"Contactless Electrowetting"

Thesis submitted in partial fulfillment of the requirement for the PhD Degree issued by the Universitat Politècnica de Catalunya, in its Electronic Engineering Program

Vito Di Virgilio

Director: *Luís Castañer*

October 2015

Contents

Table of Figures

Abbreviations

EW	Electrowetting
EWOD	Electrowetting on dielectric
REWOD	Reverse electrowetting
µTAS	Micro total analysis systems
MEMS	Microelectromechanical systems
TPL	Triple contact line
MST	Maxwell Stress Tensor
RGB	Red Green Blue colors of a display
LCD	Liquid crystal display
FPS	Frames per second
LED	Light emitting diode
CAD	Computer aided design
FEA	Finite element analysis
ES	Electrostatics module
CIR	Circuits module module
TPF	Two phase fluid module
CFD	Computed fluid dynamics
PDMS	Polydimethylsiloxane
XPS	X-ray photoelectron spectroscopy
RH	Relative humidity
C_A	Capacity per unit area
C_p	Parasitic capacity
R_p	Parasitic resistance
ρ	Density
μ	Dynamic viscosity
ϑ	Contact angle
γ	Surface tension
ε	Dielectric permittivity
ζ	Friction coefficient
r	Droplet radius
$\Omega(\vartheta)$	Spherical cap

…to Laura

Acknoledgements

My most warm thank you goes to prof. Luís Castañer, who supported me in any moment and with infinite patience during these years. I owe him my professional career; all that he taught me is priceless. Thank you so much.

Following, my thoughts go to my wife Laura, who suffered my very painful thesis writing process, for having waited for me so many “thesis nights” and for having sacrificed an uncountable number of holidays/week end. You are the best of my life and you make me better person every day.

Thanks to my parents, grandparents and to my sister, for having believed in me every day of my life. From now it is my turn to support you, Lucia, you are much smarter than me and you will be a great physicist!

Thank you for all the people I met at UPC; thank you Miguel, for fabricating all kinds of stuff for my lab; thank you Gema for having been so patient to teach me how to manage all strange (and very dangerous) stuff in clean room. Thank you David, Dennis, Moises, Jordi, Lukasz, Arnau, Enrique, for all the time spent together in fantastic discussions, over technology and not, no matter it was you have taught me so much and I always enjoy to spend time with you.

Thank you Sandra for having helped me to solve numerous Comsol problems and for that fantastic time at Comsol conference. Now it is my turn to give you back the favor.

Thank you Angel, for always being there trying to solve my existential problems as a student giving me your smart advices over how to do and above all do not things.

Thank you to all the people of MNT group. It is an honor to have worked with you.

Summary

Electrowetting technology, known since more than 100 years, just recently was successfully applied for the fabrication of devices such as pixels, liquid lenses and µTas (micro total analysis systems). Some of those devices are already a market product and some others are expected to reach the maturity to be marketed in the short period, although some fundamental aspects of the electrowetting phenomenon are not yet clear, like the origin of the saturation and the driving forces that lead to a contact angle variation.

In this dissertation are presented several contributions to the electrowetting technology.

First, have been reported the preliminary evidences about the contactless variation of the contact angle. Furthermore, these phenomena have been studied deeply and rigorous experimental work has been performed.

Experimental data have been cross checked with simulations results and theoretical calculations.

Finally, the results of the contactless electrowetting experiments lead us to be able to state that the driving element of the contact angle variation is the charge. Contactless electrowetting method has also unlocked the possibility to experimentally measure the impact of surrounding humidity in electrowetting dynamics and the limitations that introduce in the saturation of contact angle. The relationship between relative humidity and saturation contact angle resulted to be directly proportional and in line with the Peek's law prediction, here applied to a system in the micro scale.

Therefore the last part of the dissertation was dedicated to the study of the charge driving of an electrowetting device in order to be able to control and predict the contact angle dynamics. As additional results it has been found that charge injection rate affects the speed of the contact angle variation, with negligible effects on the contact angle saturation. Cross checking the experimental results with theoretical predictions it has been found that the approximation of a droplet to a spherical cap gives a very good result while no clear contributions could be given to the saturation problem, leaving it open and without any clear solution, so far.

Additionally, in this work contains a comprehensive review of state of the art of electrowetting technology and a detailed description of the multiphysic simulation method used.

Chapter 1: Fundamentals of Electrowetting

Electrowetting is the modification of the contact angle of a liquid drop by applying an electric field.

1.1 Introduction

Electrowetting is a technique that allows modifying the contact angle of a drop of liquid on a solid surface by the application of an electric field.

The first observations of contact angle variation by electrical means were reported by Gabriel Lippmann at the end of XIX century [1]. In his work, Lippmann reports on how to control the variation of the contact angle of a mercury drop in contact with an electrolyte by applying an electric field across such system, as shown in Figure 1-1a. Lippmann observed what he called *electrocapillarity* effect, which is the basis of the modern electrowetting concept.

In his work, Lippmann formulated the basic theory of electrocapillarity and also developed some interesting applications, like an electrocapillarity based motor and a very sensitive electrometer.

Unfortunately, the works developed around electrocapillarity during the large part of XX century, where about aqueous electrolytes in direct contact with mercury drops, or mercury drops in contact with insulators, configurations that bring to unwanted electrolytic effects, even applying very low voltage such as few milliVolts.

Just in 1981 Beni and co-workers[2], reporting on a novel pixel structure, Figure 1-1b,[2], described and named for the first time the electrowetting effect. The novelty of the study was also that they focused the attention on the triple contact line (TPL) behavior when a voltage is applied between the substrate and the liquid.

Electrowetting on dielectric (EWOD) concept was introduced only few years later, in the ’90, by Berge[3]. His idea was to avoid the contact between the liquid and the conductive surface by introducing a thin insulator layer in between. This feature introduces great reliability as the electrolysis problems are solved; furthermore, it unlocks the use of this technology in a wide range of applications, such as micro-lenses, electrowetting pixels and microfluidics advanced applications.

The general schematic of an *electrowetting on dielectric* system is presented in Figure 1-1c. The basic electrowetting on dielectric configuration is a drop of conductive liquid sit on a dielectric surface.

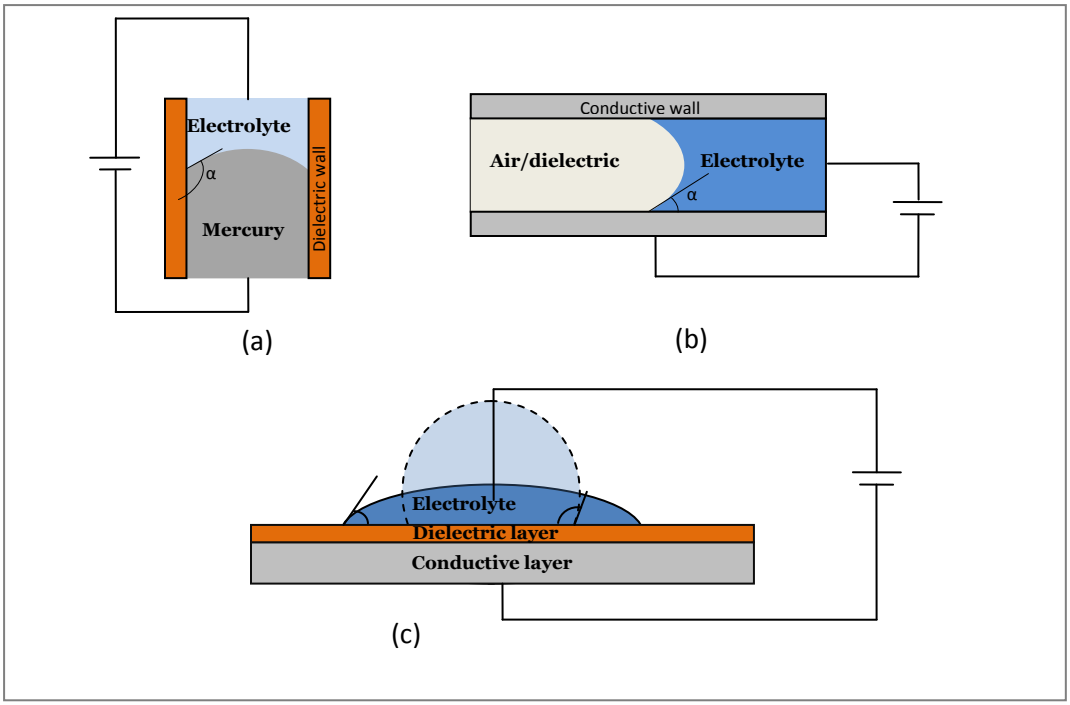

***Figure 1-1**: Schematic representation of a) an electrocapillarity device, b) an electrowetting device and c) and electrowetting on dielectric device.*

The dielectric surface covers a conductive layer, which connected to ground. The liquid drop is polarized with a certain voltage. The contact angle suddenly decreases, as the wetting properties of the surface are enhanced. The process is completely reversible and controllable; when the voltage biasing the liquid decreases, the contact angle increases; when the voltage is removed, the system goes back to its original state.

1.2 Theoretical concepts

As explained in the previous Section, typical EWOD setup is a polar liquid drop sit on a thin hydrophobic insulator layer that covers the bottom electrode; the conducting drop is surrounded by a dielectric; according to the application, it could be air or an immiscible fluid, like silicone oil. This last solution reduces the hysteresis effects.

The estimation of the body force effect over the surface tension is done by analyzing the Bond number. The bond number, reported in eq.(1-1), where $\Delta\rho$ is the difference in density between the liquid drop and the surrounding fluid, g is the gravitational force, R is the characteristic length of the

drop and γ_{ci} is the surface tension between the conducting and insulating phase, represents a measure of the importance of surface tension over the body forces.

The typical drop size can range from few millimeters down micrometer size therefore the Bond number β is smaller than the unity[4]; therefore the gravitational effect over the drop is negligible. The Bond number is given by:

$$\beta = \frac{\Delta\rho g R^2}{\gamma_{LV}} \qquad (1\text{-}1)$$

Where $\Delta\rho$ is the difference in density of the two phases involved (kg/m^3), g is the gravitational acceleration (m/s^2), R is the radius of the droplet (m) and γ_{LV} is the liquid-vapor surface tension (N/m). If no voltage is applied the drop takes a spherical cap shape due to Laplace equation, eq.(1-2), where r_1 and r_2 are the two principal radii of curvature of the surface; at the triple contact line the surface tensions between liquid (*L*), vapor (*V*) and solid (*S*) are in equilibrium and, at a mesoscopic scale[5], the drop shows the Young contact angle defined by eq.(1-3).

$$\Delta p = \gamma_{LV}\left(\frac{1}{r_1}+\frac{1}{r_2}\right) = \gamma_{LV}\cdot k \qquad (1\text{-}2)$$

$$\cos\vartheta_Y = \frac{\gamma_{SV}-\gamma_{SL}}{\gamma_{LV}} \qquad (1\text{-}3)$$

When an electric field is applied the equilibrium is broken; the contact angle ϑ_Y decreases towards a final contact angle ϑ_V that is smaller.

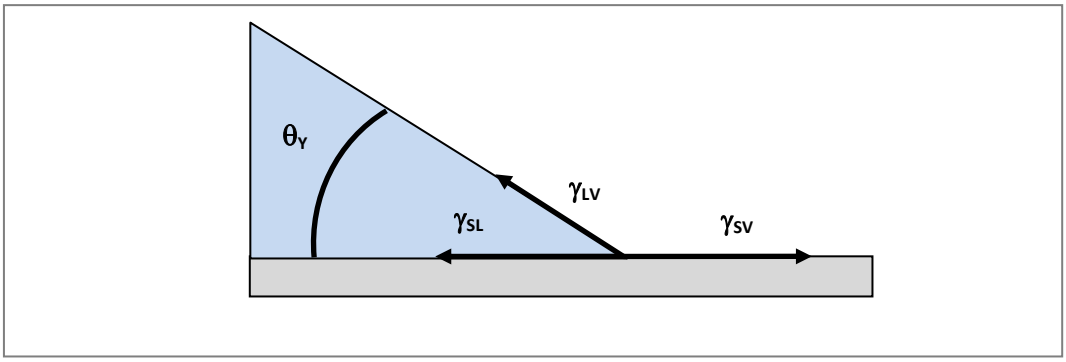

Figure 1-2: *Force balance at the contact line.*

The most generic equation that predicts the final contact angle is the Young-Lippmann equation:

$$cos\vartheta_V = cos\vartheta_Y + \frac{\varepsilon_0\varepsilon_r}{2t\gamma_{LV}}V^2 \qquad (1\text{-}4)$$

where ε_0 and ε_r are the relative permittivity of the vacuum and the dielectric layer, t is the dielectric thickness, γ_{LV} [N/m] is the liquid-vapor surface tension and t is the dielectric thickness [m]. This equation was already formulated by Lippmann in his work[1], but in that case, the ε_r was the permittivity of the fluid and the thickness of the dielectric was not taken into account. As we can see, the higher the dielectric constant and the thinner is the dielectric layer, the smaller the final angle will be.

Thinner insulator layers will induce easier dielectric breakdown, therefore a tradeoff must be found in order to tune the contact angle variation within a safety operational range.

For a general design of electrowetting devices, the Lippmann-Young equation, eq.(1-4), predicts quite well the contact angle variation. On the other hand, one should reach complete wetting when $\cos\vartheta_V = 1$. This situation has never been observed so far, even using dielectric layers capable to withstand very large voltages before the breakdown. The contact angle follows a parabolic variation until a saturation state (to a voltage increase does not follow a contact angle decrease) is observed. The Lippmann-Young equation is no more valid; instead the contact angle becomes independent to the voltage applied.

The physics behind the contact angle saturation is still matter of interest and research. Several works report on the contact angle saturation: Verheijen and Prins [6] relate it to the charge trapping effect in the dielectric layer, also supported by the work of Janocha et al.[7]; Vallet et al. [8] attribute it to the air ionization around the TPL, also sustained by Di Virgilio et al. [9] furthermore relating it with air humidity; Quinn et al.[10, 11] attribute the contact angle saturation to the fact that the surface tension between liquid and solid cannot be smaller than zero, being air ionization a concurring effect rather than a limiting one; Papathanasiou et al.[12, 13, 14] propose a local dielectric breakdown due to the diverging electric field in the vicinity of the TPL.

Up to date, any of the proposed theories has fully answered the contact angle saturation problem that remains an open research topic in the electrowetting technology.

1.3 Electromechanical approach: electrostatic fields change the contact angle in electrowetting

Electrowetting on dielectric is a phenomenon that intrigued many researchers from different fields such as chemists, physicists, electrical and mechanical engineers; therefore many approaches have been proposed and all of them predict the same final angle reduction. On the other hand, a broadly accepted theory explaining the saturation has not yet been found.

Among all the different theories proposed, in this work will be used the one formulated by the electromechanical approach, that provides not only information about how the contact angle evolves, but also about the forces exerting on the liquid body by the electric field. This information will be extremely useful at the moment of designing a set of equation for a reliable Finite Element Analysis. The results will be given not only at the triple line boundary but for the overall body dynamics.

When an electric field is applied to an electrowetting setup, mechanical forces are exerted on the liquid by the electric field. In this Section the response will be discussed in terms of contact angle variation due those forces.

This approach was firstly introduced by T.B. Jones and reported in [15, 16, 17].

The electrical body force exerted on isotropic liquids can be formulated in the Korteweg-Helmholtz body force density[18]:

$$\vec{f}_k = \rho_f \vec{E} - \frac{\varepsilon_0}{2} E^2 \nabla\varepsilon + \nabla\left[\frac{\varepsilon_0}{2} E^2 \frac{\partial\varepsilon}{\partial\rho}\rho\right] \qquad (1\text{-}5)$$

where ρ_f is the net free space charge density in the liquid, ρ is the mass density and ε the dielectric constant of the liquid and *E* the electric field. In EWOD context the liquid can be considered homogeneous and incompressible, therefore the third term of equation (1-5), which describes the electrostriction can be neglected[19].

By applying voltage between the drop and the counter electrode, the charge in the liquid are drawn to the liquid/dielectric interface, the liquid is considered a perfect conductor so the free charge density in the bulk is zero; only the forces acting on the free liquid interfaces are contributing to a translational motion of the liquid. The calculation of the total net force acting on the liquid can

hence be computed by integrating equation (1-5) along the liquid surface, over the momentum flux density of the electric field. The Maxwell Stress Tensor (MST) is particularly appropriate for this computation [20]. Equation (1-6) is the MST consistent with equation (1-5).

$$T_{ik} = \varepsilon_0 \varepsilon \left(E_i E_k - \frac{1}{2} \delta_{ik} E^2 \right) \qquad (1\text{-}6)$$

δ_{ik} is the Kroneker delta function and *i, k =x,y,z*.

At the liquid/dielectric interface, the tangential component of the electric field vanishes at the surface while the normal component is related to the surface charge density by $\rho_s = \varepsilon_o \vec{E} \cdot \vec{n}$ where $\vec{n}$ is the outward unit normal vector; $\vec{E}$ vanishes in the bulk of the liquid.

The net force acting on the liquid surface can be calculated by:

$$F_i = \oint_{\Sigma} T_{ik} n_k dA \qquad (1\text{-}7)$$

The result obtained is that the only non-vanishing contribution is a force per unit surface area directed outward the liquid surface and directed along $\vec{n}$.

$$\frac{\vec{F}}{dA} = P_{el} \vec{n} = \frac{\varepsilon_0}{2} E^2 \vec{n} = \frac{\rho_s}{2} \vec{E} \qquad (1\text{-}8)$$

The electrostatic pressure term, P_{el}, is here introduced and represents a negative component to the total liquid pressure. In order to understand how it contributes to the liquid motion, it is necessary to understand the electrostatic field and charge density distribution along the surface.

In general, close to the surface and far away from the TPL the electrostatic pressure only acts in the normal direction and any possible effect on the surface is counterbalanced by elasticity. In the vicinity of the TPL the electrostatic pressure has also a tangential component due to the sharp increase that the solid/liquid charge density also increases sharply, $\rho_{SL} = \varepsilon_o \varepsilon_d U/d$. The result is that the electrostatic force pulls the drop from TPL resulting in a different contact angle.

The interpretation proposed by Digilov [20], based on thermodynamic analysis, suggested that at the TPL the electrostatic force was originated by an excess of electrical charge. Vallet et al.[8] give evidences about excess of charge at TPL by imaging the photon emission due to air or gas ionization; many dielectric atmospheres (such as SF_6 an C_2F_6) were used, resulting in different ionization

emissions but similar saturation levels, pointing out the saturation is not related to the dielectric surrounding medium. Besides the charge accumulation at TPL, Vallet et al. proposes in [8] a convenient methodology in order to analyze the electrostatic field near to the edge region, the TPL. Vallet et al. consider the drop an infinite planar wedge; by applying the Schwarz-Christoffel transformation it is then possible to calculate analytically the electrostatic field. These calculations are shown in Section 3.5, where is also explained in detail the whole procedure to get to that particular equation.

Using the Schwarz-Christoffel transformation proposed by Vallet et. al, Kang [21] calculates analytically the horizontal net force acting on the drop, supposing that the drop shape remains wedge, by integrating equation (1-8) horizontal component along the liquid/vapor interface. The results show that both electric field and charge distribution diverge while approaching the TPL. Hence the MST reaches a maximum value at the TPL and it fades down to a negligible value already at small distance from TPL.

Due to its rapid decay, this force can be assumed to be localized.

The resulting force obtained by Kang[21] is:

$$F_e = \frac{\varepsilon_0 \varepsilon_d}{2d} V^2 \, cosec\, \vartheta \qquad (1\text{-}9)$$

This force can be decomposed into horizontal F_{ex} and vertical F_{ey} components:

$$F_{ex} = \frac{\varepsilon_0 \varepsilon_d}{2d} V^2 , F_{ey} = \frac{\varepsilon_0 \varepsilon_d}{2d} V^2 \, cot\, \vartheta \qquad (1\text{-}10)$$

Interestingly, the horizontal force component is not depending on the contact angle: the F_{ex} component pulls the TPL until it is balanced by the dragging force due to the surface tension. On the other hand, the horizontal force component is confined to a very small area close to the drop edge, comparable to the dielectric thickness. The dielectric thickness is comprised in the range between the micron and hundreds of microns. In the macroscopic point of view, the stress can be still represented as force acting in a point.

1.4 Electrowetting on dielectric applications

The applications of electrowetting on dielectric technology are concentrated in optics and microfluidics domain and it can be mainly divided in three areas: electrowetting lenses, electrowetting pixels and electrowetting based microfluidics. Some more exotic application includes energy harvesting devices, micro prism systems, bi-stable pixels.

1.4.1 Electrowetting lenses

Electrowetting lens concept was introduced by Bruno Berge[22], few years after he introduced the concept of electrowetting on dielectric by coating the bottom electrode.

The concept he proposed is shown in Figure 1-3. A glass enclosure contains two transparent immiscible liquids, one conductive and the other dielectric.

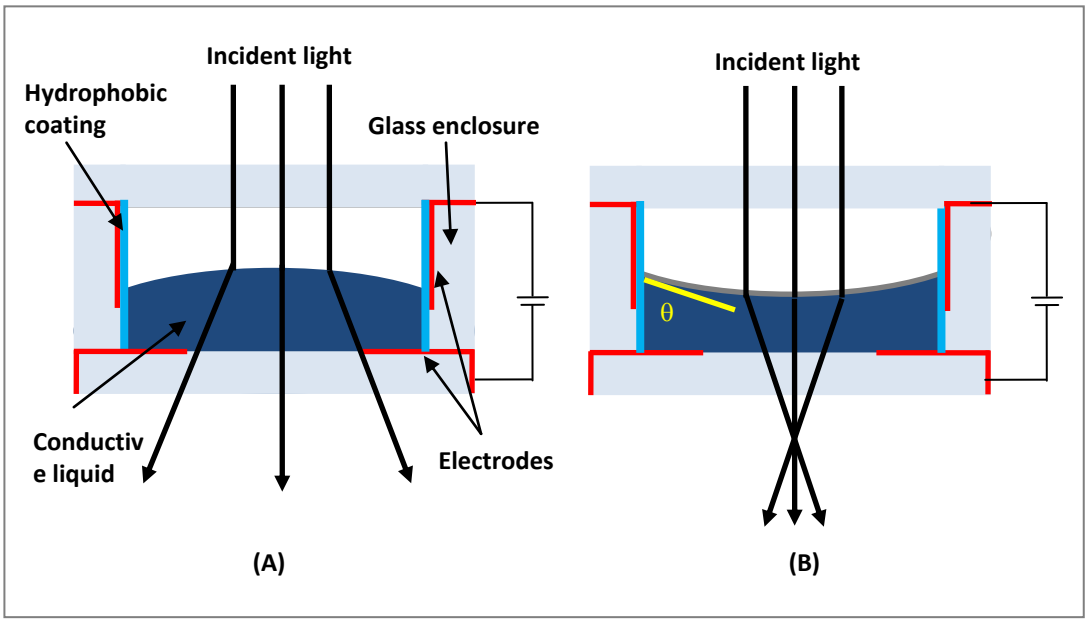

***Figure 1-3**: General schematic of an electrowetting liquid lens: a) shows the arrangement of the two liquids contained in the glass enclosure when no voltage is applied. B) Represents the system at ON state, when a voltage is applied to the electrodes. The contact angle between the two liquids is modified and then the incident light path is modified, too.*

The index of refraction of the two liquids differs; typical values are n≅1.6 for the conductive liquid and n≅1.3 for the dielectric liquid. The glass enclosure has electrodes at the bottom and dielectric coated electrodes on the side walls.

Being hydrophobic, the dielectric layer forms a high contact angle with the side walls, resulting in a convex meniscus; incident light diverges, (Figure 1-3a). When the lens is turned on, the polarization of the side walls results in a variation of contact angle between the two liquids and the side wall; the meniscus becomes convex, therefore the light path is modified converging in a given point, (Figure 1-3b). The electrowetting lenses have been very interesting and promising because no movable parts are involved, therefore the miniaturization is easily achievable. The variable focus lenses based on electrowetting are very promising to be integrated in portable electronic devices such as mobile phones, tablets and sport cameras. The French company Varioptic has been producing variable focus lenses based on electrowetting since 2007, while in late 2011 it was acquired by Parrot Company[23]

1.4.2 Electrowetting displays

Electrowetting pixel concept reported by Beni and co-workers in 1981[2] was lately developed by Feenstra and Hayes[24], who reported in 2003 the development of an electrowetting display based on voltage controlled motion of a colored oil covering the pixels. The basic schematic of the electrowetting pixel is shown in Figure 1-4. The pixel substrate is made in glass covered by a transparent electrode covered by a transparent dielectric hydrophobic layer (i.e. Teflon, Cytop).

The oil preferentially wets the hydrophobic dielectric layer when no voltage is applied; at OFF state, the oil blocks light coming from the back of the pixel, or in case of reflective display, the light coming from external source. The oil is surrounded by an electrolyte, i.e. water or other polar solutions. When a voltage is applied between the back electrode and the electrolyte, the hydrophobic layer changes its wettability properties. The electrolyte displaces the oil and wets the pixel surface. The oil is confined in a corner allowing the light to shine through the pixel.

The electrowetting technology enables the fabrication of novel displays that show better performances for outdoor use as a back-reflector can be integrated and light coming from external sources enhances the luminosity. Transparent and trans-reflective displays can also be easily fabricated, using the same fabrication process of standard LCD displays. At the moment few

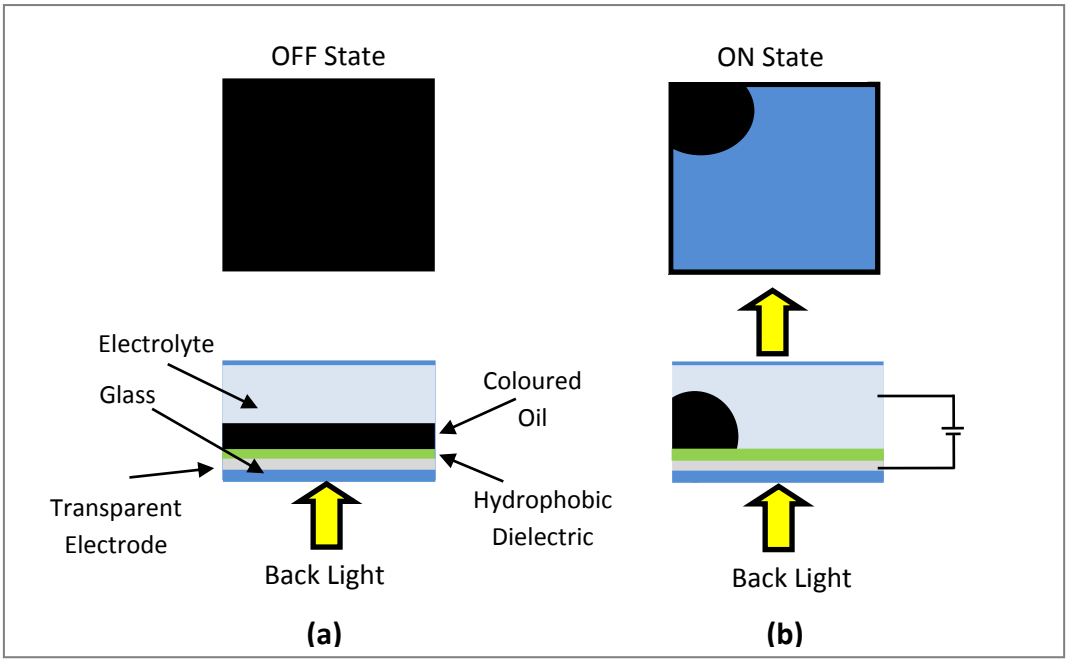

***Figure 1-4**: Schematic of an electrowetting pixel. a) shows the electrowetting pixel in OFF state. The backlight is blocked by the colored oil wetting completely the pixel surface, which is a hydrophobic insulator. b) shows the ON state of the pixel: the electrode is polarized therefore the wettability increase. The electrolyte wets the pixel surface displacing the oil. The oil acts as a curtain that opens and allows the backlight to go across the pixel. On the top of the pixel can be placed a color filter for the RGB color arrangement. The backlight can be replaced by a back-reflector that allows the incident sunlight to be reflected and then increase the usability of such displays in sunshine. Electrowetting pixels are also suitable for transparent display fabrication.*

companies are fabricating electrowetting based displays, among them Liquavista BV[25], a spin out of Philips Laboratories, is holding the leadership, being acquired in 2010 by Samsung and lately acquired by Amazon.

A slightly different electrowetting display concept, “electrofluidic displays” has been introduced by Heikenfeld and co-workers [26] and resulted in a spin-off company, Gamma Dynamics[27]. In this case, a liquid is dragged in and out of a reservoir close to the display surface, acting as an optical curtain. Another electrowetting display company is ADT[28], based in Dusseldorf, Germany; ADT commercialize big size displays based on a bi-stable pixel technology, based on electrowetting and microfluidics.

1.4.3 Electrowetting for microfluidics applications

Electrowetting real potential is the ability to manipulate precisely small quantity of fluid; this feature is very interesting for μTAS (micro total analysis systems) and for microfludics in general [29, 30, 31]. A general schematic of a lab-on-a-chip based on electrowetting is shown in Figure 1-5. The concept

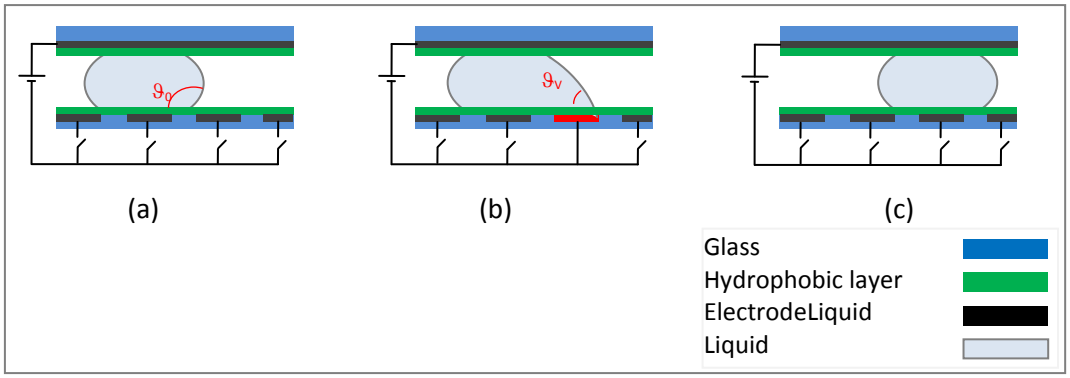

***Figure 1-5**: a) The drop sits in rest between the two plates, squeezed, no voltage is applied. The contact angle showed is the static one, hydrophobic. b) shows the moment in which one of the electrode is biased. The voltage varies and so the contact angle decreases due to the wettability increase. A net force arises and pulls the drop to sit over the activated electrode. c) When voltage is withdrawn, the contact angle increases. The drop sits in rest in a new position.*

is based on addressable electrodes that can individually controlled in order to arrange paths along which the drop moves. The programming of the activation sequence controls the movement of the drop over the surface. The electrodes are buried beneath a dielectric hydrophobic layer. In Figure 1-5 is shown a typical EWOD setup. In general, the liquid drop is confined between tho parallel plates where the top one is conductor and it is connected to ground; the lower one has patterned electrodes covered by an hydrophobic dielectric layer. When a drop sits across two electrodes and one of them is polarized, the drop changes its contact angle asymmetrically. The wettability increase of the polarized electrode gives rise to a net force in the bulk of the drop, that results in a net force and hence in a movement. Electrowetting systems have been used successfully for the manipulation of tiny amount of body liquids such as blood, urine, saliva, etc.[30]; in particular Cho et al. [29] report the successful implementation of actions such as creation, merge, cutting and mixing of drop that definitely enable the cost-effective implementation of automated solution for bioassay at micro scale. The leader in electrowetting based devices for bioassay and genome sequencing is Advanced Liquid Logic [32], a spin-out of the Duke University. In July 2013 Advanced Liquid Logic was acquired by Illumina Inc[33], the leader manufacturer of life science tools and integrated analysis system for genetic variation and function.

1.4.4 Other applications of electrowetting on dielectric

Electrowetting on dielectric showed such versatility that very interesting and exotic applications have appeared.

One of the most unique applications electrowetting is involved with is proposed by the company mPhase[34], which introduced the electrowetting concept in battery field. Figure 1-6 shows the mPhase battery manufacture schematic. Using electrowetting, the contact between anode and cathode of a battery is created by electrolyte flowing from a different reservoir. This solution is suitable for achieving a potentially infinite shelf-life, lower manufacture cost and power management.

Recently, in 2011, two mechanical engineers from the University of Wisconsin, Tom Krupenkin and Taylor Ashley[35] came up with a novel energy harvesting method based on microfluidics and electrowetting; they named it reverse electrowetting or REWEOD. The REWOD is based on the fabrication of channels or plates filled by discrete drops of conductive liquid surrounded by dielectric liquid. In the case reported by Krupenkin and Ashley, the conductive liquid was mercury and galinstan.

The idea behind the REWOD concept is that a mechanical stress can be converted in electrical charges due to the interaction of a number of discrete drops with electrodes. Figure 1-7 shows the three main drop actuation for energy harvesting through REWOD. An external electrical circuit gives continuous bias between the drops and the electrodes; due to external actuation (i.e. pressure generated by human step), when the drops move into the microfluidics circuit, the total charge that can be maintained at the solid-liquid interface decreases; the excess of charges generated flows back to the electrical circuit generating electrical current.

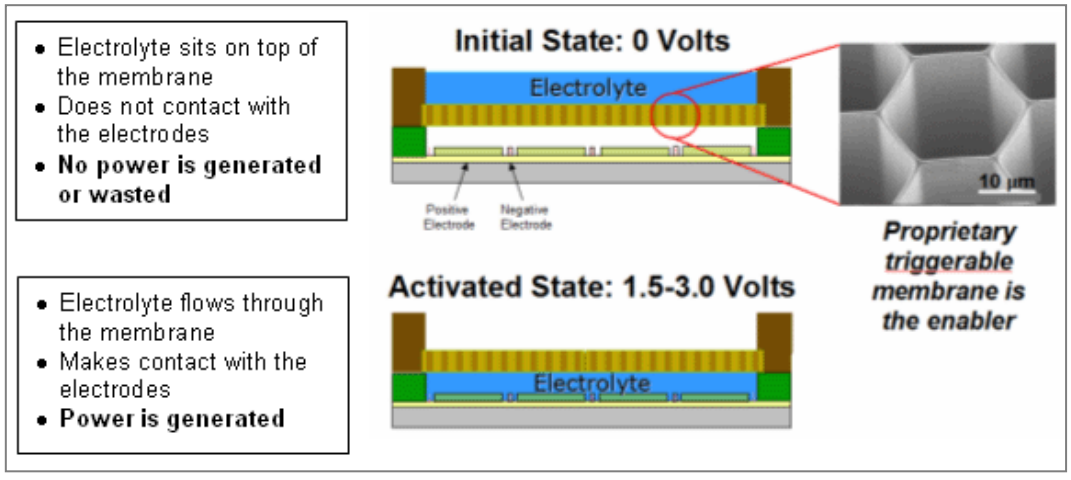

***Figure 1-6**: Schematic representation of the mPhase system for smart battery systems and shelf-life extension. Image reprinted with permission from the website of mPhase Technologies [34].*

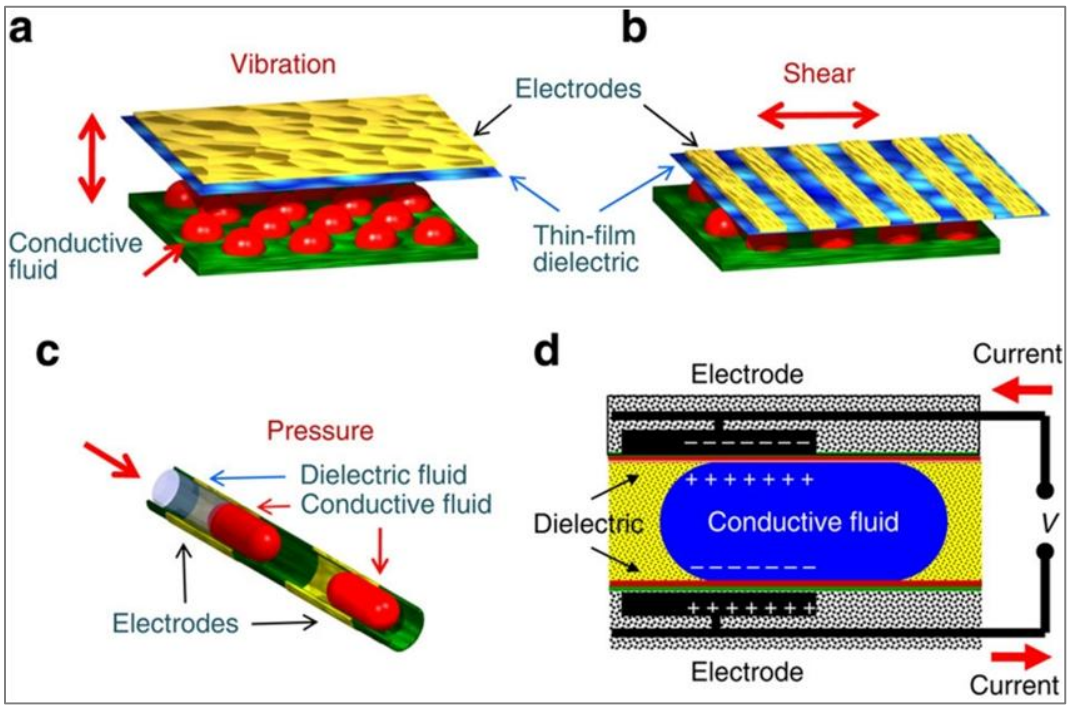

***Figure 1-7**: Schematic of three major drop actuations. Reprinted by permission from Macmillan Publishers Ltd: Nature Communications [35], copyright (2011).*

This phenomenon still lacks of deep and detailed physic explanation, as only experimental data were reported. In addition to that, several drawbacks are reported, such as line pinning of the drop causing fluid actuation interruption, excess of charge trapping in the dielectric and breakdown of the dielectric coating.

Despite of that, the main results are promising as in a relatively small packaging; 1W of excess power can be easily created. Thus material optimization is needed to achieve the optimal power production. Figure 1-8 shows how can be practically used REWOD energy harvester: Figure 1-8a shows a REWOD device embedded in footwear, Figure 1-8b shows a vibration harvester that can be integrated in tiles or roads; these ideas are not novel as some previous works propose integration of piezoelectric in footwear [36] and there are commercially available energy harvester tiles by Pavegen Systems[37], nevertheless the output power range it is only about 10^{-6} to 10^{-2} W[36, 38, 39].

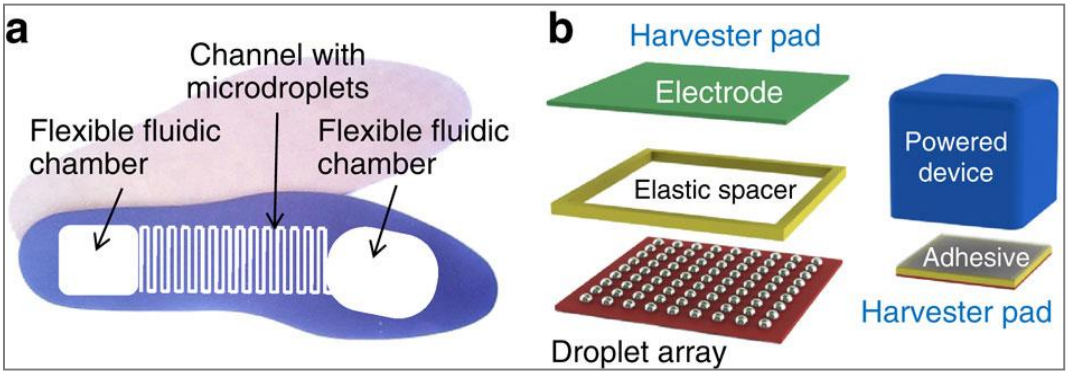

***Figure 1-8**: (**a**) Footwear-embedded microfluidic energy harvester and (**b**) a REWOD-based vibration harvester. Reprinted by permission from Macmillan Publishers Ltd: Nature Communications [35], copyright (2011).*

1.5 Conclusions, motivation and dissertation outline

Electrowetting displays and lenses are already a commercialized product that works on the electrowetting on dielectric principle; machines for genotyping based on this technology are ready to be marketed; REWOD energy harvesting is very promising if compared to actual piezoelectric technology. In spite of that, many of the fundamental aspects of the electrowetting on dielectric physics have to be better understood, in order to reach a complete process optimization and in order to improve the overall performances of the product.

The main challenges researchers in this field face are:

- Contact angle saturation
- Dynamics of the contact angle variation
- Fine control of the contact angle variation rate
- Decrease below 15V of the voltage control

Contact angle decrease close to zero degrees is theoretically possible, nevertheless it have never been achieved. Obtaining a smaller contact angle assumes a capital importance in applications such pixels and lenses. Up to date many debates are opened and no clear solution is found yet.

The contact angle variation is quite well described by Young-Lippmann equation eq.(1-4), until saturation is reached. Eq.(1-4) does not take into account many dynamic effects that in the wetting process really occur. A dynamic set of equations explaining the wetting is still missing.

Usually, the contact angle variation is very suddenly, overshoots are very much limiting the performances in pixel dynamics and lens precision. A smoother actuation could help to tune finely the contact angle variation rate in order to avoid overshoots and smoothly reach the set point.

At the moment, many efforts have been done in order to lower the voltage below 15V. This voltage target is a constraint given by the integration with portable electronics. Up to date many efforts have been made in fabrication process optimization and material [40, 41]. In general, the dielectric layer is the major responsible of actuation voltage increase, therefore the thinner it goes, the easier breakdown occurs; the reliability is indeed a concern. A new actuation strategy might be a convenient solution in order to overcome unwanted dielectric breakdown together with low contact angle values.

This dissertation is aimed to shine light on electrowetting on dielectric technology, trying to offer a further improvement for the actual electrowetting based applications and trying to open path to novel electrowetting based applications.

1.6 Outline

Chapter 2 gives a broad overview on complete FEA analysis strategy for the evaluation of the different electrowetting arrangements, according to the application it is referred to.

Chapter 3 is dedicated to the description of the Contactless Electrowetting on Dielectric phenomenon. This phenomenon is related to the charge spreading from a source to a drop sit on a dielectric hydrophobic layer. The contact angle variation is evaluated by comparison to previous works and by FEA simulations.

Chapter 4 reports experimental data about contact angle increase due to “corona” effect that unlocks future developments of contactless electrowetting on dielectric platforms for liquid manipulation. Moreover saturation angle has been observed to be closely related to the humidity.

Chapter 5 reports about the dynamics of contact angle variation by controlling charges delivered to the system. This method is suitable for finely tune the contact angle variation in systems that are very sensitive to overshoots and therefore more precision is needed. Moreover, the energy efficiency of electrowetting on dielectric devices can be enhanced.

Chapter 6 closes the dissertation by drawing conclusions and describing further works.

Chapter 2: Electrowetting on dielectric Finite Element Analysis

In this chapter are presented the results of Finite Element Analysis multiphysic simulations performed using Comsol.

The systems taken into account for the modeling are the three different configurations of electrowetting devices: sessile drop under electric field, electrowetting lens, electrowetting pixel.

2.1 Introduction

The aim of the chapter is to show how a performance FEA analysis of an electrowetting device can be run by using the Comsol Simulation software. Up to date, some contributions on the simulation of electrowetting on dielectric have remained confined only to the CFD area, in particular, Cahill et al. [42] reports over a pure CFD drop-based electrowetting simulation and later, in 2010 Dannenberg et al. [43] introduce a basic coupling with electrostatics. In this Chapter, as Comsol are coupled Computed Fluid Dynamics (CFD), circuit definition (CIR) and ElectroStatic (ES) modules in order to get a multiphysic simulation coupling also the effects of the power supply.

In **¡Error! No se encuentra el origen de la referencia.** it is shown the conceptual schematic of a multiphysic simulation of an electrowetting device.

CIR module provides the ES module a terminal voltage, calculated according to the electrical circuit schematic (transients, voltage limitations etc). The ES module solves the Maxwell equations starting from the voltage input from CIR. Voltage field, electric field, electrostatic force are ES outputs that feed the CFD module. The CFD module solves Navier-Stokes equations and calculates the phase field according to the fluidic boundary conditions specified and to the effect of electrostatic forces, calculated by ES module and given as an input to CFD module.

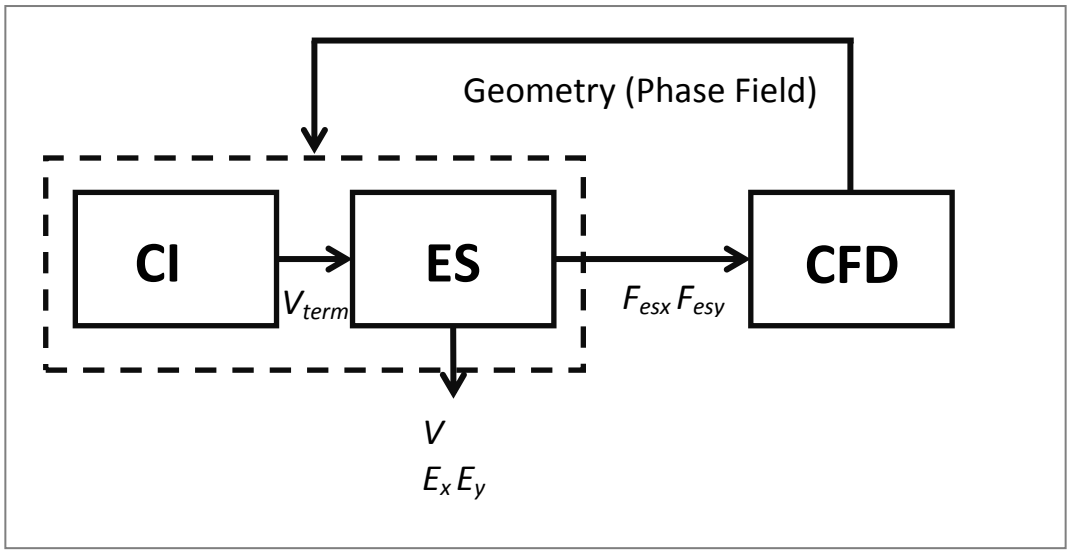

Figure 2-1: *Conceptual schematic of a simulation of an electrowetting device using Comsol software and coupling electric circuits, electrostatics and computed fluid dynamics modules.*

2.2.1 The mathematics of moving interface and electrostatics

2.2.1.1 CFD: the fluid flow modeling

CFD module solves the Navier-Stokes equations, in order to resolve the fluid motion in the device designed by the integrated CAD tool of Comsol.

The set of equations is:

$$\rho\frac{\partial u}{\partial t}+\rho(u\cdot\nabla)u=\nabla\cdot\left[-pI+\mu(\nabla u+(\nabla u)^T)\right]+F_{st}+\rho g+F$$
$$\nabla u=0 \qquad (2\text{-}1)$$

where ***u*** denotes velocity (m/s), ***ρ*** the density (kg/m^3), ***μ*** dynamic viscosity (Pas), ***p*** pressure (Pa), ***g*** gravity (m/s2). $\boldsymbol{F_{st}}$ is the surface tension force (N/m^3), and ***F*** is any additional volume force (N/m^3). External additional forces included in ***F*** allow coupling the electrostatics with CFD by the definition of electrostatic volume force as an input of the CFD model. In this way, the CFD simulation converts to an electro-hydrodynamic simulation, explained in details in the following paragraph.

The fluid motion simulations have been run taking into account that the flow is influenced by two different phases, the dielectric and the conductive one. Therefore the two phase flow extension has been used. This extension allows tracking the fluid interface by using the Phase Field method:

$$\frac{\partial\phi}{\partial t}+u\cdot\nabla\phi=\nabla\cdot\frac{3\chi\sigma\varepsilon}{2\sqrt{2}}\nabla\psi$$
$$\nabla\psi=-\nabla\cdot\varepsilon^2\nabla\phi+(\phi^2-1)\phi \qquad (2\text{-}2)$$

where σ is the surface tension coefficient (N/m), $\boldsymbol{\varepsilon}$ is an internal numerical parameter (m) that keeps control of the interface thickness between the two phases and which value goes from -1 to 1 smoothly. $\boldsymbol{\chi}$ is an internal parameter that controls the fluid interface mobility.

The phase field variable ϕ is −1 in air or oil and 1 in water. The density and viscosity, different between the conductive and dielectric phase, are automatically calculated from the phase field variable ϕ as shown following:

$$\rho = \rho_1 + (\rho_2 - \rho_1)\phi$$
$$\mu = \mu_1 + (\mu_2 - \mu_1)\phi \qquad (2\text{-}3)$$

The surface tension is also automatically calculated taken into account the fluid interface curvature and normal vector.

2.2.1.2 Electro-hydrodynamics modeling

As the fluid motion is induced by the electric potential applied. In case the voltage supply has any special feature, like specific transient time, impedance adaptation or any other feature that affects somehow the electrowetting circuit, a SPICE model can be set as input to the CIR module, available in Comsol. On the other hand, the circuit can be easily designed by using Comsol feature for the declaration of each component. Finally, the circuit defined in CIR module can be easily coupled to the ES module by defining a special node value as terminal voltage. The terminal voltage is hence used as input by the ES module.

The ES module is capable to calculate the electric field in the droplet by solving the Poisson equation:

$$\nabla(\varepsilon_0 \varepsilon_r \nabla V) = \rho_f \qquad (2\text{-}4)$$

Where V is the terminal voltage, ε_0 and ε_r are the permittivity of the vacuum and relative to the material, and ρ_f is the free charge density.

The equations shown above are automatically solved by the Comsol solver; however the simulated system has two different fluid phases and they move according to the Navier-Stokes equations, therefore, in order to couple electrostatics and fluid motion correctly it is needed to track the electric permittivity with the fluid motion, the following equation couples CFD and ES and it is set up as:

$$\varepsilon_r = \varepsilon_{r1} + (\varepsilon_{r2} - \varepsilon_{r1})\phi \qquad (2\text{-}5)$$

As mentioned in the previous paragraph, the coupling between the Fluid Flow and Electrostatic physic is done by applying the electrostatic volume force as external force in eq.2-1. The electrostatic force, hence, induces a variation in the fluid motion.

The electrostatic volume force (N/m^3) is calculated starting from the Maxwell Stress Tensor (MST), by calculating its divergence:

$$F = \nabla T_{ik} \tag{2-6}$$

The MST is given by:

$$T = ED^T - \frac{1}{2}(D \cdot EI) \tag{2-7}$$

where ***I*** is the identity matrix, ***E*** is the electric field and ***D*** is the electric displacement field:

$$E = -\nabla V \tag{2-8}$$

$$D = \varepsilon_0 \varepsilon_r E \tag{2-9}$$

For a 2D model, the MST tensor is represented by:

$$T = \begin{bmatrix} T_{xx} & T_{xy} \\ T_{yx} & T_{yy} \end{bmatrix} \tag{2-10}$$

That is equal to:

$$T = \begin{bmatrix} \varepsilon_0 \varepsilon_r E_x^2 - \frac{1}{2}\varepsilon_0 \varepsilon_r (E_x^2 + E_y^2) & \varepsilon_0 \varepsilon_r E_x E_y \\ \varepsilon_0 \varepsilon_r E_x E_y & \varepsilon_0 \varepsilon_r E_y^2 - \frac{1}{2}\varepsilon_0 \varepsilon_r (E_x^2 + E_y^2) \end{bmatrix} \tag{2-11}$$

The volume force due to electrostatics, which will only appear at the interface between fluids, is therefore calculated as following:

$$F = \begin{bmatrix} \frac{\partial(T_{xx})}{\partial x} & \frac{\partial(T_{xy})}{\partial y} \\ \frac{\partial(T_{yx})}{\partial x} & \frac{\partial(T_{yy})}{\partial y} \end{bmatrix} \qquad (2\text{-}12)$$

2.3 Electrowetting on dielectric devices step-by-step simulation.

2.3.1 Geometry definition for optimized simulations

The three main electrowetting on dielectric device types were discussed in Chapter 1. In this Section it will be discussed how to take advantage of symmetries looking towards a simplification and optimization of the geometry at the moment of proceeding to multiphysic simulations.

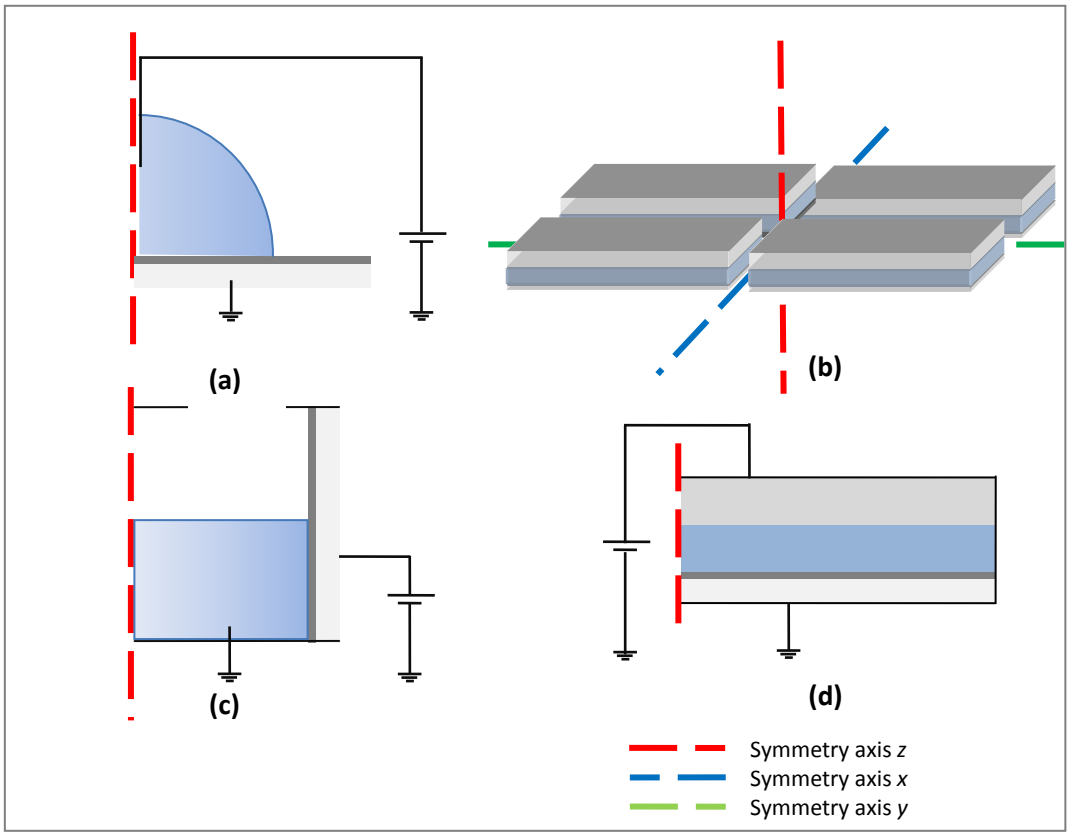

Figure 2-2: *A) Drop based electrowetting on dielectric. The geometry used for the simulation is a 2D section of the droplet. Making a revolution around the symmetry axis a 3D representation of results can be easily done. B) Liquid lenses are also simulated with a 2D axisymmetric geometry. By revolving the results around the symmetry axis a 3D result is found. C) Electrowetting pixels, for their topology, can be divided into quarter. Simulating a 3D axisymmetric quarter of pixel and mirroring the results a full 3D result can be obtained. On the other hand, as the fluid motion in these structures is very complex, this approach is only for preliminary simulations. For full 3D simulations there is no shortcut than simulating the full structure.*

2.3.2 Parameter definition

In order to properly run a multiphysic simulation, several inputs have to be provided to the model; those inputs are material physical properties, behavioral/mathematic functions and boundary conditions. Physical properties and functions involved in simulations are entered as text files respectively. Boundary conditions are set step by step in each single physical module section. Here are reported the material physical properties (table 2-1) and the functions involved in electrostatic volume force calculation in table 2-2.

In Annex II it is reported in detail the step-by-step methodology for setting up correctly an electrowetting multiphysic simulation, combining together circuit design, CFD and electrostatics. In the next Sections of tis Chapter are reported the simulations of a droplet based electrowetting device, an electrowetting pixel and an electrowetting lens.

Table 2-1: *physical properties of materials typically involved in electrowetting device fabrication and hence, simulations.*

Material	Density (kg/m^3)	Dynamic viscosity (Pa*s)	Relative permittivity
Water	1e3	1e-3	80
Air	1e-3	1e-6	1
Oil (Decane) [44]	730	0.920e-3	2
Teflon[45]	--	--	1.9

Table 2-2: *Functions involved in the simulations.*

T11	-epsilon0_const*(es.epsilon_r/2*(es.Er^2+es.Ez^2)-es.epsilonrrr*es.Er^2)
T22	-epsilon0_const*(es.epsilon_r/2*(es.Er^2+es.Ez^2)-es.epsilonrrr*es.Ez^2)
T12	epsilon0_const*es.epsilon_r*es.Er*es.Ez
T21	epsilon0_const*es.epsilon_r*es.Er*es.Ez
Fr	d(T11,r)+d(T12,z)
Fz	d(T21,r)+d(T22,z)
epsilon_r	Tpf.Vf1*perm_air+tpf.Vf2*perm_water

2.4 Droplet-based electrowetting simulation

In Chapter 1 have been described the main applications of electrowetting technology, although the basic study of materials, liquids and gasses, electronics and actuation strategies implemented in electrowetting devices is always done previously by a drop-based electrowetting experimental session.

The performance assessment of electrowetting devices can be done by running droplet-based experiments. For this reason the simulation of such structure is still very important, even if there is no practical use of it.

The structure simulated is very simple and it consists into a liquid droplet surrounded by air or by another immiscible liquid, sit onto a hydrophobic dielectric thin layer. The droplet is conductive and it is connected to one electrode while the other electrode is

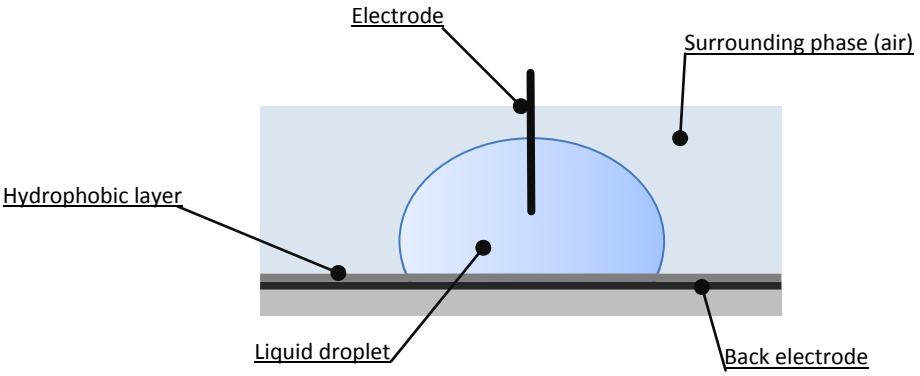

Figure 2-3: *Droplet –based electrowetting device typical structure: a conductive liquid droplet, surrounded by a dielectric phase (typically air), sits over an hydrophobic dielectric layer. The conductive liquid is biased by a contacting needle while the back electrode is buried under the hydrophobic layer.*

buried beneath the hydrophobic layer. This structure is shown in Figure 2-3.

Figure 2-4 shows the geometry simulated in Comsol. Only an axisymmetric section is simulated in order to optimize the memory use and processing power involved into the simulation. The simulations of the 2D half section represented in Figure 2-4 can be easily post-processed by revolving the 2D results around the axisymmetric axis. It this way, a pseudo-3D simulation result is obtained. On the other hand, the memory and processing power required to the system is limited, allowing results within few minutes of computation.

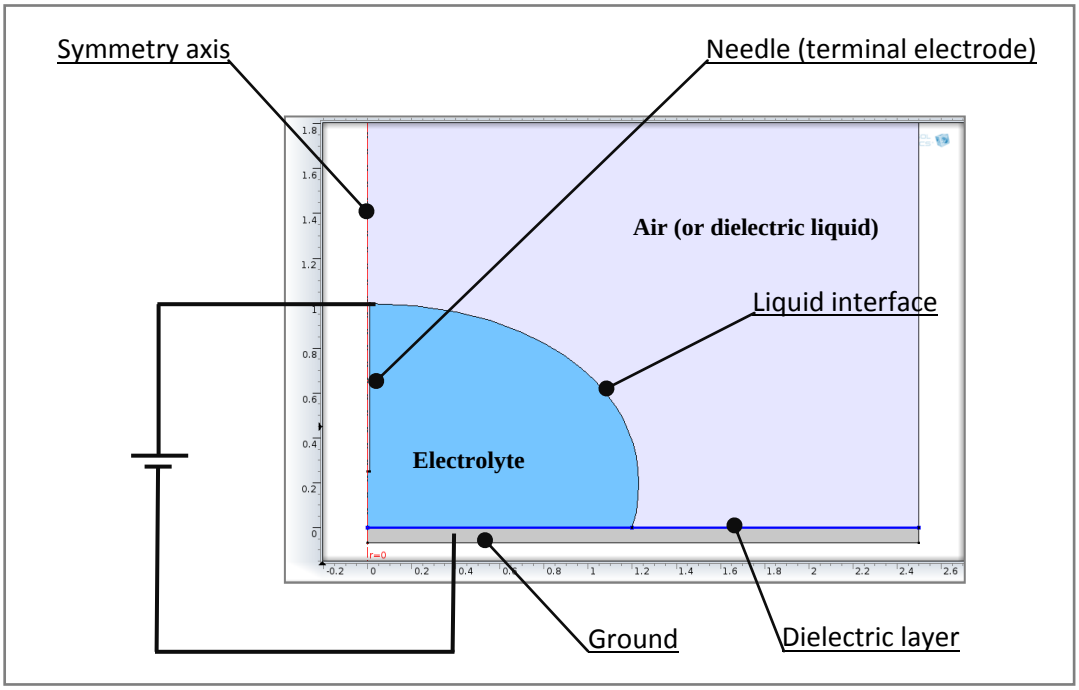

Figure 2-4: *Geometry designed to be simulated. Due to specific symmetries of the structure, only half a section has been designed. The full simulation 3D results will be plotted taking advantage of the axisymmetric axis and revolving the simulation 2D results around it.*

The boundary conditions are applied to the system following the step-by-step process described in Annex II. In particular, the electric circuit module (CIR) conditions are the same for all the electrowetting devices simulated and reported in this Chapter, while the boundary conditions for electrostatics (ES) and fluidic (TPF) modules differ depending the electrowetting device structure simulated.

For the droplet-based electrowetting device, the electrostatic (ES) and fluidic (TPF) boundary conditions specifications are reported in the next Paragraph.

2.4.1 Boundary conditions setup for the droplet-based electrowetting device simulation

Boundary conditions for the electrostatic (ES) module

The conductive droplet is connected directly to one electrode through a metal needle (placed in the center of the droplet). The ground electrode is covered by a thin dielectric layer. The coupling is done by capacity.

The electrostatic module boundary conditions applied shown in Figure 2-4 are the following:

- Ground
  - Chosen as the lower area beneath the droplet
- Terminal
  - Chosen the area delimited as “needle”, placed in the middle of the droplet and connected to the CIR module.
- Thin low permittivity gap
  - The hydrophobic Teflon layer, 1µm thickness and dielectric constant 1.9.

The conductive droplet is connected directly to one electrode through a metal needle (placed in the center of the droplet). The ground electrode is covered by a thin dielectric

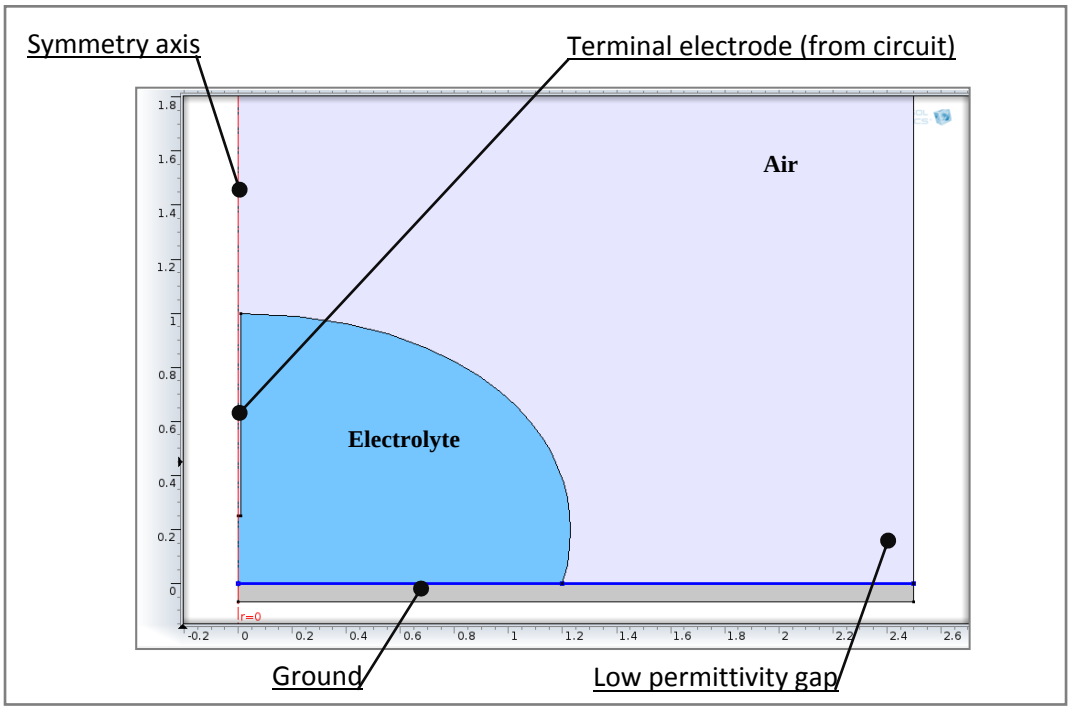

Figure 2-5: *Droplet-based electrowetting device geometry with highlighted ES boundary conditions.*

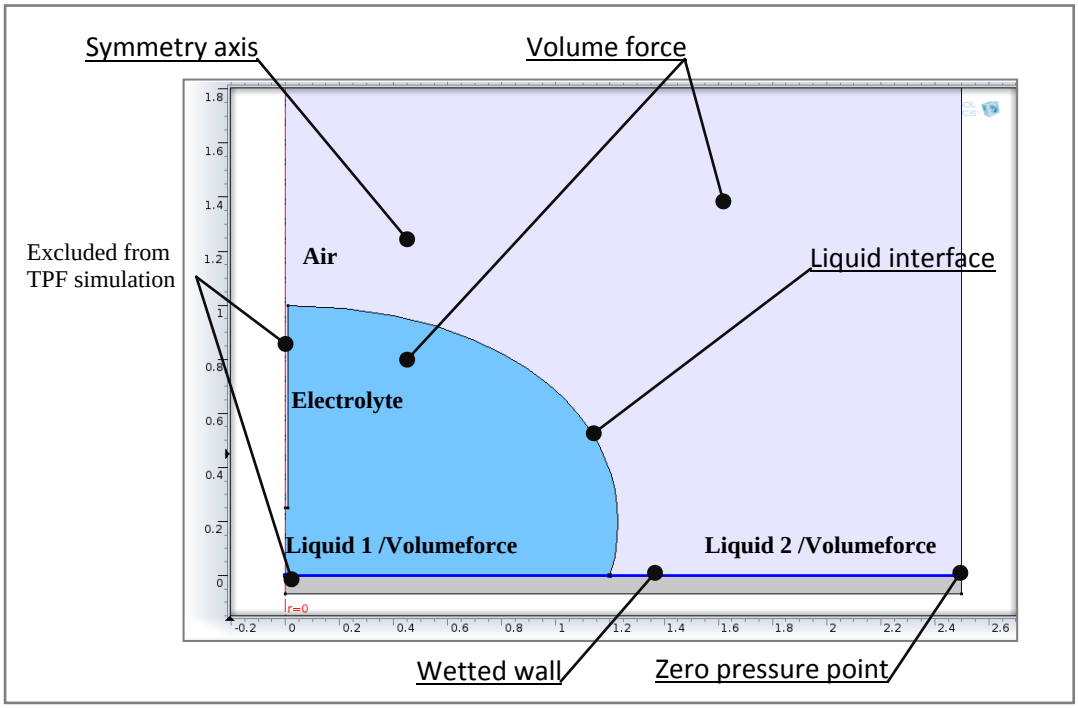

Figure 2-6: *Droplet-based electrowetting device geometry with highlighted TPF boundary conditions.*

Boundary conditions for the electrostatic (ES) module

The two phase fluid module boundary conditions applied shown in Figure 2-6 and are the following:

- Fluid initial values
  - Electrolyte set to “fluid 1”.
  - Air set to “fluid 2”.
- Volume force
  - Applied over the whole geometry by specifying *Fx* and *Fz* as horizontal and vertical volume force.
- Initial interface
  - Interface between electrolyte and air. The initial contact angle as 100°.
- Constant pressure point
  - Set up choosing the lower right corner, in order to make the system to converge.
- Wetted wall
  - Slip, allowing the fluid to move over the surface

Study definition

The study is defined as previously:

- Phase initialization
    - Only TPF selected
    - Values of dependent variables
        - Initial expression
        - Zero Solution
- Time dependent transient
    - Time range: range (0,0.01/999,0.01)
    - All physics selected and activated (CIR, ES, TPF)
    - Values of dependent variables
        - Solution
        - Study 1 Phase initialization.

2.4.2 Post-processing of the liquid drop simulation

The post-processing is carried out by using the embedded post processor of Comsol. By plotting tpf.Vf1 as surface plot, the result is shown in Figure 2-7a and Figure 2-7b, where the droplet shape is compared at time *t=0s* and at time *t=0.1s*; the contact angle is plotted in function of the time in Figure 2-9 and it is shown the contact angle reaches the theoretical value for the physical properties used in the material and system description, that is 67.2V. In Figure 2-8a is plotted the voltage across the whole system, taking into account the propagation across the liquid, the air and the metal beneath the droplet.

The electrostatic force calculated using MST is shown plotting "*Fr*" over the interface between the liquid and air. The plot is shown in Figure 2-8b: the electrostatic force component in r-axis is plotted in function of the arc-length of the interface. In the left side is plotted the value of the highest point of the droplet (the upper center) while at the right side the value corresponds at the point where liquid touches surface, the TPL. The result is that at TPL, the electrostatic force is considerably higher. Finally, in Figure 2-10 is shown a pseudo 3D representation of the droplet before and after applying a voltage, obtained by a revolution of the 2D results.

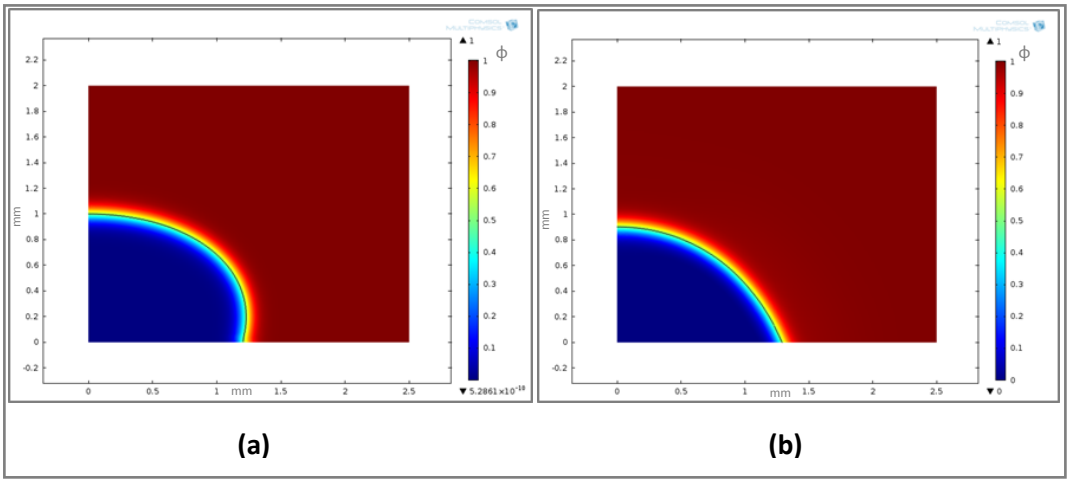

Figure 2-7: *In the picture is shown the liquid drop a) at the first simulation step and b) at the last one. Contact angle changed significantly. The color scale represents the CFD variable* ϕ.

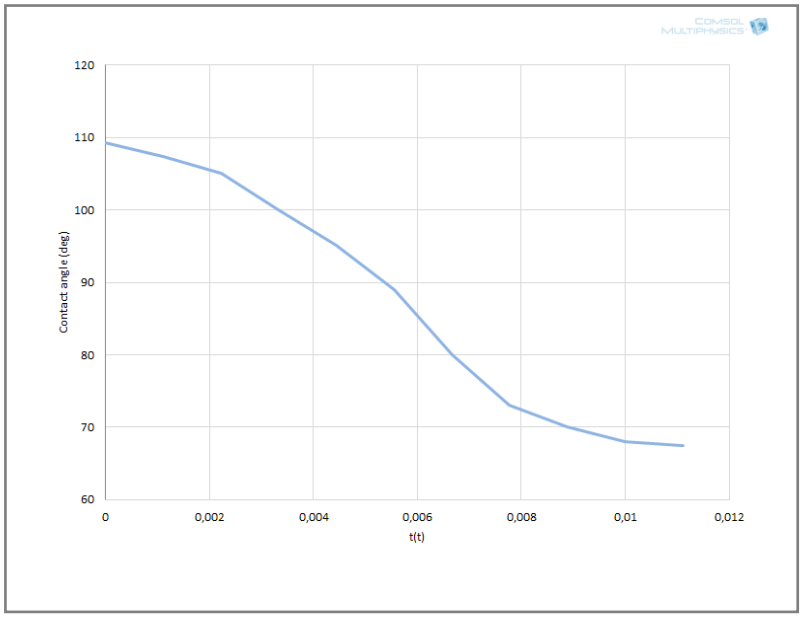

Figure 2-9: *Contact angle calculated at the TPL of the droplet in function of the time for a voltage source supplying 70V*

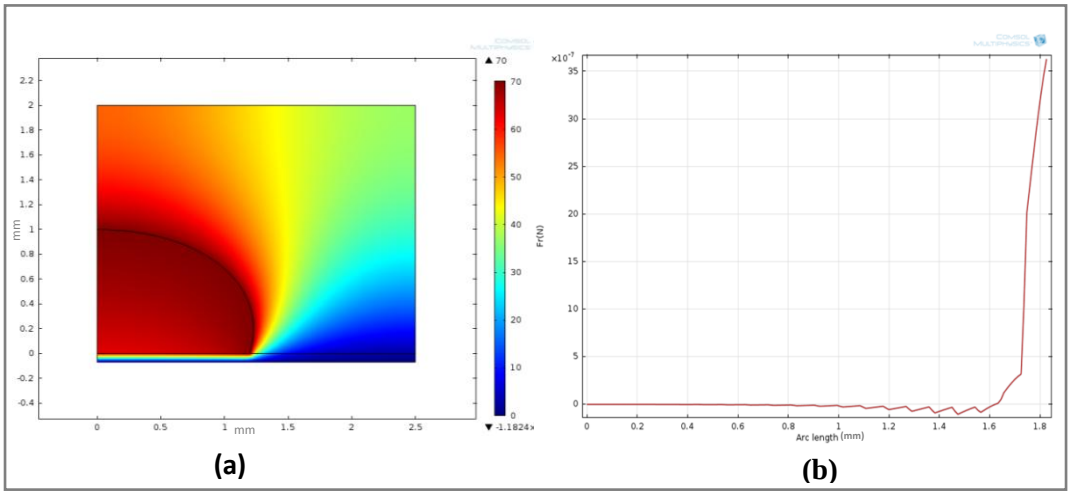

Figure 2-8: *a) Voltage across the drop and b) Electrostatic force calculated over the interface between the liquid droplet and air. The left most side of the plot is representing the very central area of the droplet, while the right side of the plot is the TPL. It can be seen that the electrostatic force increases strongly on the drop edge.*

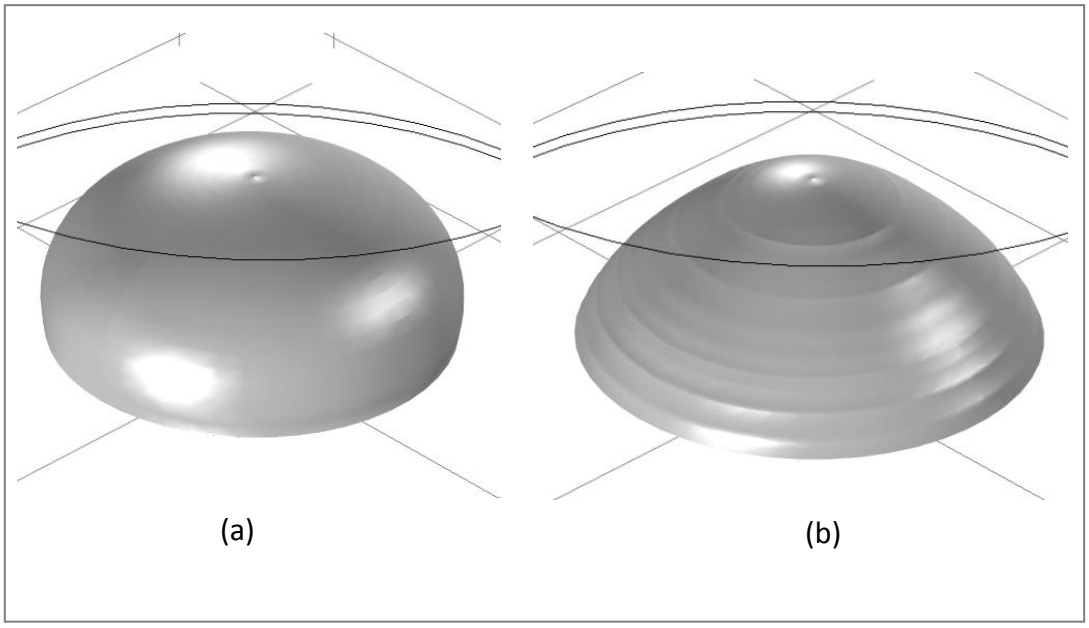

Figure 2-10: *Picture of the droplet obtained by revolving a 2D solution and applying iso-surface. In this way it can be obtained a pseudo 3D representation of the droplet a) before and b) after applying a voltage.*

2.5 Electrowetting pixel simulation

As described in Chapter 1, the electrowetting pixel is based on the interaction of a colored dielectric fluid, typically oil, and a transparent conductive electrolyte, packed together in a "tub"-like structure obtained by fabricating walls, that contains the oil and it is surrounded by the electrolyte, Figure 2-11.

The pixel surface, where oil sits, is hydrophobic, typically Teflon. When no voltage is applied, the oil wets the hydrophobic surface, avoiding the light to pass through the pixel. When the voltage is applied, the electrolyte, willing to wet the Teflon surface, displaces the oil that remains confined in a side region of the pixel. The most of the pixel area is now transparent and able to leave light shining through.

If voltage is removed, the oil flows to wet again the hydrophobic surface and acts as an optical curtain. The typical structure of an electrowetting pixel is shown in Figure 2-11. The geometry is designed in Comsol as shown in Figure 2-12. Only a section of the pixel is simulated as the amount of memory and processing power involved into the simulation of 3D structures like this pixel is huge. Nevertheless, taking into account that the structure has symmetry, only half of the section is represented. Even though the structure is simple and small, the simulation takes generally hours to be solved. This kind of structure with thin layers moving are very demanding in memory and processing power.

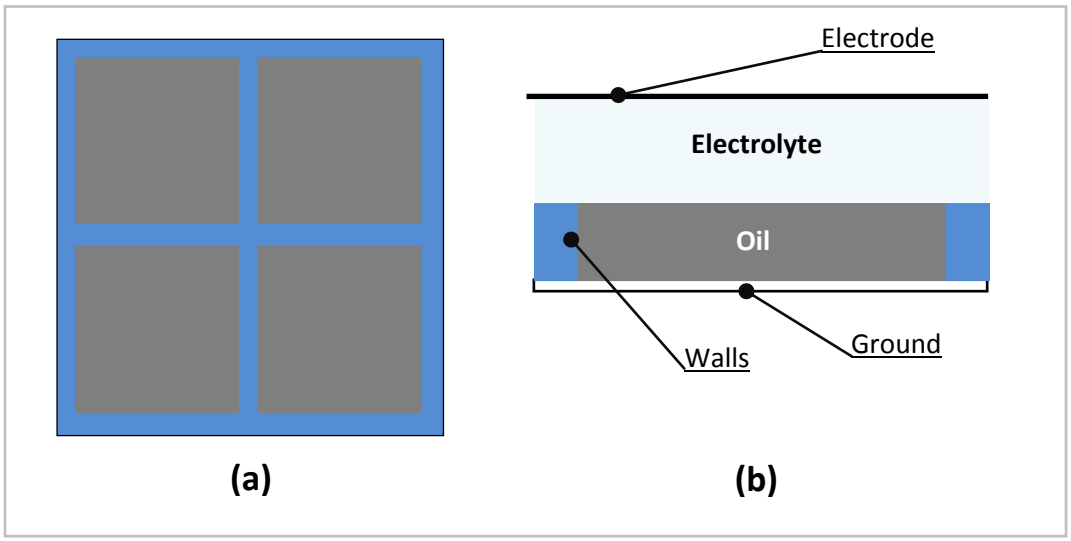

Figure 2-11: *Typical electrowetting pixel structure where a)several pixels are divided by walls and b) the wall only serves as constraint to avoid the black oil to invade the active matrix contiguous zone.*

The boundary conditions for the circuit module (CIR) remain the same, while for the electrostatic (ES) and fluidic (TPF) module boundary conditions are defined differently and they are shown in the next Sections.

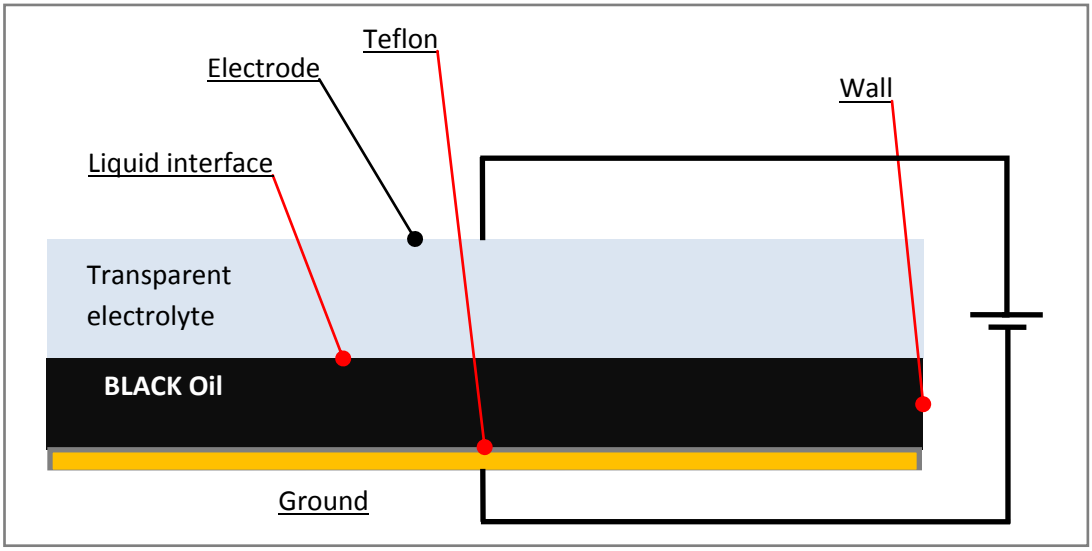

Figure 2-12: *Geometry designed to be simulated. Only interactions between fluids are interesting. Walls are omitted as the dielectric effect can be achieved by surface boundary conditions.*

2.5.1 Boundary conditions setup for the electrowetting lens simulation

Boundary conditions for the Electrostatic (ES) module

The electrowetting pixel is packed between two glass plates covered with a transparent conductive material. The plate in contact with oil is also coated with Teflon. The ground electrode is placed beneath the oil surface, while the voltage terminal is put in contact with the transparent electrolyte.

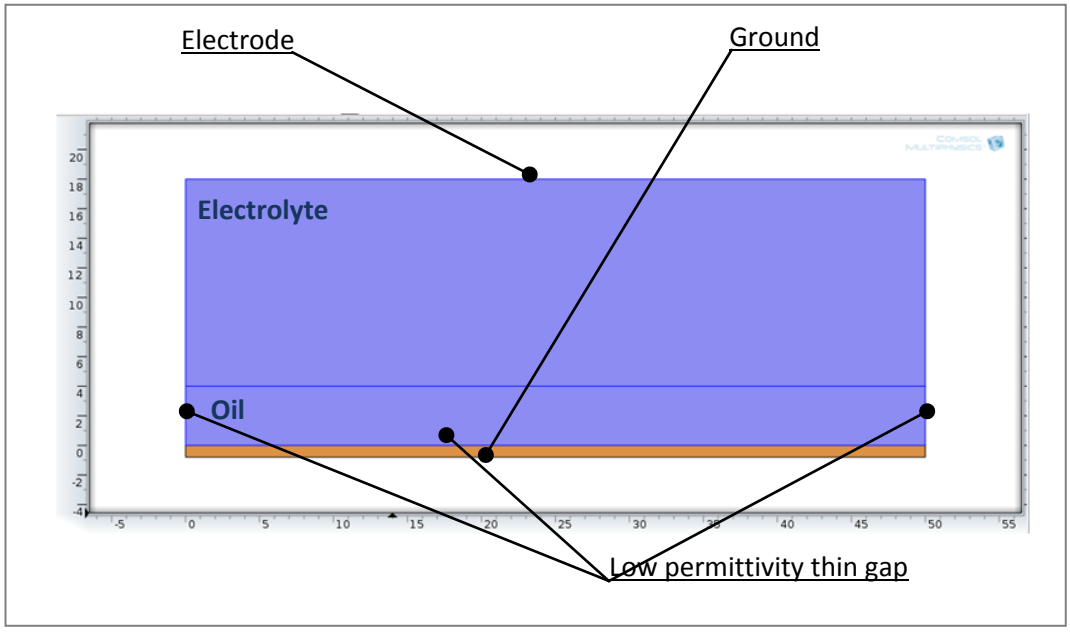

Figure 2-13: *Electrowetting pixel geometry simulated with highlighted ES boundary conditions*

The electrostatic module boundary conditions applied shown in Figure 2-13 are the following:

- Ground
  - Chosen as the lower area beneath the oil
- Terminal
  - Chosen the surface in contact with electrolyte and connected to the CIR module.
- Thin low permittivity gap
  - The hydrophobic Teflon layer, 0.8µm thickness and dielectric constant 1.9.
  - The side walls, 4µm and dielectric constant 2.8 (SU8)

Boundary conditions for the laminar two-phase flow (TPF) module

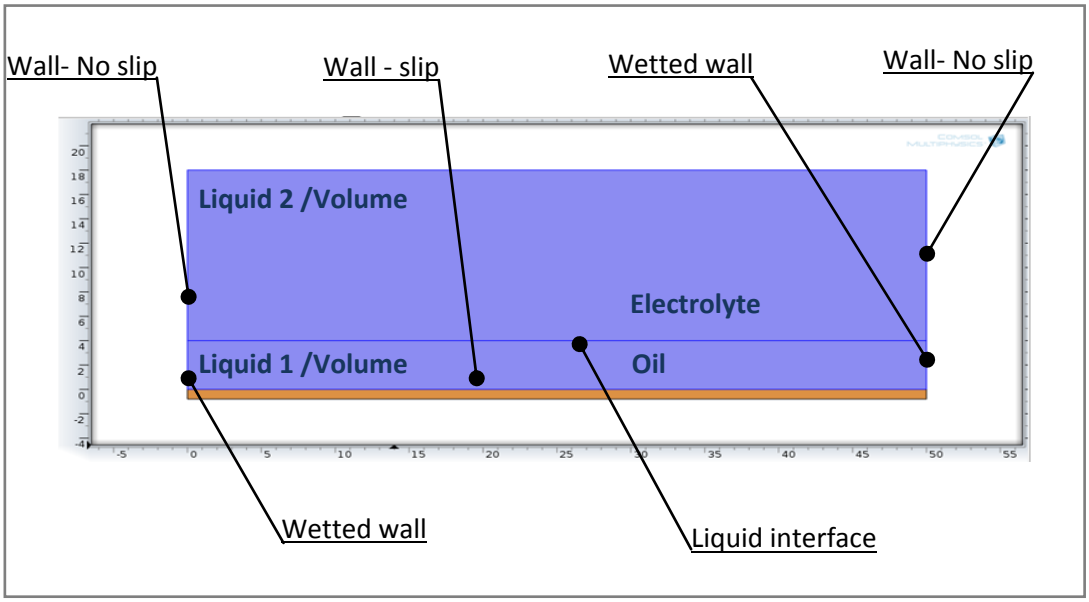

Figure 2-14: *Electrowetting pixel geometry simulated with highlighted TPF boundary conditions*

The two phase fluid module boundary conditions applied shown in Figure 2-14and are the following:

- Fluid initial values
  - Oil set to “fluid 1”.
  - Electrolyte set to “fluid 2”.
- Volume force
  - Applied over the whole geometry by specifying *Fx* and *Fz* as horizontal and vertical volume force.
- Initial interface
  - Interface between electrolyte and oil.
- Constant pressure point
  - Set up choosing the lower right corner, in order to make the system to converge.
- Wetted wall
  - Slip, allowing the fluid to move over the surface

The side walls are defined as wetted wall with a contact angle of 85˚.

Study definition

The study is defined as previously:

- Phase initialization
    - Only TPF selected
    - Values of dependent variables
        - Initial expression
        - Zero Solution
- Time dependent transient
    - Time range: range (0,3.0e-4/30,3.0e-4)
    - All physics selected and activated (CIR, ES, TPF)
    - Values of dependent variables
        - Solution
        - Study 1 Phase initialization.

2.5.2 Post-processing of electrowetting lens simulation

In Figure 2-15 it is reported the plot of the electrowetting pixel closed, Figure 2-15a with the detail of the oil touching the side wall with an angle of 85˚. As soon as the electrostatic force acts, the oil is pushed away until reaching equilibrium, being contracted and in contact with the opposite side of the pixel.

In Figure 2-16 it is shown the electrostatic force (white arrows) acting over the oil. In Figure 2-16a, the electrostatic force pushes oil to contraction. In Figure 2-16b, just before reaching the equilibrium point, it is plotted the residual electrostatic force and in addition the voltage field all over the pixel area. In oil domain the voltage is influenced by the dielectric nature of the material.

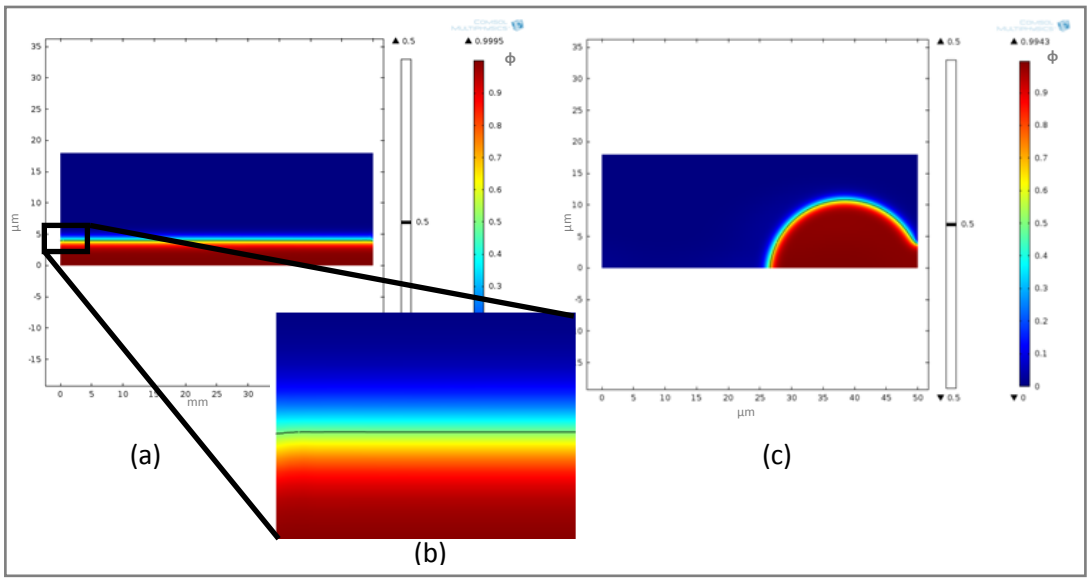

Figure 2-15: *a) EW pixel with oil covering the surface, no voltage applied; b) detail of the interface between the oil and the wall: 85˚contact angle between oil, electrolyte and wall. C) When voltage is applied the oil contracts and lets electrolyte wetting the bottom surface.*

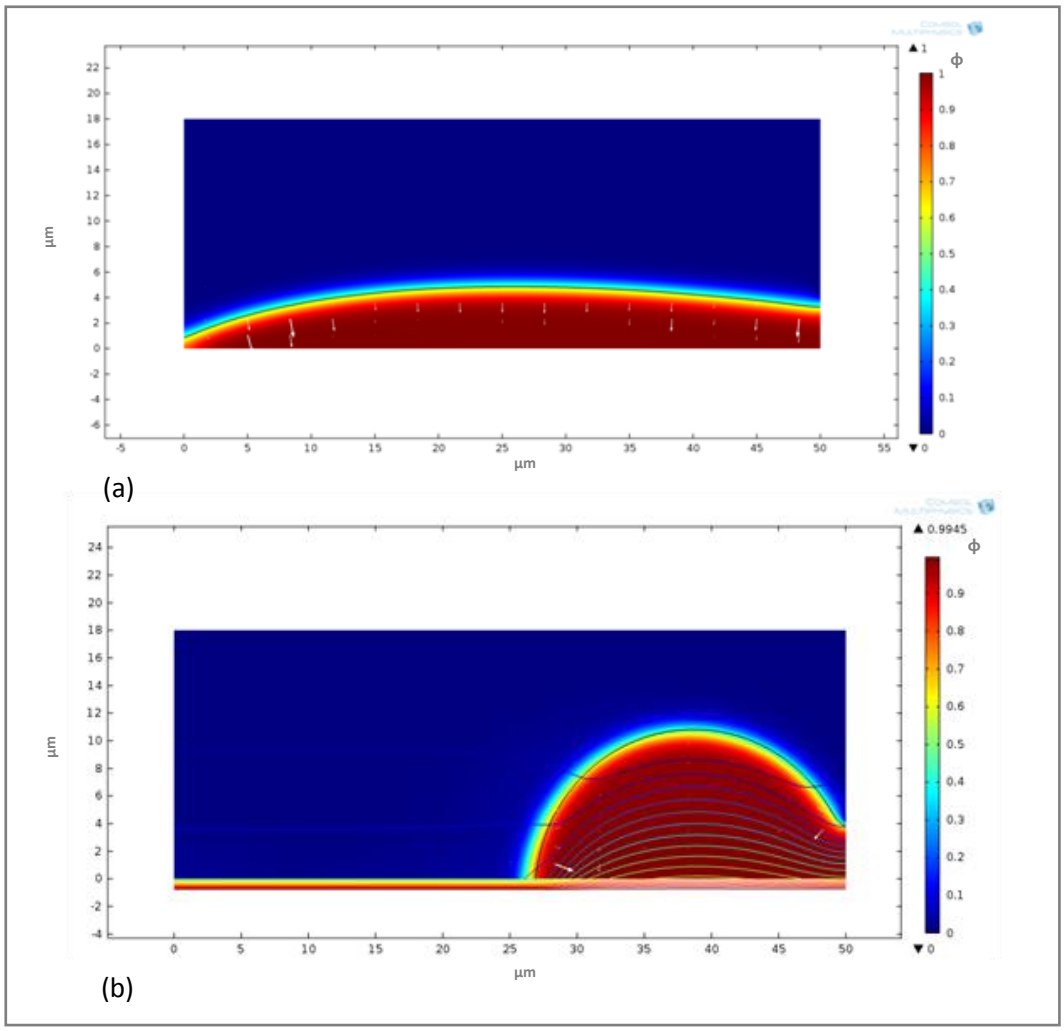

Figure 2-16: *a) Plot of the initial stage of the pixel opening: the electrostatic force pushes away oil from the wall surface and b) reaches the equilibrium. In the plot shown in b) it is also represented the voltage across the oil drop.*

In Figure 2-17 it is shown the velocity field of the liquid enclosed in an electrowetting

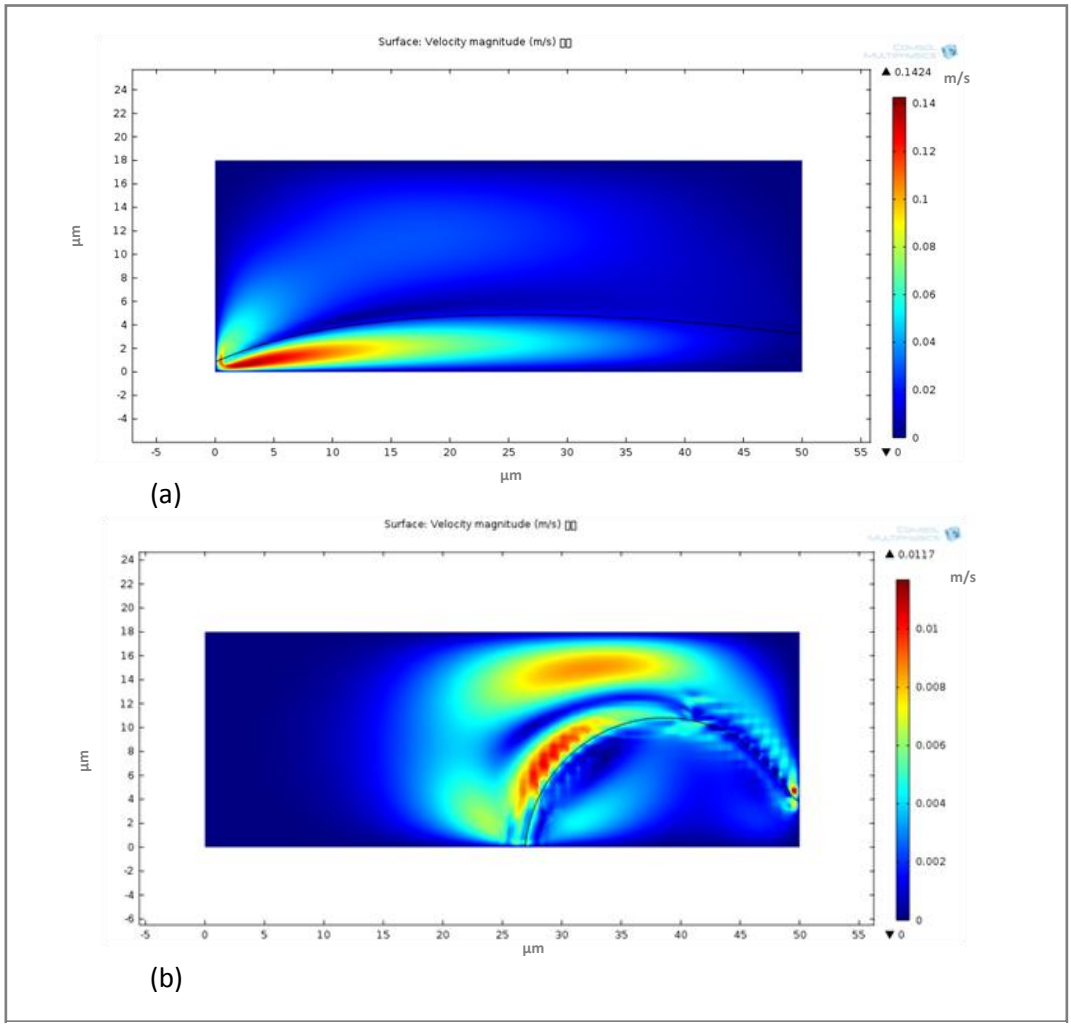

Figure 2-17: *a) Velocity field of the liquid while oil contracts, at the very beginning of the opening and b) reaching the equilibrium point.*

pixel. The liquid starts experiencing a velocity increase at the TPL, Figure 2-17a, and when the system reaches the equilibrium, the oil is almost completely contracted onto the opposite side wall, Figure 2-17b, the electrolyte flows over the droplet.

The recirculation of the fluid at high velocities inside the pixel enclosure limits the switching speed performance and efficiency of the device: energy is dissipated due to fluid-fluid interactions and fluid-surface frictions are linearly dependent with speed. Simulations help to understand how fluid recirculation happens in order to limit energy losses.

2.6 Electrowetting lenses simulation

Electrowetting lenses, shown in Chapter 1, are very interesting application for high end compact camera sensors, i.e. on smart-phones. The special interest is that the focal depth this kind of lenses can reach is not possible to achieve with standard mechanical lenses.

The limitation of standard lenses is the fabrication of actuators that move the lenses and the packaging in few cubic millimeters volume. Electrowetting lenses solve the problem.

Electrowetting lenses do not need any moving part for the actuation; in fact, only the electrodes and liquids are involved in focal variation.

The dynamics of the lenses, anyway, are not easy to control due to hysteresis, electrode shape difficult to fabricate and high voltage required for the liquid shape control. In addition side effects like pinning and hysteresis are limiting electrowetting lens performances. Multiphysic electrowetting simulations are very handful for preliminary studies and early design validation.

The simulation conditions for the CIR, ES and TPF modules are the same as shown in Section 2.4, with the exception that instead of air, oil is used, therefore for the dielectric phase the parameters to be used are the corresponding to oil in Table 2-1.

Boundary conditions for the *electrical circuit module (CIR)* do not change in comparison to Section 2.4 and they are not reported here. Volume force, calculated using Maxwell Stress Tensor is the same, therefore the full list of equations can be imported as a .txt file. Specific boundary conditions for ES and TPF modules set up differently for this geometry are reported following.

2.6.1 Boundary conditions setup for the electrowetting lens simulation

The electrowetting lens simulated structure is shown in Figure 2-18. It consists in a stack of transparent electrolyte and dielectric oil, packed into a closed round packaging where the ground electrode is placed beneath the hydrophobic surface where dielectric oil is sit, while the biasing electrode terminal is buried beneath a hydrophobic Teflon layer.

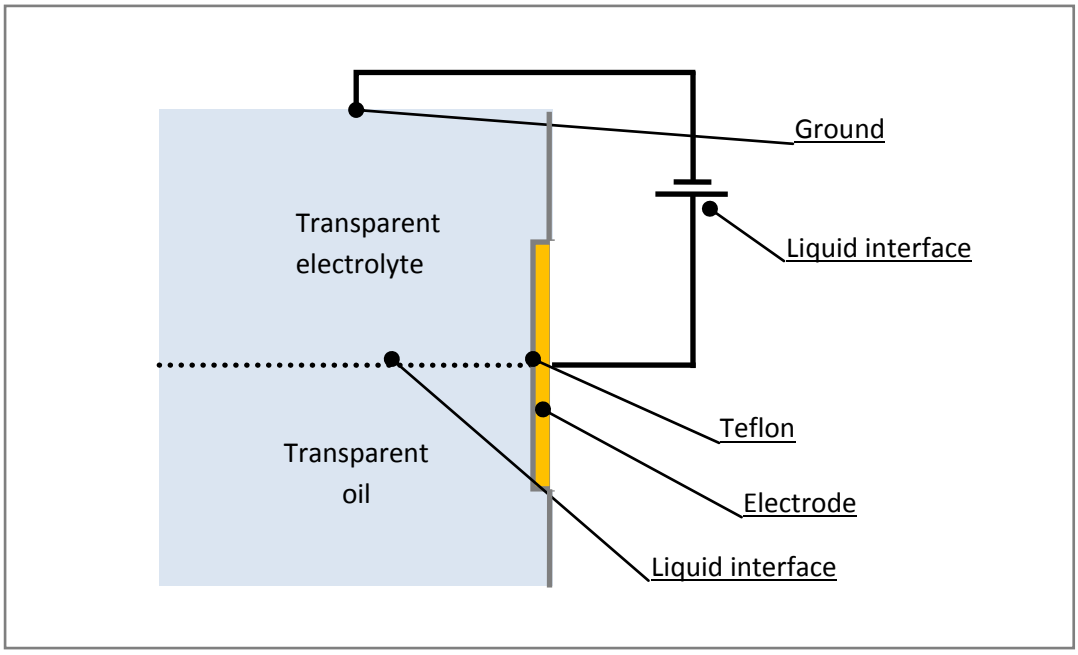

Figure 2-18: *Schematic of the electrowetting lens structure simulated in Comsol.*

The interface of the two liquids is reported at the middle of the structure. A voltage supply is connected between ground and terminal.

The simulation is performed taking into account that the system has a cylindrical symmetry, therefore only a section of the system is simulated and afterwards it is transformed to get a 3D representation of the results, as shown for the droplet-based simulation in Figure 2-10.

Boundary conditions for the Electrostatic (ES) module

The electrostatic module boundary conditions applied are shown in Figure 2-19 are the following:

- Ground
    - Chosen as the upper wall in contact with the transparent electrolyte.
- Terminal
    - Chosen as the area buried beneath Teflon hydrophobic layer and connected to the CIR module.
- Thin low permittivity gap
    - The hydrophobic Teflon layer, 1µm thickness and dielectric constant 1.9.

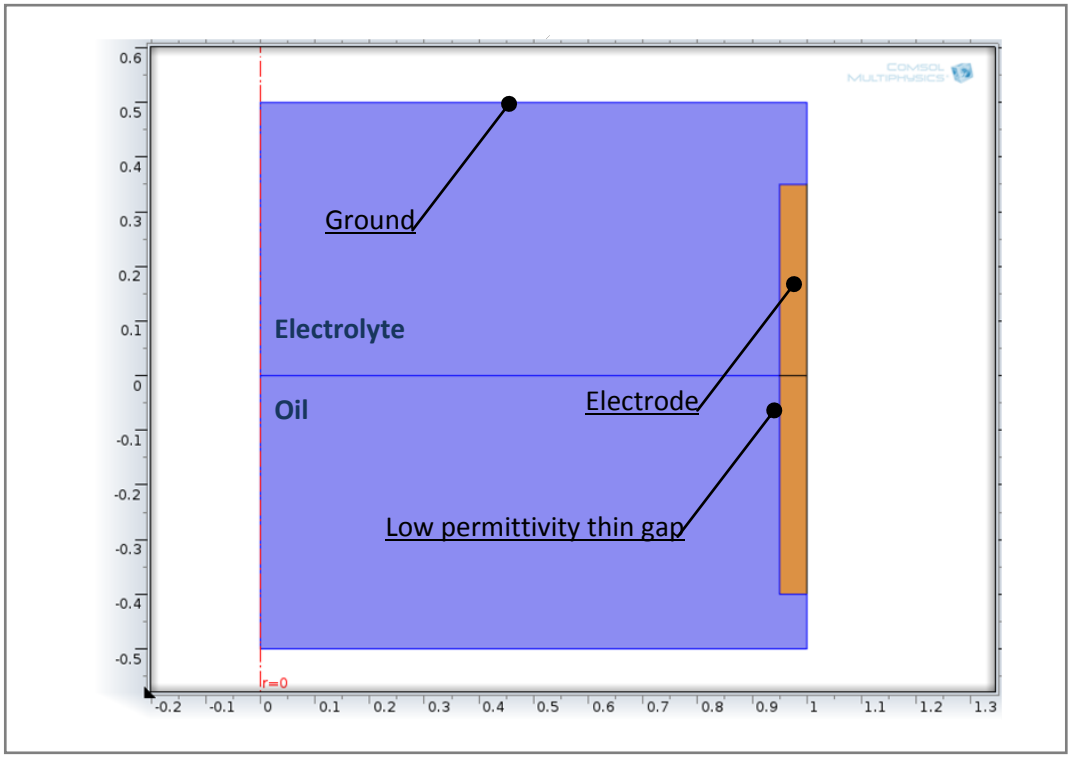

Figure 2-19: *Electrowetting lens geometry simulated with highlighted ES boundary conditions.*

Boundary conditions for the laminar two-phase flow (TPF) module

The two phase fluid module boundary conditions applied are shown in Figure 2-20 and are the following:

- Fluid initial values
    - Oil set to “fluid 1”.
    - Electrolyte set to “fluid 2”.
- Volume force

- Applied over the whole geometry by specifying *Fr* and *Fz* as horizontal and vertical volume force.

- Initial interface
  - Interface between electrolyte and oil.
- Constant pressure point
  - Set up choosing the lower right corner, in order to make the system to converge.
- Wetted wall
  - The hydrophobic layer is defined as wetted wall with a contact angle of 85˚.

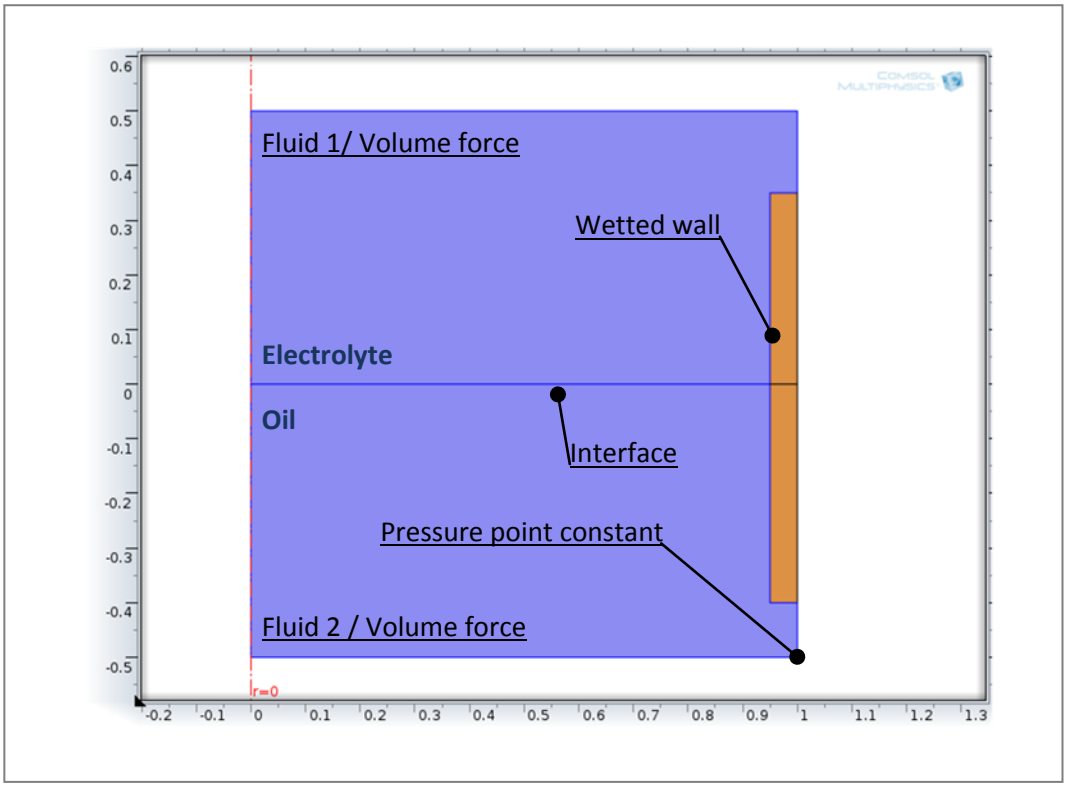

Figure 2-20: *Electrowetting pixel geometry simulated with highlighted TPF boundary conditions.*

Study definition

The study is defined as previously:

- Phase initialization
  - Only TPF selected
  - Values of dependent variables
    - Initial expression
    - Zero Solution
- Time dependent transient
  - Time range: range (0,0.01/19,0.01)
  - All physics selected and activated (CIR, ES, TPF)
  - Values of dependent variables
    - Solution
    - Study 1 Phase initialization.

2.6.2 Post-processing of electrowetting lens simulation

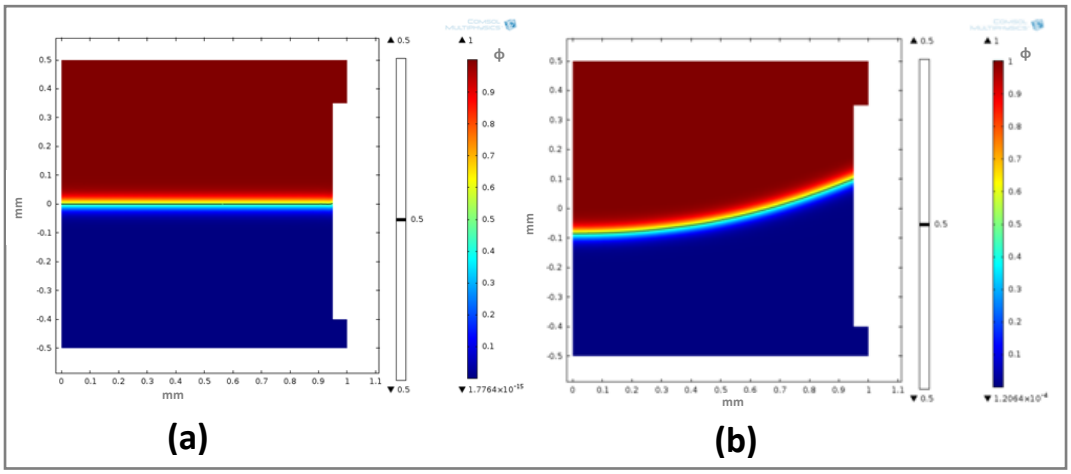

Figure 2-21: *a) Electrowetting lens prior the application of voltage at the electrodes (70V) and b) after applying the voltage.*

In Figure 2-21 is shown the picture of the geometry studied in Comsol, before and after applying voltage to the electrodes. In Figure 2-22 is shown the pseudo 3D representation of the liquid bending, obtained by performing a 3D revolution of a 2D simulation result set and finally, applying an isosurface to 0.5 phase field level in order to see the liquid interface only. Lateral and Iso views are reported.

The measurement of the volume force, bending the liquid interface is shown in Figure 2-23. The z-component of the force has been measured along the liquid interface at time *t=0*. As expected, it is maximum at the left side, where triple contact line is, and close to 0 in the middle, where electric field is also very low.

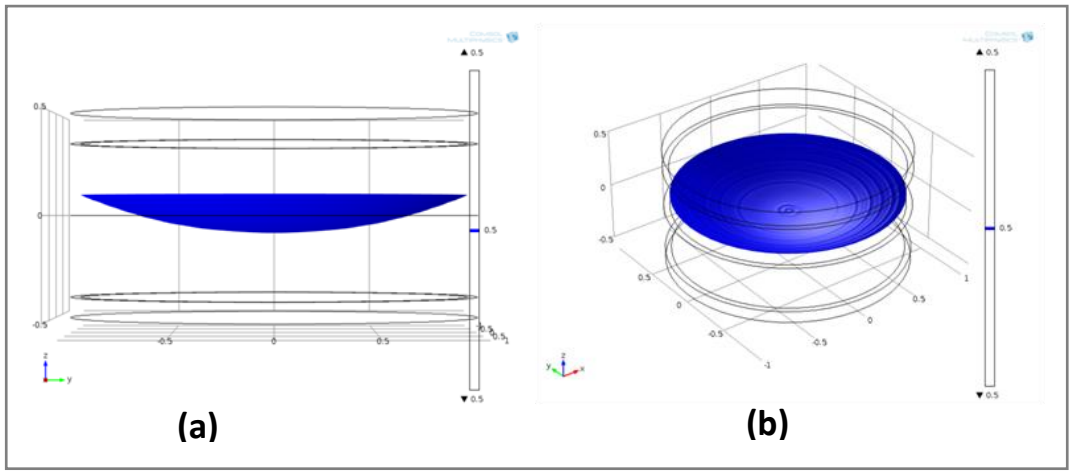

Figure 2-22: *a) Electrowetting lens prior the application of voltage at the electrodes (70V) and b) after applying the voltage.*

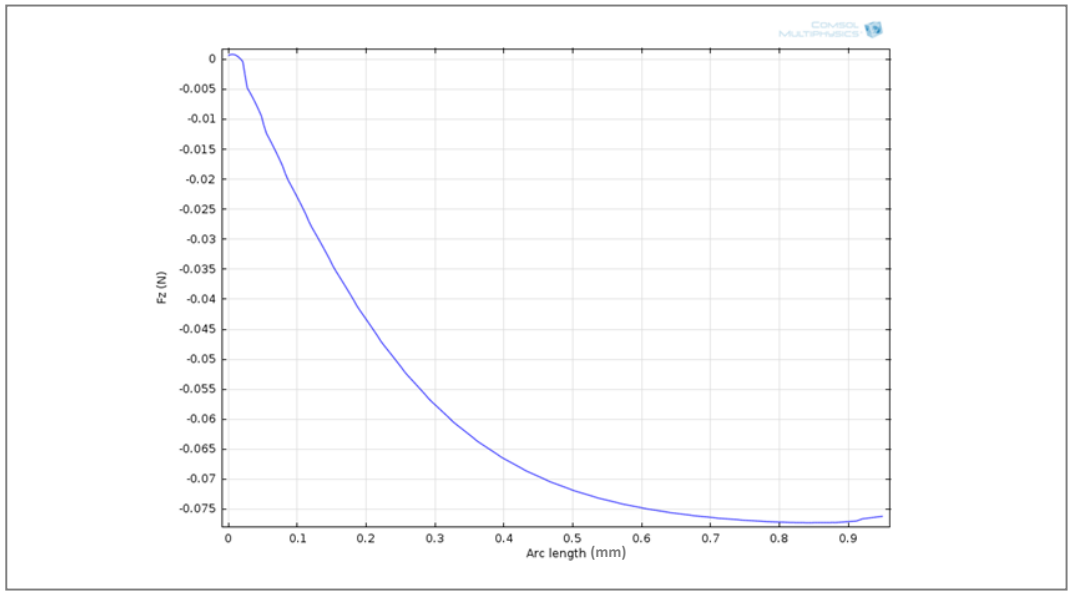

Figure 2-23: *Force (z component) along the liquid interface. The value is high at the right side, corresponding to the TPL and driving the system by contact angle variation.*

In Figure 2-25 is reported the simulation of the speed of the liquid when the lens is actuated. It is clear the liquid moves faster at the center of the geometry, where the liquid interface experiences the most of the movement.

On the other side, at the TPL, it is measured the contact angle in function of the time, reported in Figure 2-24. Contact angle varies suddenly when voltage is applied and it experiences a very noticeable ripple in the beginning, when the steady state is not yet reached.

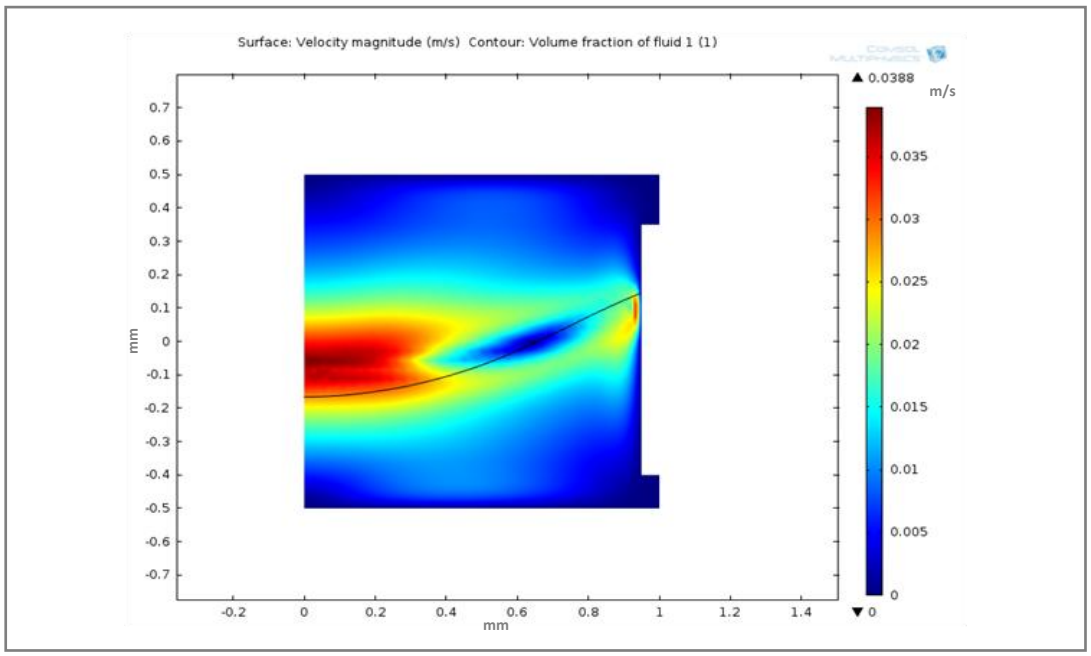

Figure 2-25: *Velocity field inside the electrowetting lens, showing the fluid dynamics inside the packaging.*

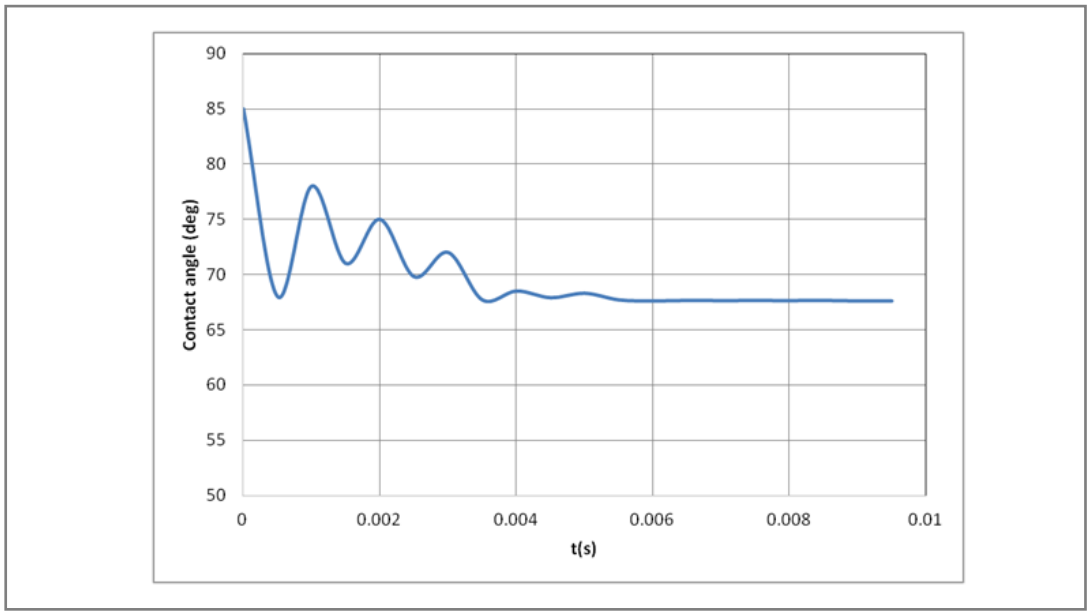

Figure 2-24: *Contact angle in function of the time for an electrowetting lens biased with a 70V voltage source.*

2.7 Conclusions

In this Chapter has been shown a comprehensive step by step guide useful to perform a full multiphysic simulation of an electro-hydrodynamic system.

The major contribution is the link between electrostatics and fluid dynamics; Maxwell Stress Tensor has been defined as a volume force in order to couple the effects of voltage to the dynamics of the liquid interface.

Moreover, it has also shown a way to introduce non linearity, parasitic effects and dynamics of a power supply by simulating a circuit and feeding with it the full model, or just import a model previously simulated or given by the manufacturer.

Quick results have been shown by post-processing data for the three major electrowetting on dielectric configurations: the drop-based experiment, the electrowetting pixel and the electrowetting lens.

Annenx II describes more in detail the comsol comands used and the simulation step-bystep procedure in order to help the reader understanding the simulations.

Chapter 3: Contactless electrowetting

Contactless electrowetting is a technique that allows modifying the contact angle by air ionization. The liquid is in contact only with the surface beneath. The contact angle is modified by charge accumulation at the triple contact line.

3.1 Introduction

Liquid handling in extremely safe and clean conditions plays a very important role in applications such as μTAS and integrated analysis systems. More important is the need to limit contamination and interactions with the liquid, which may lead to jeopardized results of essays and tests.

Typically, in EWOD-based microfluidics, the drop is confined and squeezed between two hydrophobic coated glass plates. The top glass has a continuous electrode that provides the electric contact for the capacitive coupling with the drop.

The interaction area of the liquid is indeed double, having to flow touching constantly the top and bottom plate, that converts in more pinning probability of the TPL with the surface, more friction, therefore poorer handling performances. In addition, possible interactions between any remnants of previously manipulated liquids with the actual manipulated drop are doubled.

Satoh et al. proposed an open channel solution[46] for the liquid handling; nevertheless it is still performed along specific paths addressing to specific electrodes an electrical pulse sequence; the side effect of the standard actuation by electrical pulses is that dielectric breakdown can easily occur[47].

In this chapter a novel technique for contactless electrowetting on dielectric actuation is reported. Contactless techniques for plasma separation in blood samples were already proposed by Arifin et al.[48]. Nevertheless the actuation for samples manipulation was performed by electrode addressing. Here it is proposed a technique to avoid electrode addressing for drop manipulation; charges stored at the TPL induce a selective wettability increase that finally results in a total net force for the drop propulsion.

3.2 First experimental evidences

The first experimental evidences of contactless electrowetting are reported in [49]. The air ionization was produced by using a commercial ion gun by Milty, showed in Figure 3-1, based on a piezoelectric generator. The device is manually triggered; the trigger produces a single shot discharge of negative or positive charges. When the gun trigger is pressed, negative charges are shot; releasing the trigger, positive charges are shot.

Figure 3-1: *Milty ion gun device*.

The ion gun has been characterized by measuring the current using an Agilent 4156C semiconductor analyzer. The measurement setup is made by a 4" copper disk connected

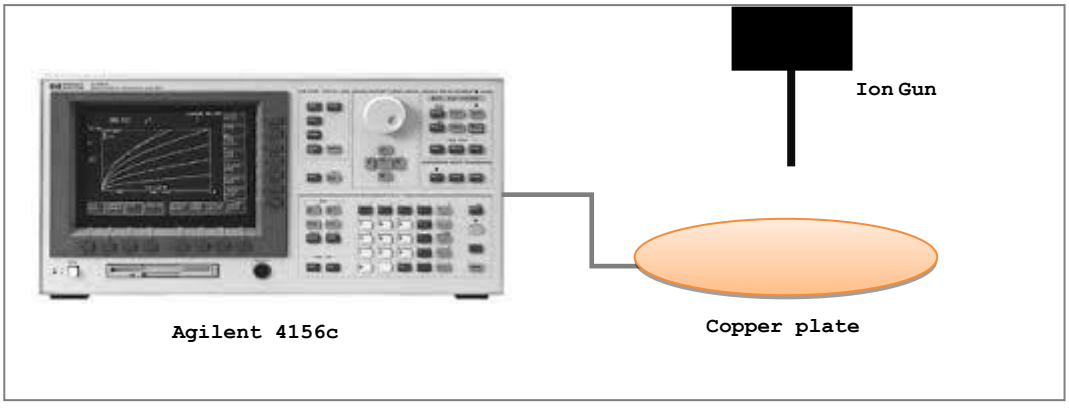

Figure 3-2*: Ion gun current measurement setup.*

to the equipment probe; the copper disk gathers all the charges when the ion gun is triggered in its vicinity at a controlled distance of 18mm. The measurement setup is shown in Figure 3-2.

The ion gun is triggered several times (hundreds) close to the copper disk. The data are recorded and the current over time is integrated by excel. The average is done by dividing the total charge by the number of shots. The result is the average charge delivered per shot is found to be 1.25μC. In Figure 3-3 is displayed a burst of ion gun shots over a 20 seconds time frame.

The first experiment has been performed as a trial on a single water drop sitting on a hydrophobic layer. The visual inspection determined that the contact angle was severely affected by the charge shot. In particular a hydrophilic behavior was observed; if the charge shot was performed on the Teflon surface, the most peculiar effect was that the drop was moving around, trying to find a position where to rest. The charge shot resulted as a propeller for the water drop.

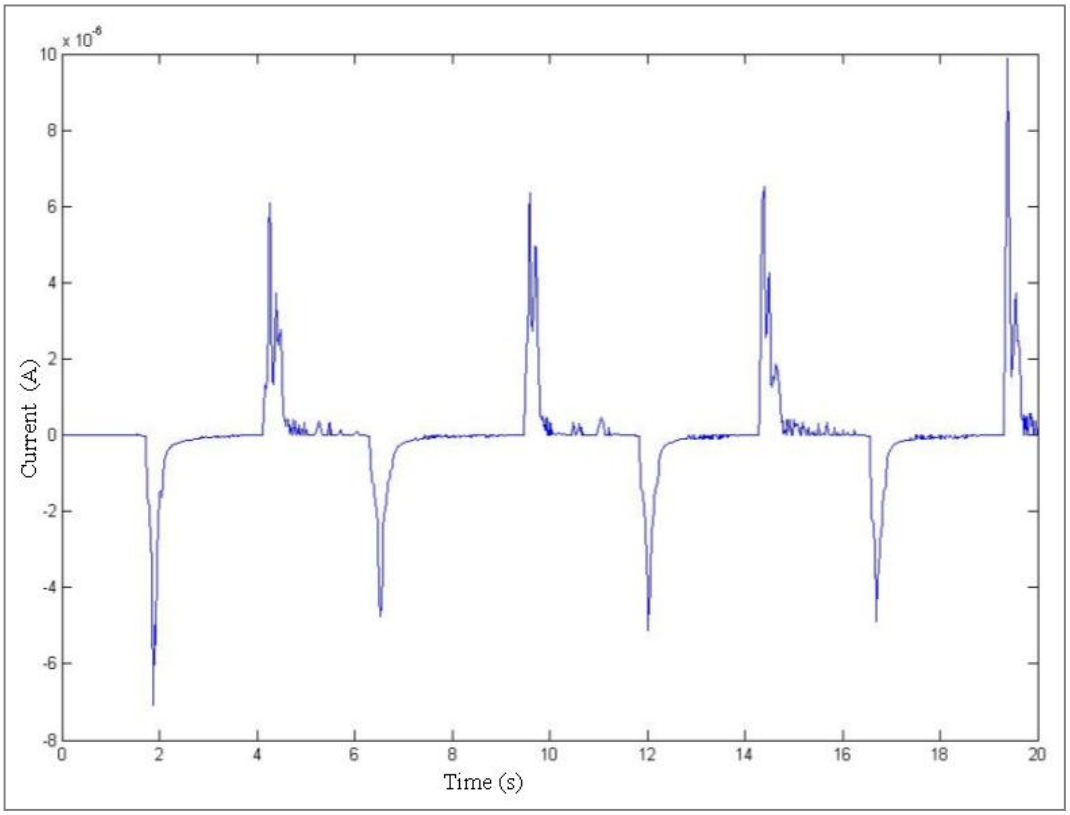

***Figure 3-3**: Current transient induced by a burst of ion gun shots in a 20s time frame. The measurement has been taken by measuring the charge with an Agilent 4156c.*

The contact angle is here the only measurable magnitude. As mentioned previously in Section 1.2, the Young-Lippmann equation, eq.(1-4), describes the contact angle variation in electrowetting. The origin of the contact angle variation is the electric charge stored per unit area capacitance; hence it is independent form the charge source. In this case

reported, no voltage is directly applied at the drop; the effect is instead ensured by ion gun charges.

Taking into account the capacitance C_A and charge Q_A per unit area

$$C_A = \frac{\varepsilon_0 \varepsilon_r}{t} \qquad (3\text{-}1)$$

and

$$Q_A = C_A V \qquad (3\text{-}2)$$

the Young-Lippmann equation (1-4) can be written as:

$$\cos\vartheta_V = \cos\vartheta_0 + \frac{Q_A^2}{2C_A\gamma_{LV}} \qquad (3\text{-}3)$$

In equation (3-3) the contact angle before applying charges, ϑ_0, and after applying charges, ϑ_V, can be directly measured; the capacity and charge per unit area can be calculated starting from the dielectric thickness and physical parameters of the system.

3.2.1.1 Device fabrication process

The electrowetting setup proposed for the first exploratory tests is composed by a set of devices constituted by a conductive substrate coated by a dielectric layer, which in this case was Teflon or Polydimethylsiloxane (PDMS). Figure 3-4 summarizes the three substrates used for the experiments.

The devices are different in fabrication. These differences have a reason. In order to compare the contactless electrowetting effect, standard electrowetting experiments must be carried out. The application of a high voltage often leads to a dielectric break out. A thin layer of PMDS on metal electrode is preferred because the behavior of this stack is much stronger than the Teflon coated one. Together with the dielectric strength, the PDMS shows nice results when the maximum voltage available (260V) is applied, resulting in a wide contact angle variation. On the other hand, the contactless electrowetting

showed good performances on devices with high dielectric thickness; thicker material could be applied in order to not reach the saturation or dielectric break out without major drawbacks in terms of response range. The results of the tests are reported in Table 3-1 while the visual inspections are resumed in Figure 3-6 and Figure 3-7.

3.2.1.2 Teflon coated devices fabrication process

The Teflon coating used for the preparation of the dielectric hydrophobic layer is the Teflon AF 400S1-100-1. The solution has not been diluted. The fabrication process flow for the device coating is described as following:

Substrate preparation:

- RCA cleaning and following dry oxidation for the growth of a 260nm oxide layer
- Piranha cleaning of the substrate
- HMDS coating 3500rpm for 60 seconds
- Curing 5 minutes at room temperature (RT).

Teflon coating:

- Spin coating of 3500rpm for 60 seconds
- 15 minutes at RT
- 12 minutes at 115°C on hotplate
- 15 minutes at 220°C on hotplate
- 30 minutes at 330°C in furnace.

The resulting coating is homogeneous and reproducible. The measured thickness is 1.2μm.

3.2.1.3 PDMS coated device process

The PDMS coating is simpler and more stable; on the other hand reaching a very thin layer is more difficult as the spin coating speed is very high. Two kinds of substrates have been coated with PDMS, a pirex glass/TiAg and a Si/SiO_2 substrate.

The pirex glass substrate has been prepared as following:

- Piranha cleaning of the glass
- Ti/Ag sputtering in Univex 250 equipment, 700nm layer thickness
- Piranha cleaning prior the PDMS coating.

The Si/SiO_2 substrate has been prepared as following:

- RCA cleaning and following dry oxidation for the growth of a 260nm oxide layer
- Piranha cleaning prior the PDMS coating

The PDMS has been prepared using the Sylgard 184 elastomer kit. The dilution between elastomer and curing agent has been done with a ratio of 1:10 V/V. The mix has been stirred vigorously, using a laboratory spatula and it has been degassed by putting the mixture in a vacuum chamber. The PDMS has been then applied by spin coating. Different spin speeds have been used. The best results in thickness and homogeneity of the PDMS layer have been:

- 1000rpm for 60 seconds on Si/SiO_2
- 5000rpm for 120 seconds on Ti/Ag

Following the spin coating, the PDMS has been cured at 70°C on hot plate for 30 minutes.

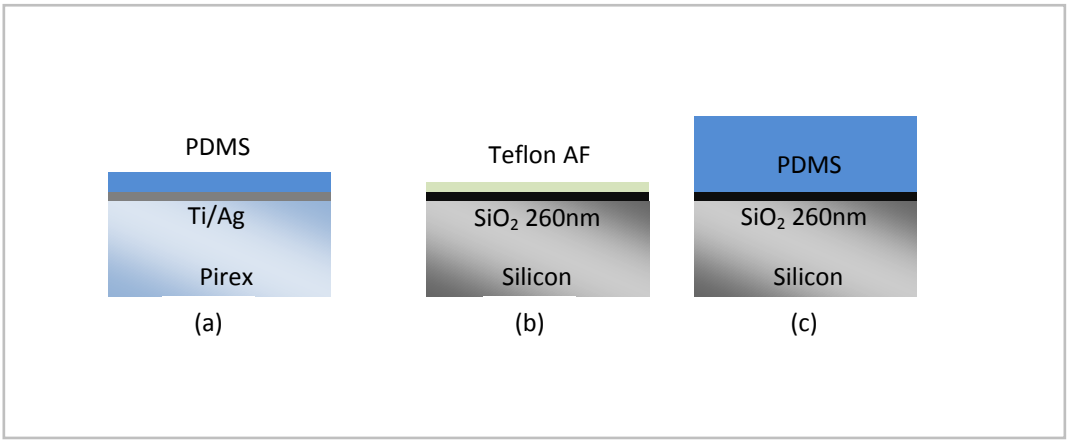

Figure 3-4: *Schematic view of the three types of devices used for the standard (a) and contactless (b and c) electrowetting experiments.*

3.3 Experimental setup and preliminary results

The experiments have been performed by monitoring the contact angle variation using a KSV CAM200 contact angle goniometer. For the standard electrowetting measurements, the voltage has been applied by connecting the system to a variable voltage supply, capable to provide 260VDC maximum. Contactless electrowetting experiments have been performed placing the ion gun on the top of the water drop at a fixed height of 8mm. The water drop dispensed was sat on the hydrophobic surface, just below the ion gun needle. The amount of water dispensed was 5 µl, the water was standard de-ionized laboratory water, semi-conductor grade.

The schematic arrangement of the experiments is shown in Figure 3-5.

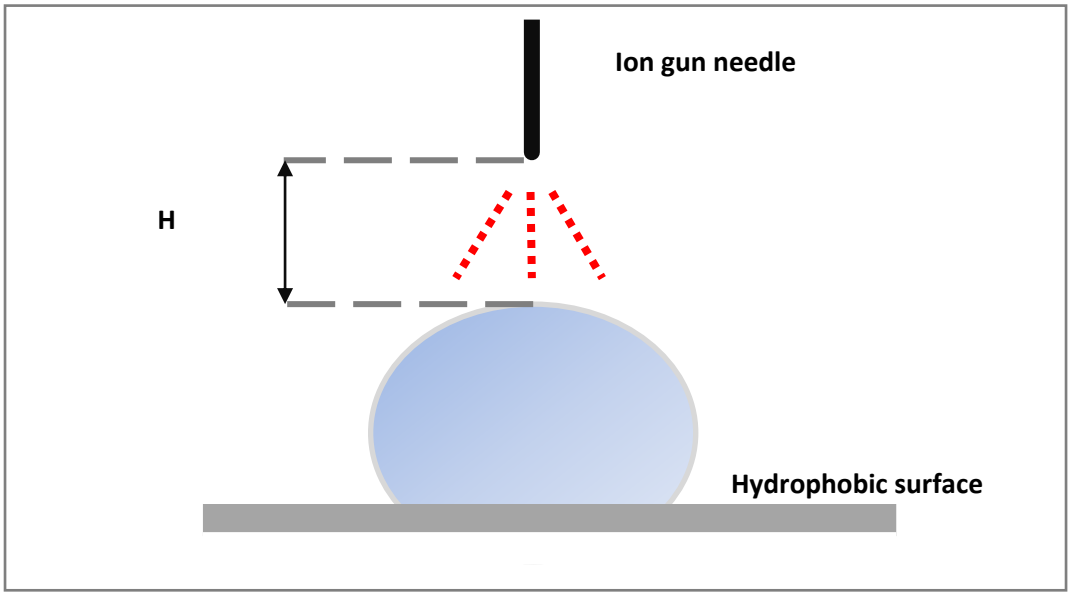

***Figure 3-5**: Schematic arrangement of the contactless electrowetting experiment.*

In Table 3-1 are reported the contact angle values recorded along the experimental session. The initial contact angle is very similar for the two coated surfaces and it is in the range of 108° in average, indicating that the hydrophobicity of both surfaces were quite similar; nevertheless a small asymmetry on the right and left sides of the drop is noticeable.

When ion gun is activated, a shot of negative charges is delivered and hence the contact angle varies. The contact angle variation behavior changes dramatically according to the dielectric coating used.

Table 3-1: *Summary of the results before and after ion gun shot*.

	Teflon AF (1.2μm)		PDMS (52μm)	
	Left	Right	Left	Right
Contact angle before ion gun activation	111°±1.2	106.4°±1.5	106.6°±1.4	107°±1.8
Contact angle after negative charges shot	100.1°±3.7	87.7°±4.1	57.2°±1.9	59.2°±2.2
Contact angle after spontaneous relaxation	110.2°±5.2	105.2°±4.9	71.8°±6.1	65.9°±7.1
Contact angle after a positive charge shot	-	-	102°±7.7	101°±6.9
C_A(F/m2)	$1.4x10^{-5}$		$4.8x10^{-7}$	
$Q_A^2=2\gamma_{LG}C_A(\cos\vartheta_V-\cos\vartheta_0)$ (L and R) (C^2/m^2)	$3.71x10^{-7}$	$6.55x10^{-7}$	$5.4x10^{-8}$	$5.27x10^{-8}$
$Q_A^2=2\gamma_{LG}C_A(\cos\vartheta_V-\cos\vartheta_0)$ (Averaged) (C^2/m^2)	$5.13x10^{-7}$		$5.335x10^{-8}$	

Case 1: Teflon coating

In the case of Teflon coating, the contact angle variation measured is modest and it is comprised between 10° and 20° as reported in Figure 3-6; high asymmetry between left and right side of the drop is also reported. The contact angle variation happens very fast when the ions are applied. Just after the ion shot is finished, the contact angle recovers the initial condition.

A peculiar behavior that is worth to be mentioned is the high instability of the drop on the substrate when the ion gun is activated. In case the needle was not perfectly in line with the drop center, the drop was propelled away from the needle vicinity, causing difficulties in reproducing a sufficient number of experiments on the same site. The speed induced to the water drop is measured in the range of 0.02m/s by dividing the distance between one frame and the other and dividing it by the sample time.

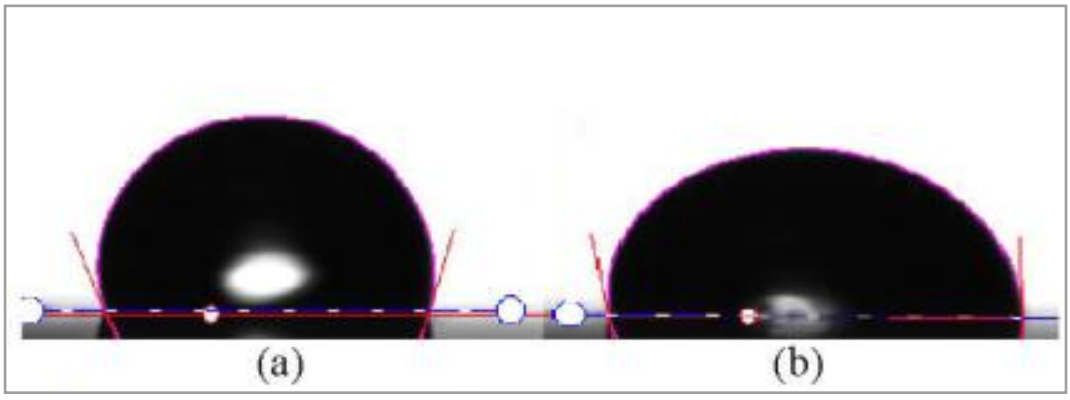

Figure 3-6*: a) shows the initial contact angle of a 5μL water drop sit on a Teflon coated substrate; b) shows the drop while experiencing the ion shot. Asymmetry can be noticed between the left and right side of the drop. Contact angle variation is poor.*

Case 2: PDMS coating

In the case of the PDMS coating device, the contact angle variation when ions are applied is in the range between 47.8° and 49°; the asymmetry is much smaller, being in the range of 10°. This trend is fully compatible with the C_A values, reported in the last row of Table 3-1, due to the different values of the coating thickness and dielectric permittivity.

An important observation that must be reported is a sort of memory effect of the contact angle variation after the ion shot. When negative charges are shot over the drop sitting on a PDMS coating device, the contact angle decreases dramatically and does not fully recover spontaneously, instead, it remains 31.4°-41.1° away from the initial conditions. In order to fully recover the initial state, a positive charge shot must be applied. In other words, the system is bi-stable and it is triggered by the applied ion sign.

In the case of the PDMS, this bi-stable effect is certainly due to the charge trapping effect[50, 8] at the interface between the PDMS coating and the metal surface.

Figure 3-7 shows the effect of the ion gun on the liquid drop, according to the substrate the drop is placed on. Figure 3-7a shows the drop on Teflon surface at rest; in Figure 3-7b the effect of ion shot is reported. A light displacement of the drop is noticeable. Figure 3-7c and Figure 3-7d depict the drop of water sit on a PDMS surface before and after the ion shot.

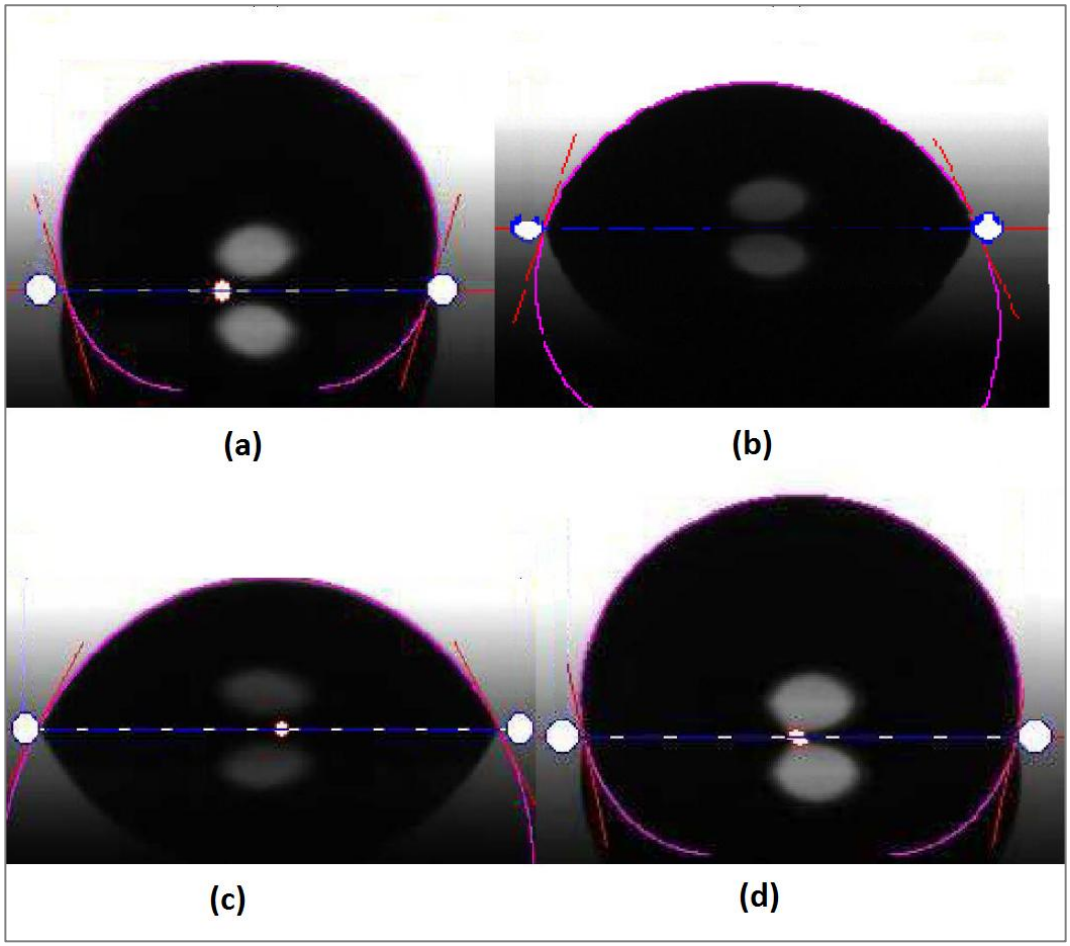

***Figure 3-7**: a) The water drop is sit at rest on a PDMS coated surface, no ions are applied. b) Ion gun is activated and the contact angle reduces to reach its minimum value. c) Ion shot is finished, the contact angle increases lightly but does not fully recover.*

3.4 Comparison between conventional and contactless electrowetting

In this section contactless electrowetting performance is compared with conventional electrowetting in order to validate and estimate what is the novelty impact of the technique. A set of complementary experiments have been performed using a 260VDC power supply in order to bias a 5µL water drop, in contact with a metal probe, reproducing a conventional electrowetting experiment setup.

The voltage has been swept from 0 to 260V in order to draw a complete curve and also the Lippmann-Young equation has been calculated for the devices under test.

As can be seen in eq. (3-3) in a given solid-gas-liquid interface, the real magnitude responsible for the contact angle change is the charge stored per unit interface area.

This is similar to what happens in electrostatic driven MEMS actuators where the charge stored bears the main responsibility for the electrostatic force developed between plates [51].

In order to plot on the same graph the conventional electrowetting and the contactless electrowetting experimental results, together with the Lippmann-Young equation, the following magnitude has been calculated:

$$Q_A^2 = 2\gamma_{LG} C_A (\cos\vartheta_V - \cos\vartheta_0) \qquad (3\text{-}4)$$

This magnitude represents the square of the charge stored per unit area for both contactless and conventional electrowetting experiments. The results are plotted in function of Q_A ($C_A V$) in Figure 3-8; for comparison, the theoretical values of Q_A^2 calculated from the Lippmann-Young equation are also represented in dashed line. Figure 3-8 is the log-log plot of the magnitude described above. The theoretical curve given by the Lippmann-Young equation is a straight line with a slope 2 (as Q_A^2 is represented in function of Q_A). The conventional electrowetting results do not follow the theoretical results; nevertheless a slope close to 2 can be identified in most of the range of values of Q_A explored. The two horizontal lines represented in Figure 3-8 are calculated for the contact angle variation due to air ionization on Teflon and PDMS substrates. The vertical lines intersect the conventional electrowetting experiments line at $4.4\text{x}10^{-4}$(C/m^2) in the case of devices coated with PDMS and at $1.1\text{x}10^{-3}$(C/m^2) in the case of devices coated with Teflon.

These resulting values can be easily transformed into an “effective voltage” that would lead to a similar contact angle variation in comparison with the conventional electrowetting setup. The effective voltage calculated for Teflon coated devices is V_{eff}=75.71V while for PDMS coated devices is V_{eff}=933.33V.

The summary of the first experimental results are:

1. Teflon coated devices show instability of the drop and low contact angle variation but high mobility of the drop, which can be very interesting if used in μTAS devices for drop manipulation.
2. PDMS devices show very high effective voltages with respect to the Teflon coated devices; nevertheless dielectric breakdown does not appear.
3. PDMS coated devices show a very interesting memory effect.

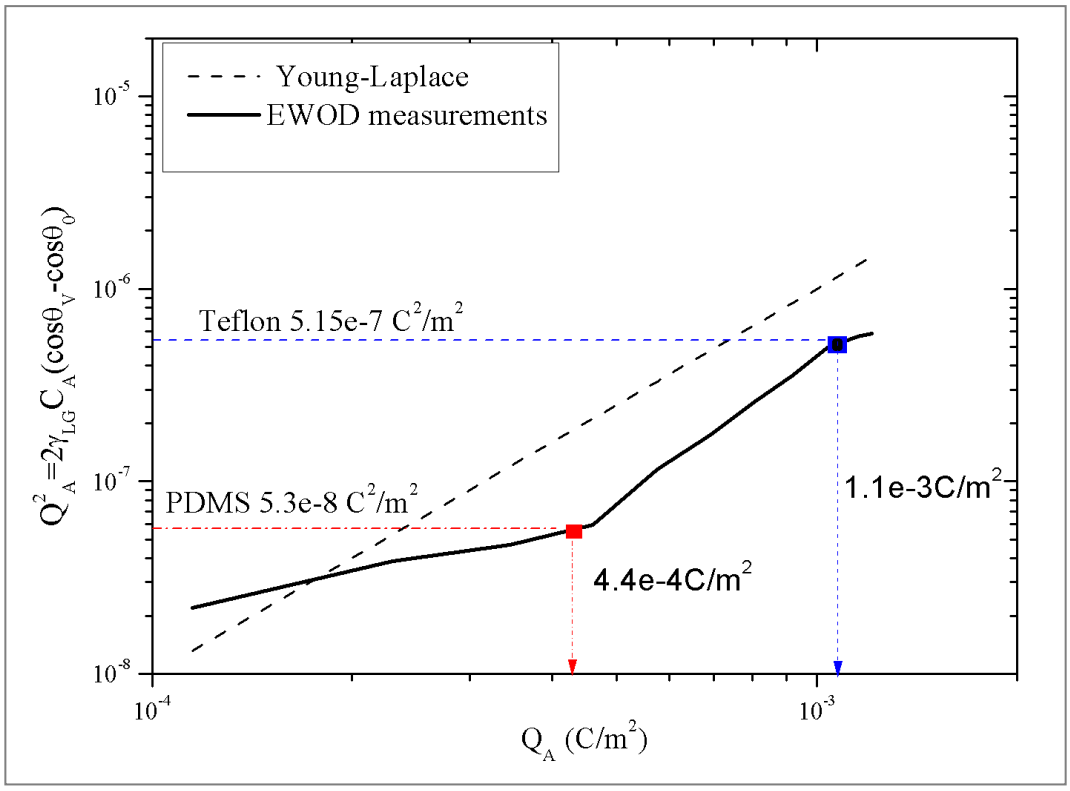

Figure 3-8: *Plot of $Q_A^2=2\gamma_{LG}C_A(\cos\vartheta_V-\cos\vartheta_0)$ for Young-Lippmann equation, conventional EWOD (solid line) and for the contactless EWOD measurements on PDMS and Teflon.*

3.5 Simulation of force and charge density in the edge of a drop for conventional electrowetting

In this section are reported the COMSOL simulation studies performed by modeling a simple electrowetting system based on a conductive liquid drop sit on a planar surface. The electrostatic force acting on the edge of the drop has been evaluated by integrating Maxwell Stress Tensor, considering surface and point charge distribution and by varying the value of contact angle ϑ. The results of the simulations are then compared with the analytical solutions and results proposed by Kang et al.[21] and by Vallet et al. [8].

The geometry showed in Figure 3-9, where the upper triangle represents the water drop with infinite wedge sit on the surface, the dielectric surface is represented by a rectangle of thickness *t*, also infinite, which is also considered in references[21] and [8] to analytically calculate the charge distribution on the drop surface when a voltage *V* is applied between the drop and the bottom electrode.

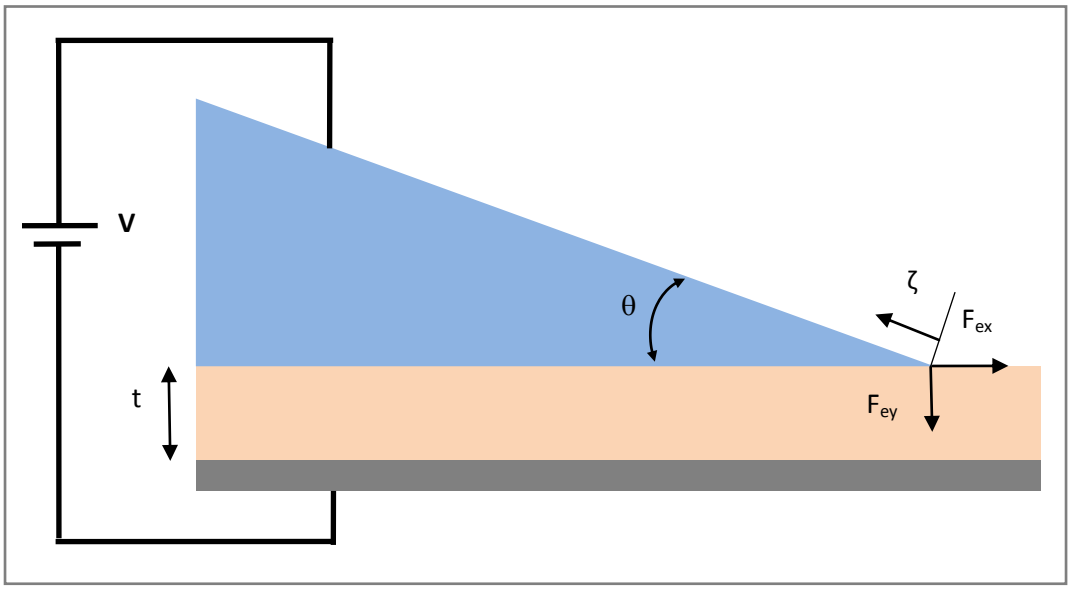

***Figure 3-9**: Cross section of the solid-gas-liquid interface used for the Comsol simulations*

The analytic solution is found by applying the Schwarz-Christoffel conformal mapping [52].

This solution provided physical insight in the underlying physics of electrowetting; in particular it was shown that the charge was accumulating at the edge of the drop and that the horizontal force was independent on the contact angle.

In references[21] and [8] two main assumptions are made: the drop is considered electrically conductor and the dielectric layer has the same permittivity of the air.

Electric field and charge distribution can be calculated solving Maxwell equations analytically; unfortunately, this possibility is restricted only to few electrode shapes; the shape depicted in Figure 3-9 is not among them, nevertheless it is possible for the case of two parallel infinite electrodes and Schwarz-Christoffel transformations allow the transformation to such particular shape.

Eq.3-5 was used by Vallet et al.[8] in order to solve analytically the electrowetting problem a shown in the following equation:

$$Z(w) = \int_{i\pi}^{w} (e^{w'} + 1)^{\alpha} dw' + i\pi \qquad (3\text{-}5)$$

In the transformed coordinates plane *W(u,iv) u* and *v* are scaled by $\frac{t}{\pi}$ and $\frac{V}{\pi}$, being *t* the dielectric thickness and *V* the voltage applied respectively. The parameter $\alpha = \frac{p}{q}$, where p and q are positive integers, relates with the contact angle as $\alpha = 1 - \frac{\vartheta}{\pi}$.

The distance from the triple point (ζ) becomes, from eq. (3-5)

$$\frac{d\zeta}{du} = \frac{t}{\pi}\left|e^{u} - 1\right|^{\alpha} \qquad (3\text{-}6)$$

Therefore the distance ζ can be calculated by:

$$\zeta = \frac{t}{\pi}\int_{0}^{u}\left|e^{u} - 1\right|^{\alpha} du' \qquad (3\text{-}7)$$

Also from eq. (3.5), the charge density on the surface of the drop can be written as:

$$\frac{\sigma}{\sigma_0} = \frac{1}{\left|\left(e^{w} + 1\right)^{\alpha}\right|} \qquad (3\text{-}8)$$

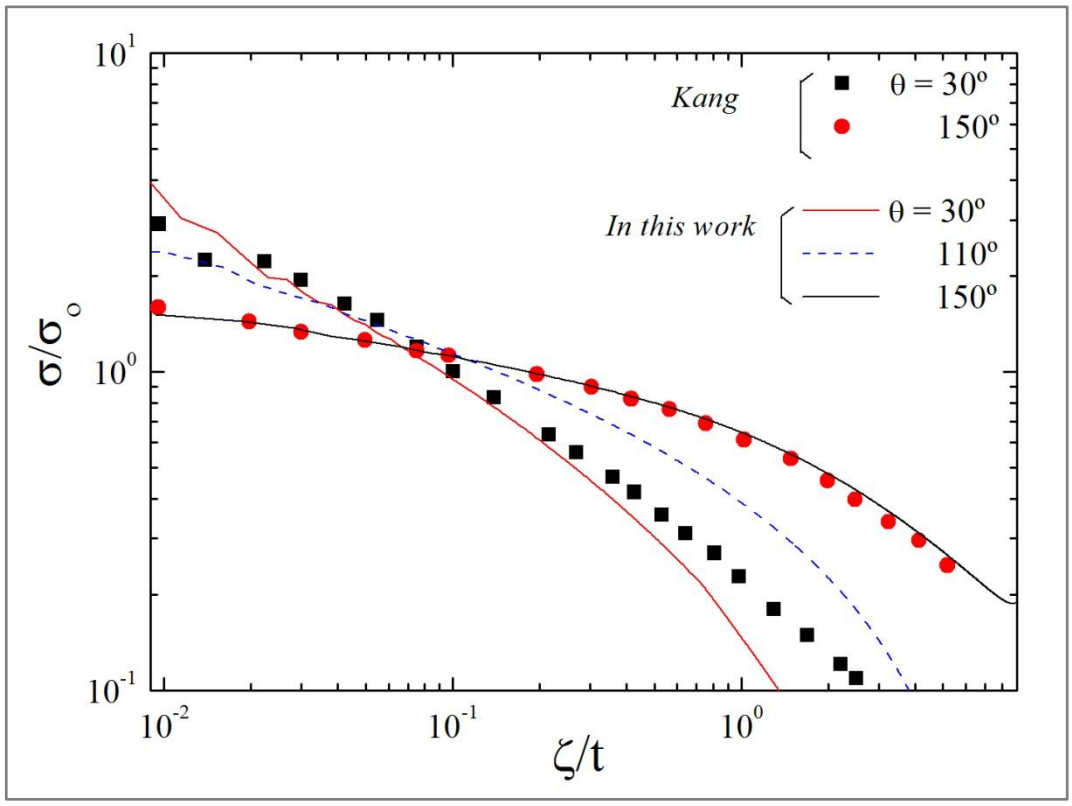

Figure 3-10: *Plot of the normalized surface charge density values simulated by Comsol multiphysics along the normalized distance from the triple point.*

The graph is normalized to $\sigma_0 = \frac{\varepsilon_0 \varepsilon_r}{t} V$ and it is plotted in function of the distance ζ from the triple point normalized by t, the dielectric thickness. Figure 3-10 shows the simulation results performed using Comsol of the normalized surface charge distribution along the normalized distance from the triple point for several values of ϑ, namely 30°, 110° and 150° in comparison with the results reported by Kang et al. in [21].

The extra 110° value is taken into account because is the baseline of the contactless and conventional electrowetting experiments performed. The results agree well with the analytical solutions, especially in the case of ϑ=150° and ϑ=30° when $\frac{\zeta}{t} < 0.2$; in the case of $\frac{\zeta}{t} > 0.2$ the matching it is poorer nevertheless the trend is not altered.

The same Comsol code allows the computation of the electrostatic force components acting upon the drop edge by integration of the Maxwell tensor.

This is shown in Figure 3-11 where simulation results are again compared to the analytical results reported in Kang et al. [21]. Analytical predictions say that horizontal component

of the electrical force is independent from the contact angle, whereas the vertical component is proportional to the cotangent of the contact angle, $\cot\vartheta$.

Figure 3-11 shows the plot of the two components of the electrostatic force. The points represent the values taken from the work published by Kang et al.[21], the lines are the results of the Comsol simulations. Simulations tend to confirm the analytic results, anyway it can be observed that the analytical solution tend to overestimate the force value and that there is effectively some dependence of the x-component of the force with the contact angle.

Figure 3-10 and Figure 3-11 confirm that the numerical simulations provide consistent results and that they can be taken in confidence, and open the way to release some of the basic assumptions made by Vallet et al.[8] and by Kang et al.[21] to consider more realistic geometries and material properties.

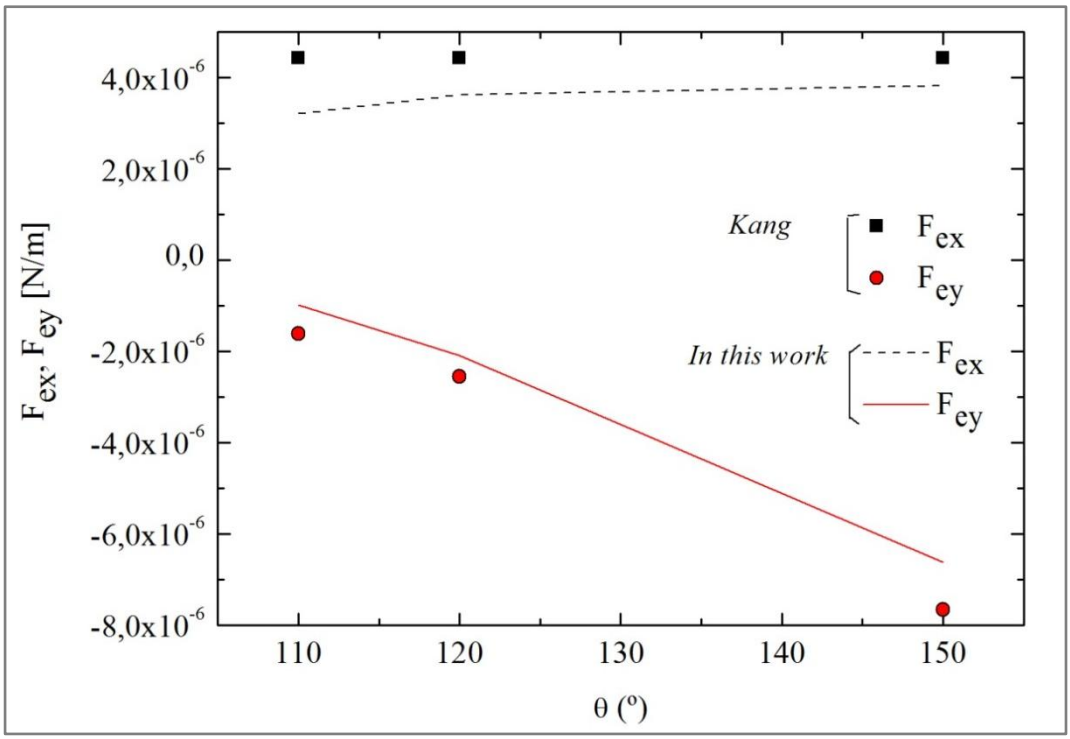

Figure 3-11: *Horizontal and vertical components of the electrostatic force on the drop edge, after applying an external voltage of 1V, as a function of the contact angle. Points are taken from Kang et al. [21].*

3.6 Simulation of force and charge density in the edge of a drop for electrowetting driven by air ionization

As described in the previous Section, the stored charge at the interface is the main parameter conditioning the contact angle variation. In this section it is examined how the contact angle would change, following the air ionization in the vicinity of the drop.

In the case the drop is an ideal conductor, the Gauss theorem states that the electric field inside the drop is zero and that the surface is equipotential. If the drop is a perfect dielectric, without conduction losses, the surface potential will be, in general, a function of the ζ coordinate, $\phi(\zeta)$. In the case of dielectric surface and dielectric drop, the distribution of charge over the drop surface and over the dielectric surface depends on the adsorption properties and nature of both.

The air ionization method is not yet completely understood and modeled in order to estimate the spatial distribution of the charge over the surface and how long it will stay before vanishing; however Comsol software allows extending the simulations to the case where the drop is not conductive, instead it shows a dielectric nature. The assumption of equipotential surface is no longer valid in this case; therefore hypothesis the surface charge distribution can be done. In particular, two limiting assumptions can be done: (a) the charge accumulates along the TPL at the edge of the drop, and (b) the charge is homogeneously distributed over the surface.

In particular, the first assumption is corroborated by data reported again by Vallet et al. [8] where accumulation of charge at the drop edge has been observed by fluorescence by applying high voltage directly to the drop and by Di Virgilio et al.[9], ionizing air above the liquid drop using a corona ionizer and a high sensitivity camera.

Figure 3-12 shows the simulation results for the two assumptions made above: (a) singular point charge of value Q placed at the triple line and (b) uniform surface charge density, σ_s.

As it can be seen, the surface potential peaks at the leftmost of the plot, corresponding to the edge of the drop for case (a) whereas it peaks far from the edge in the case (b). It is interesting to see that the surface potential gets smaller at the triple line when it is

considered a uniform charge density at the surface. This result is consistent with the fact that the capacitance per unit area increases as it gets close to the triple line (as the effective thickness of the capacitance is getting smaller), and hence the voltage has to be smaller in order to keep constant the surface charge density; in contrast, in the scenario of a point charge Q located at the triple line, the potential is maximum there.

It can be concluded that the conductive or dielectric properties of the drop dramatically change the distribution of the surface charge (in conducting drops) or the distribution of the surface potential (in dielectric drops).

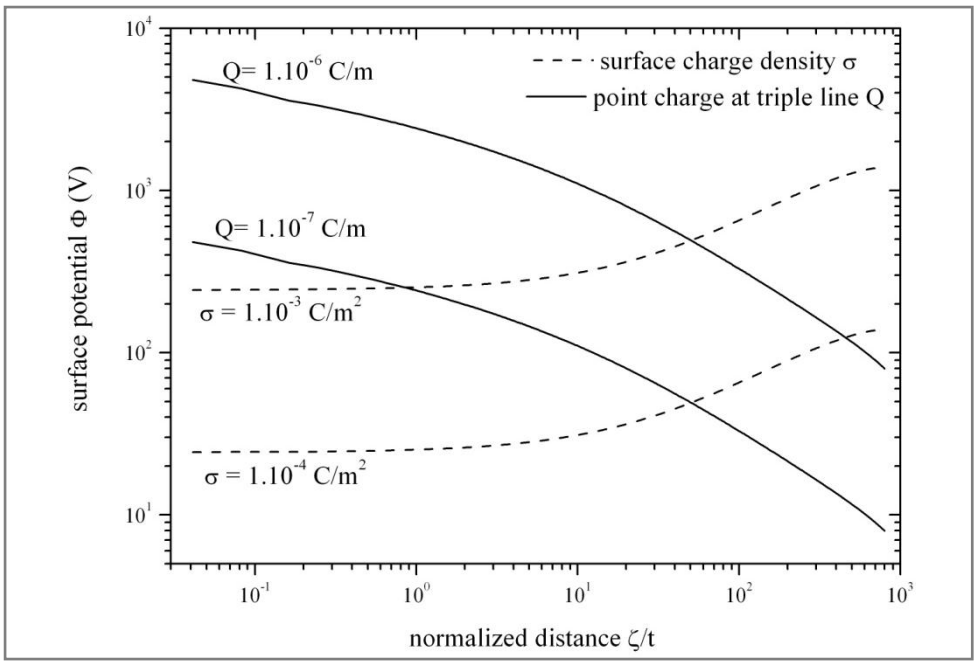

Figure 3-12: *Comparison of the surface potential distribution in a dielectric drop following scenarios of point charge at the edge of the drop (Q) and a constant surface charge density (σ).*

3.7 Conclusions

Localized ionization of air around a liquid drop sitting on a hydrophobic dielectric surface has showed to induce contact angle variation on two different coatings: Teflon and PDMS. Both coatings show a peculiar effect: on Teflon, the contact angle variation lasts only few seconds, on the other hand, the liquid drop results propelled at high velocity. On PDMS coating, the effects lasts longer; in fact the effect seems to be bi-stable and it depends on the polarity of the ions. When a negative shot is applied, the contact angle drops down and when the ion-gun shot finishes, the contact angle does not recover; in order to fully recover, it needs an extra positive ions shot.

These observations have been put in relationship with the conventional electrowetting, by comparing them plotting the Q_A^2 magnitude as a function of the $Q_{a.}$ in order to get an idea of the equivalent polarization voltages. The method does not induce the dielectric breakdown; therefore very high voltages are seen.

Furthermore, the system has been related to the electromechanical model of electrowetting proposed by Kang et al. [21] and with the work published by Vallet[8]. Comsol simulations have been extensively used for performing a set of simulations that brings to similar results as the ones analytically found by Kang. Specifically, it seems that the results of the contactless electrowetting technique can be explained by a similar model explaining conventional electrowetting. That maybe indicates that the ion shot charges are distributed over the surface of the drop and of the device similarly, also taking into account that the simulations remove some restrictive assumptions (infinite wedge drop) made in order to solve successfully the analytical model used by Vallet and by Kang. It is then anticipated that the charge create by the ion-gun shot tends to accumulate at the edge of the drop. The contactless technique produces, though, the same effect than a wire in touch with the liquid. The electrostatic force stretching by the TPL builds similarly and the contact angle varies in agreement to that.

Furthermore, the numerical code, used for the simulations, opens the path to simulations of drops of dielectric materials (i.e. pure water). It has been reported that in such case, the surface potential would change along the surface according to the hypothesis made on the surface charge distribution and that the contact angle modulation would be more noticeable in the case of a conducting drop.

Chapter 4: "*Corona*" ionization-driven electrowetting.

In electricity, a corona discharge is an electrical discharge brought on by the ionization of a fluid or gas surrounding a conductor that is electrically charged.

In this chapter it is presented how electrowetting on dielectric effect can obtain by corona ionization, a method that avoids any contact between the polarization electrode and the liquid sample. Contactless electrowetting on dielectric technology is enabled.

4.1 Introduction

Chapter 3 introduced first evidences of electrowetting driver by accumulation of charges at the TPL; those charges are likely originated by contacting and polarizing the liquid directly or by spreading a certain amount of charges around the drop.

In Chapter 3, simulations and experiments have been performed to conclude that the charges, originated by a source in the vicinity of the liquid drop, tend to accumulate to the TPL. Those assumptions have been cross-checked with some previous works which theoretical conclusions are in good agreement with the simulation and experimental results.

Nevertheless, the source of the charge detailed in Chapter 3, was not constant and reliable.

In the present Chapter more extended and systematic measurements are presented, where the charging conditions at the TPL are provided by using a setup based on a "corona" ionizer.

Corona ionizers are based on the ionization of molecules of the surrounding air by the application of a sufficiently high potential between specific geometry electrodes (e.g., pin to plane) creating a large electric field gradient [53]. The control of static charge on insulating materials is a widespread use of this technique in the semiconductor industry to avoid undesired electrostatic discharge (ESD). In fact, this is the only practical way to neutralize static charge because grounding has no effect on the level of charge in insulators.

Here it is reported on several observations monitoring the contact angle change after the corona has been switched on, photoluminescence pictures of the drop and the surrounding area, and surface charge measurements.

Also, it is shown that air ionization has an important effect on the contact angle change, increasing the wettability of the surface. The results of these experiments have been then compared to the results of conventional electrowetting, leading to the conclusion that in

the range of experimental voltages explored, the contact angle lies in the saturation regime.

A reversible effect is also discussed, when contact electrowetting is performed over a PDMS surface.

XPS measurements have been performed before and after corona exposure to make sure that the observations are not related to the deterioration of the PDMS.

Finally, in an effort to contribute to an understanding of contact angle saturation and because the only source of charge involved in the experiments is the ionization of air, the saturation angle value has been measured in function of the air relative humidity.

An interesting relationship between saturation contact angle and humidity is found: the saturation contact angle increases as the RH is increased.

4.2 Fundamentals of the "corona" effect

"Corona" discharge is a phenomenon that occurs at ambient temperature and pressure when high voltage is applied to a pair of electrodes separated one to each other.

"Corona" effect is strictly related to the electrode shape and generally it shows up when the electrodes are highly asymmetric, and commonly one of them has a strong curvature with respect to the other. The most common case of "corona" effect is constituted by pin-to-plane electrodes.

There are two main types of "corona": the positive and the negative "corona" effect.

If the pin shaped electrode is connected to positive output of the voltage supply, then the system it is called "positive corona discharger", on the other hand if it is connected to the negative output of voltage supply, the system it is called "negative corona discharger". Properties of negative and positive corona discharge are very different from each other and they are explained following.

The electric potential at which "corona" happens it is called **corona threshold voltage**. Above this voltage there is a region around the tip of the electrode where the current increases with the voltage, this region is called Ohm's Law regime and ionization is confined in this region.

Positive "corona" provokes a very stable and defined Ohm's law regime region around the electrode tip, as the electrons resultant by the ionization, are attracted towards the curved electrode while positive ions are repelled. By inelastic collisions, more molecules are created in an electron avalanche. Out of the ionization region, more secondary electrons are created by the electron avalanche and the reaction is self-sustaining in air surroundings.

Negative "corona" is more complex and less stable as the electrons are repelled by the electrode tip and the amount of secondary electrons created by this kind of ionization is not sufficient for a stable and sustainable reaction, therefore in general, negative corona is not homogeneous therefore effects are less reproducible.

In the experiments described in this Chapter, positive "corona" has been used.

When the Ohm's law region regime grows until arcing and breakdown appear, it means the dielectric strength of the surrounding environment has been overcome. The dielectric strength is the maximum electric field a material can withstand before conduction. For air it is 3kV/mm and above this level, air ionizes rapidly and arcing and sparks occur. Although this value depends on humidity of air, therefore it may vary considerably, as shown later in the Chapter. With air ionizing, the main side product created is ozone, but also negative ions OH^- and positive ions H^+.

Those are responsible of the charge transportation towards the opposite electrode and in the surrounding region of the system. These carriers are responsible to bring charges from the tip of the pinner used as "corona" charger device and the charges are acting on the liquid surface modifying it and varying the contact angle of the liquid drop.

4.3 "Corona" ionizer measurement setup

"Corona" ionizers are devices based on the ionization of the air molecules by the application of a sufficiently high voltage between two electrodes. The electrode geometry plays a very central role in the creation of ion flow. Several geometries are possible to be implemented; the most common include pit-to-plane, wire-to-plane and wire-in-cylinder. Typically the geometry chosen is "pin-to-plane" as the electric field gradient created is larger [53].

Figure 4-1: *Simco-Ion Pinner for local ion charging.*

The ionizer used for the experiment has been acquired at Simco-Ion and consists in a PFTE bar having 5 pins generating ionization; the radius of the pins has been measured and it is 45μm. The ionizer is shown in Figure 4-1. The pins' are fabricated of stainless steel and current is limited by an 80MΩ resistance in series with the voltage supply in order to prevent spark over. The ionizer is connected to a HVDC power supply, provided by Ultravolt Inc. The HVDC Ultravolt system supplies a DC potential comprised between -15KV and +15KV with low ripple with a maximum power is 30W.

The general schematic of the measurement setup is shown in Figure 4-2.

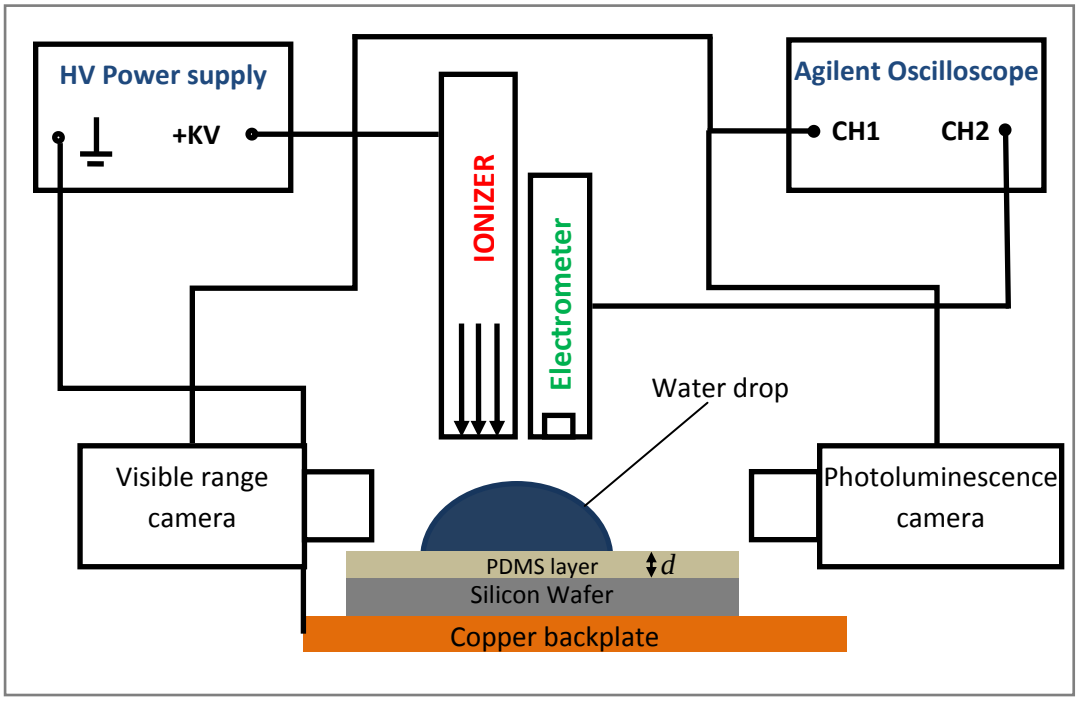

Figure 4-2: *Schematic representation of the measurement setup: the high voltage power supply polarizes the ionizer and it is connected to the oscilloscope in order to store the voltage transient. The oscilloscope also stores the electrometer analogue measurements synchronized with the power supply. The ionizer and the electrometer are placed above the droplet at a controlled fixed distance. The drop sits over a PDMS layer and it is observed with the help of two cameras, counter posed. The cameras are synchronized by a trigger signal coming from the voltage supply.*

In the moment the corona ionizer builds charges, they are measured by using a handheld electrometer distributed by Electrostatica, SA. The electrometer is small enough to be mounted together with the ionizer and close to the substrate. The height between the substrate and the ionizer/electrometer is fixed to be 1cm. The electrometer generates a TTL compliant analog signal that is acquired by using a digital oscilloscope (Agilent DSO1102B).

The optical acquisition is made by using two different systems: a contact angle goniometer CAM200 and a high sensitivity camera ImagEM, provided by Hamamatsu. The camera is cooled at -65ºC in order to reduce the thermal noise, and it is equipped with a telecentric optic 1X. This camera is then capable to acquire photoluminescence.

The substrate structure used for the tests is based on a bare silicon wafer covered with a thin layer of PDMS. The silicon wafers have been accurately cleaned in two steps:

- Piranha cleaning

- HF dipping.

The piranha cleaning is aimed to eliminate all possible organic impurities present on the wafer. The piranha solution is obtained by mixing concentrated sulfuric acid to 30% hydrogen peroxide. When the mixture is ready, the silicon wafers are submerged for 40minutes, until the temperature decreases to approximately 40ºC.

The wafers are then rinsed with deionized water and dipped in HF 2% for 10 minutes. This last step eliminates the native oxide present on the silicon surface.

Previously, a PDMS batch was prepared using the polymer kit Sylgard 184. Each 4inches wafer needs approximately 5ml of silicon oil mix in order to be completely and homogeneously covered. The mix has been done by setting a 10:1 ratio between silicone oil and curing agent. Hereafter is reported the preparation steps:

- Measure 4.5 ml of silicon oil and pour them in a plastic container with sufficient capability (300ml)
- Measure 0.5ml of curing agent and mix it gently with the silicon oil until complete homogeneity has been reached.
- Place the container in a vacuum chamber.
- Build vacuum until the bubbles form and then break the vacuum to atmospheric pressure.
- Repeat this process until no bubbles can be seen in the mixture.

In order to have three different PDMS thicknesses, the wafers have been coated at different spinning speeds using different recipes: after an acceleration step of 30s at 500rpm, the PDMS has been spun at 500rpm/1000rpm/1500rpm for 65s. The resulting thicknesses obtained are 69.5μm, 53μm and 44μm. Once the PDMS was spun, the wafers have been cured on a hot plate at 70ºC for 30 minutes. After this curing step, the PDMS polymer is completely cross-linked and it is ready to be used. The contact angle shown by the PDMS towards water in air is above 100º.

4.4 Measurements results

In this section are reported the measurements results obtained using the measurement setup shown in Figure 4-2.

The measurements have been performed in air using deionized water. The droplets were dispensed in a controlled way using a micropipette, selecting a size of 20μl. For each measurement a new water droplet was placed under the corona ionizer at a controlled distance of 1cm.

Once the device was placed beneath the ionizer head and the liquid was correctly dispensed and centered with respect to the ionizer head, the HVDC voltage supply was triggered on; therefore high voltage was applied to the ionizer and the oscilloscope measure was taken.

As reported in Section 4.1, no major changes in contact angle variation were reported for the voltage source set below 4kV; corresponding to the breakdown voltage of air[54], that also has been reported as a function of humidity[55]; the *corona* discharge usually appears before brush discharge or spark-over as soon as the electric field reaches the critical value derived by applying the Peek breakdown criterion for a pin-to-plane geometry[56].

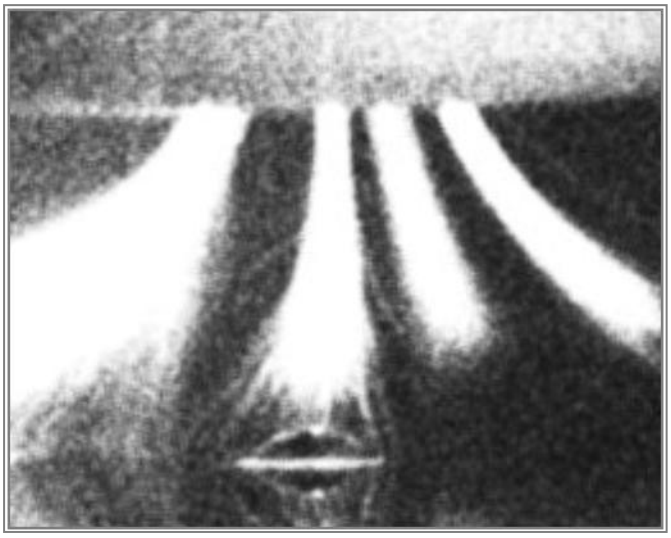

***Figure 4-3**: The picture shows the air breakdown luminescence of the corona ionizer. The luminescence starts from the five needles of the ionizer and can be also appreciated around the drop perimeter. This fact is evidence of electrical charge accumulation along the TPL.*

Applying the Peek criterion, the inception voltage calculated for the geometry used is found to be 2.5kV thus the applied voltage has to be increased beyond this threshold in order to appreciate any contact angle variation.

Photoluminescence observations have been performed using a high sensitivity camera Hamamatsu ImagEM. In Figure 4-3 is reported the air breakdown luminescence picture: bright streams of ions originated from the needles of the ionizer appear and going to the drop and the surrounding area. While the voltage was still applied, luminescence was observed along the perimeter of the droplet; this observation is evidence that charges accumulated at the TPL where they recombine emitting photons.

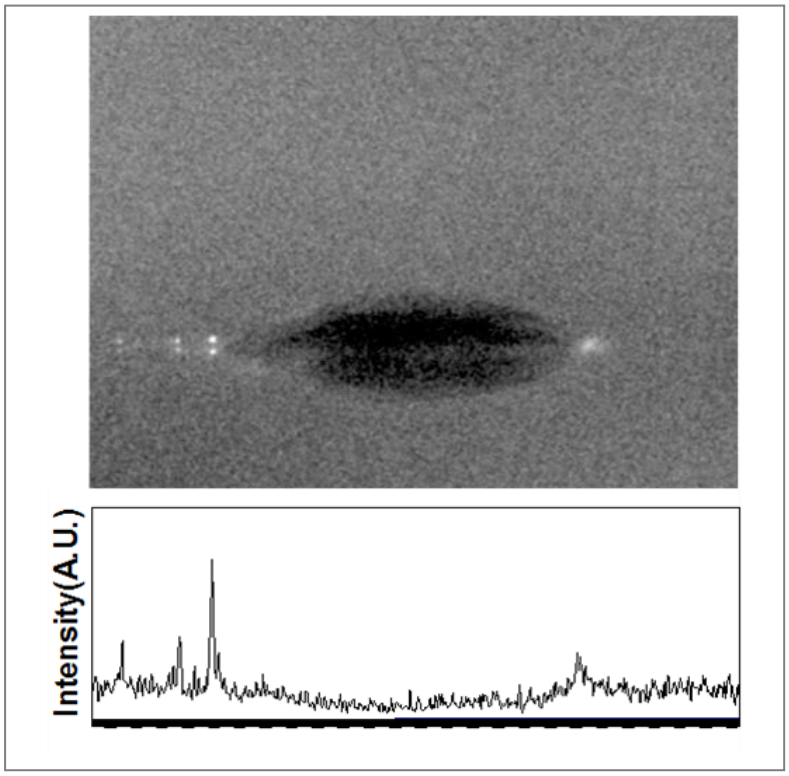

Figure 4-4: *Luminescence observed with no high voltage applied to the ionizer. The intensity graph, in arbitrary unit, shows the luminescence effect at the TPL.*

Figure 4-4 shows the residual luminescence still observed when high voltage source is switched off. Few sparks originated along the TPL with no voltage applied, as reported by the luminescence intensity graph reported beneath the picture.

The luminescence effect was accompanied with a significant contact angle reduction. Besides the high sensitivity camera, a measurement camera has been used for the contact angle measurement. The starting contact angle was around 110˚, the contact angle after

ionization was comprised between 70˚ and 55˚, as in the case shown in Figure 4-5, thereby confirming the wettability increases.

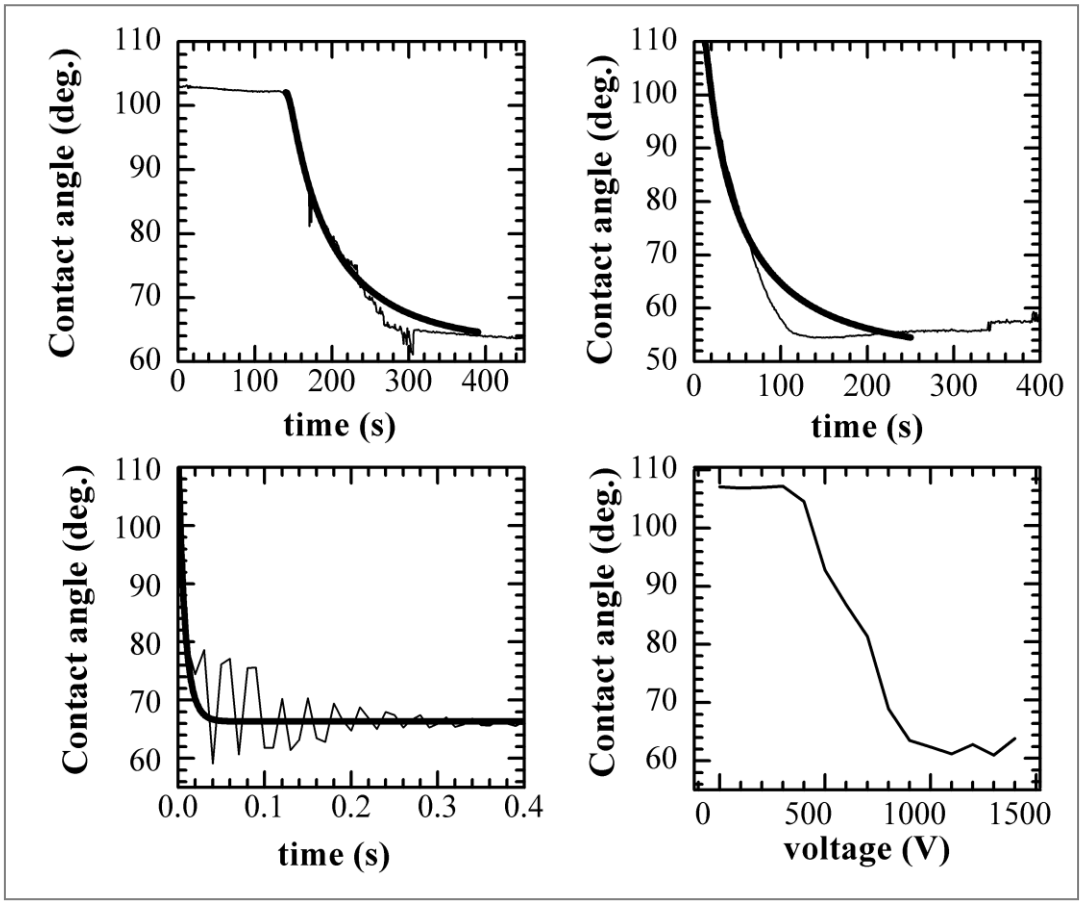

Figure 4-5: *Contact angle measured in function of time for several values of the corona ionizer polarizing voltage. 4kV (upper left), 4.5kV (upper right), 8kV (bottom left) and conventional electrowetting (bottom left). All devices were coated with 69.5μm PDMS with exception of the 8kV measurement where a 53μm PDMS layer was used. The thick lines (upper left, upper right and bottom left) are fitting results from the analytical model proposed by Castañer and Di Virgilio [62]. The measurements were performed with temperature conditions comprised between 20.2˚C and 21.4˚C and relative humidity around 27%-28%.*

These observations agree with observations reported by Peek in [56] confirming the charge accumulation over the edge of the drop as was predicted by calculations using Schwartz-Christoffel transformations[52]. Moreover, it is confirmed that air ionization acts similarly as the direct application of voltage to the liquid droplet.

Figure 4-5 resumes the contact angle measurements as a function of time. Those measurements were performed using a high speed camera Basler A601f, place opposed with respect to the high sensitivity camera as shown in Figure 4-2 and set at 400fps by reducing the viewing area to 100x400pixels. The measurements were performed by

setting the polarizing voltage of the corona ionizer at several values; the measurements are then compared with the bottom right graph in Figure 4-5 where are plotted the values of conventional electrowetting measurements.

The conclusions taken out of the plots shown in Figure 4-5 are multiple. Firstly, the transient becomes faster with the voltage increase, as can be clearly seen comparing the top left and bottom left plot. If the ionizer is biased at 4kV, the transient lasts approximately 150s, before the variation in contact angle could be appreciated. This effect could be due to the threshold described by Quinn in ref.[10].

Moreover, it is noticed that higher values of source voltage produce transients having smaller asymptotic values in the contact angle; although these values are very close to each other, being between 56˚ and 64˚. The comparison of these results with the conventional electrowetting measurements plotted in Figure 4-5 bottom left indicates that the saturation regime is reached.

Finally, from the plot at bottom left of Figure 4-5, damped oscillations are observed, mainly at higher voltages. Oscillations are consistent with resonance modes, as Oh et al. predict in ref.[57, 58, 59]; resonance frequency is in fact expected to be around 20Hz for the lower resonance mode, although the model apparently underestimates the observations: the resonance frequencies observed are found typically in the range of 30Hz.

The modeling of the movement of the fluid leads to a free boundary problem between the droplet and the surrounding air or fluid, which has been studied using different approaches for different geometries. The movement of a drop on a surface has been dynamically modeled with the help of the phase-field model[60]; a finite element model method for electrowetting devices between two parallel plates has been proposed[61, 62] and a shape-inverse approach calculates the curvature[63]. All these models require a CFD tools to be implemented.

More simplifying approaches are proposed by Castañer and Di Virgilio in ref. [64], neglecting inertia, gravitational effects and viscous losses or assuming quasi-static conditions for constant triple-line velocity, as also considered by Blake[65], Berge[3] and Vallet[8, 66].

Spontaneous wetting models, the conventional molecular-kinetic (MK) proposed by Blake[67] model and hydrodynamic model proposed by Voinov[68], can be successfully applied for the recovery modeling after excitation[69] although it is not possible for the transient induced by the electrowetting. Hereafter it is proposed a suitable model for the contact angle variation transient induced by electrowetting.

In Figure 4-5, are shown experimental measurements with superimposed fittings obtained applying the model described in ref.[64]. The model proposed is a lumped model coupling a Thevenin equivalent circuit of the source (V_{th} is the equivalent source voltage and R_{th} is the equivalent resistance) with the simplified differential equations of the dynamic surface tension balance.

It must be remarked that V_{th} and R_{th} model-equivalent circuits of the corona charging setup shown in Figure 4-2, and hence those two lumped parameters also include practical distributed effects.

In the examples shown in Figure 4-5, the value of R_{th} had to be adjusted to very large values, namely, $4x10^{12}\Omega$ for the 4 kV experiment and $5x10^{12}\ \Omega$ for the 4.5 kV experiment whereas for a larger voltage, 8 kV, the key parameter for the fitting was the friction coefficient, which was set to 0.5 Ns/m^2, and the value of R_{th} was irrelevant for $R_{th} < 500\ \Omega$. These results are interpreted from the fact that at higher voltages the supply of charge to the triple line is sufficiently fast that the transient speed is limited only by friction.

At low voltages, however, the transient is limited by the charge supply rate, indicating that the ionization is limited as described in by Intra et al. [70], and hence can be defined a "current-starved" charging supply regime. It also has to be mentioned that the model described in ref. [64] did not include saturation effects. The values adjusted from the model for V_{th} provide effective values only for the charge per unit area, q_{Amod}, defined as follows:

$$q_{A\mathrm{mod}} = \frac{\varepsilon_o \varepsilon_r}{d} V_{th} \qquad (4\text{-}1)$$

In the experiments the values provided by eq.(4-1) are generally smaller than the measured values of q_{Ameas}, given by:

$$q_{Ameas} = \frac{\varepsilon_o \varepsilon_r}{d} V_{meas} \qquad (4\text{-}2)$$

where V_{meas} is the measure of the electrometer. This indicates that we are in the saturation regime. To confirm this assertion further, we have performed conventional electrowetting with a contact needle in the drop and measure the contact angle as a function of the applied *DC* voltage. This is shown in Figure 4-5 (bottom right), where the saturation angle lays around 65˚.

In Figure 4-6 is reported a plot of $(\cos\vartheta_V - \cos\vartheta_0)$ as a function of the charge per unit area, q_A, measured by the electrometer for the 53µm-thick PDMS samples.

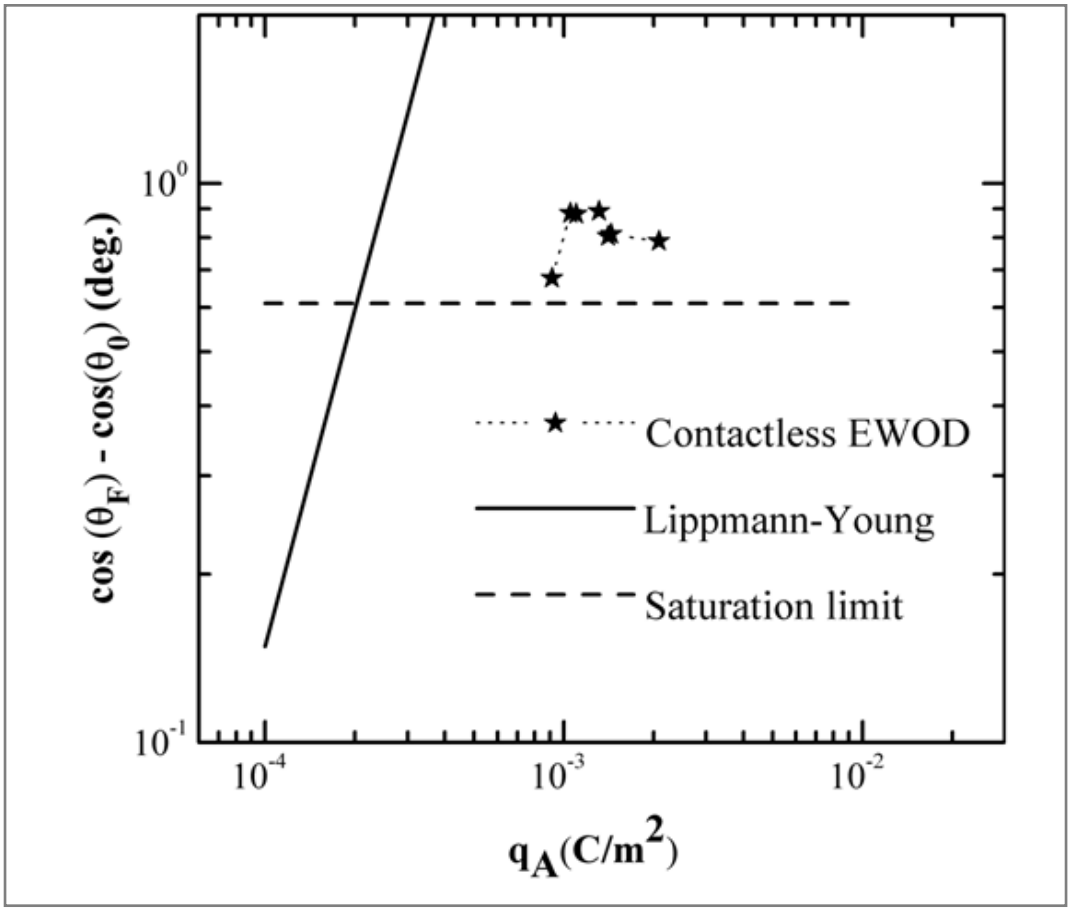

Figure 4-6: *Plot of the values of (cos ϑ_v - cos ϑ_0) as a function of the measured values of the charge per unit area, q_A. Lippmann_Young equation (──), Quinn [10] saturation limit (---), d = 53 µm, ε_r = 2.62, γ_{LV} =72.9 x10^3 ,N/m and γ_{SV} = 19x10^3 N/m.*

Over the measurement graph are also superimposed he theoretical plot of the Lippmann-Young (——), eq.(1-4), in a log-log plot. Moreover, we have also drawn a horizontal line (-----) corresponding to the value given by eq. 4-3:

$$\cos \vartheta_{SAT} = \frac{\gamma_{SV}}{\gamma_{LV}} \qquad (4\text{-}3)$$

which is the contact angle saturation limit predicted by Quinn et al. [10], by stating that the solid-liquid surface tension minimum value is zero. By applying eq.(4-3) to the contactless case, the saturation contact angle is ϑ_{SAT} = 74.6˚; by calculating $(\cos\vartheta_V - \cos\vartheta_0)$, it is found the value represented in Figure 4-6 by a horizontal line. All data points in this graph above the horizontal line are beyond the saturation limit predicted by eq.(4-3).

From the observations, as shown in the results in Figure 4-6, the saturation values that have been measured fall beyond the predictions of eq.(4-3).

4.5 The effects of humidity on contact angle saturation

In the previous Section have been discussed the results of the contactless electrowetting experiments and one of the main conclusions is that the saturation regime for the contact angle has been reached and the contact angle saturation value is smaller than the limit predicted by Quinn et al.[10]

This result is consistent with the comparison made in Table 1 in ref. [10] of the result of eq.(4-3) with several published experimental results; the agreement was within 13˚. (See, for example, the results cited in ref. [71])

The conclusion is that apparently eq.(4-3) overestimates the contact angle saturation value. It was also discussed in ref. [10] that the interpretation given in Vallet et al.[8] attributing saturation to air ionization was more concurrent that a limiting effect. Recently, additional light has been shed on the saturation effect in liquid-vapor-solid[72] and in liquid-liquid-solid [69, 73] attributing the saturation to trapped charge [74].

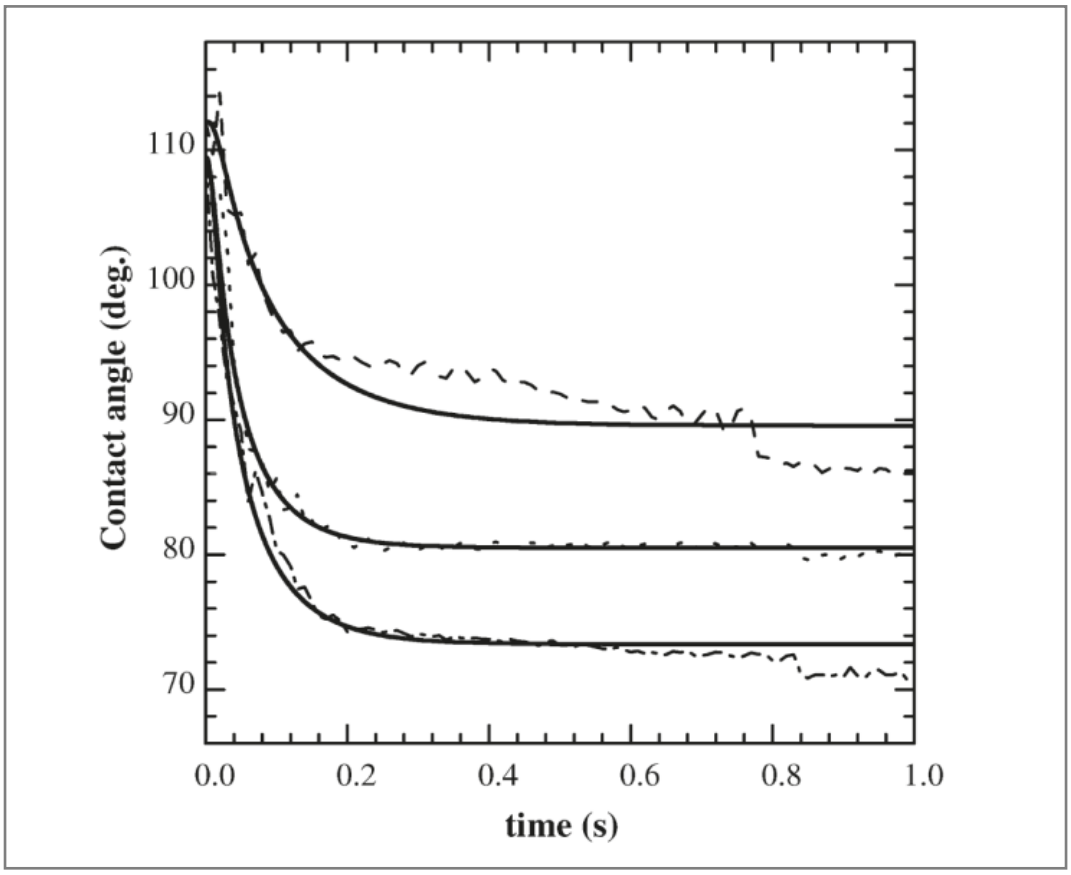

Figure 4-7: *plots of contact angle as a function of time for a 7.5kV source voltage, 69.5μm thick PDMS samples and several values of relative humidity (RH): 46% (—), 60% (···) and 70% (– · –). Solid lines are model fittings. Experiments were performed at a temperature comprised between 24.4˚C and 25.2˚C.*

Performing contactless electrowetting, the only source of charges involved is air ionization; as it is observed that the wettability increases after ionizing air, the question of whether the air humidity could any effect on contact angle saturation value arises.

For this purpose, the setup was modified in order to perform contactless electrowetting in a sealed transparent plastic box. The air relative humidity (RH) inside the plastic box could be controlled and monitored continuously in order to make sure the experiments were run in steady RH conditions during the contact angle dynamics observations.

In Figure 4-7 are shown results of measurements depending on relative humidity. As can be seen in the main Figure, the contact angle saturates at larger values as the relative humidity increases. It can also be observed that the transient is also slowed down as the RH increases. The change in ϑ_{SAT} is quite significant because a change in RH from 46% to 70% produces a change in ϑ_{SAT} from 72˚ to 86˚.

It is difficult to attribute only to eq. 50 these changes in the saturation angle because this would require either a smaller value of γ_{SV} or a larger value of γ_{LV} or both simultaneously as the humidity increases. No evidence has been found of such behavior for the surface tensions of PDMS and water in presence of air and variable RH.

Taking into account that the Peek critical field for the breakdown of air increases with humidity and that the corona inception voltage gradient also increases with humidity for a positive corona[75] the interpretation of the results is that the efficiency of charge transport from the corona area to the interface decreases as the humidity increases, possibly because of the increase in the inception voltage gradient and also the increase in the electrical conductivity of air[54].

Figure 4-8 shows a summary of the main results of the humidity effects.

As can be seen, the increase in the contact angle saturation value as the relative humidity increases corresponds to a decrease in the value of model parameter V_{th}, consistent with eq.(1- 4) and eq.(4-3).

Moreover, the fall time is seen to increase from low humidity to high humidity values quite sharply as RH gets larger than some 40%, corresponding to a very significant

increase (log scale of Figure 4-8 b) in the model parameter R_{th}, thereby indicating that the two parameters are decoupled.

These results in Figure 4-8 support the interpretation that air ionization and air humidity have a significant effect on the transient dynamics of the contact angle and its saturation value

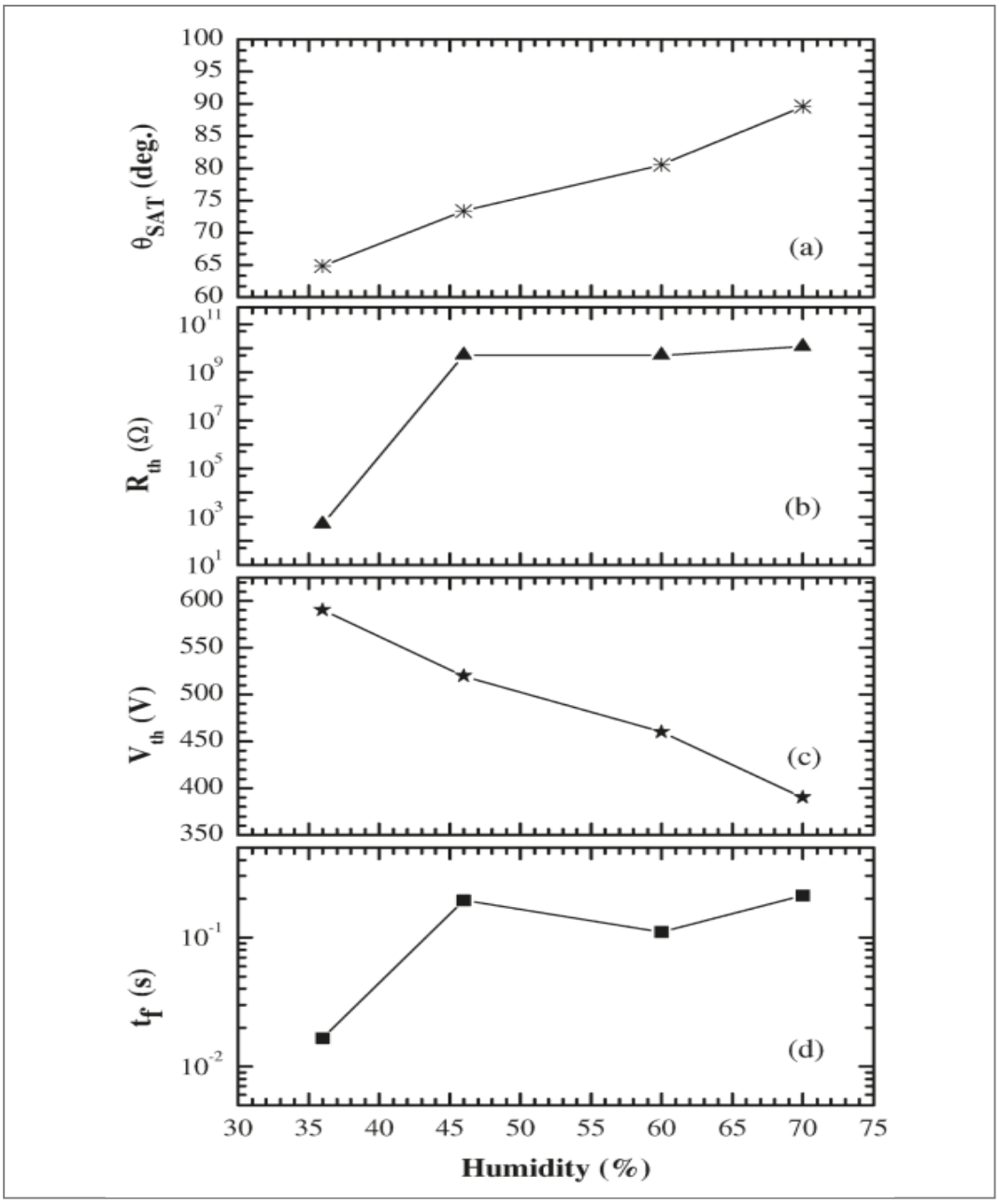

Figure 4-8: *Experimental values of the (a) saturation contact angle value ϑ_{SAT}. (b) Thevenin equivalent resistance. (c) Thevenin equivalent voltage. (d) Fall time of the contact angle transient from 90% to 10% of the maximum as a function of the relative humidity value.*

.

4.6 Reversibility

The previous section the wettability increase dynamics after corona ionization it has been discussed. This section is dedicated to the reversibility of the effect when the corona ionizer is switched off.

A summary of the observations made is the following:

a) After the drop on top of the PDMS layer has been exposed to the corona and no further manipulation of it is made, the contact angle remains low for a long time (minutes to hours).
b) If after corona exposure a micropipette is used to suck the drop out and immediately afterwards a new drop is deposited in the same place, then the contact angle recovers totally.
c) If the PDMS surface is first exposed to the corona ionizer for a few seconds with no drop on it and then switches off the corona ionizer and deposit a fresh drop on the surface, then the contact angle is low. If the drop is sucked up with a micropipette and a fresh drop is deposited in the same place, then the contact angle is fully recovered.
d) If the PDMS layer is exposed to the corona and before depositing a drop on top of it place the sample on top of a hot plate at 40˚C for a few seconds, then the contact angle that we measure after that is the same as before the corona exposure.

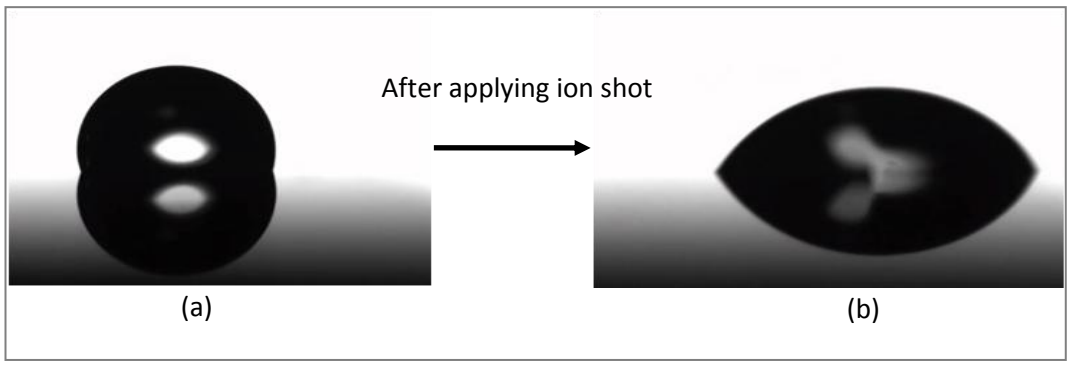

Figure 4-9: *Effect of ionization of air over the liquid drop. a) The rests over a hydrophobic dielectric surface and exhibits a contact angle of 100° approximately and b) the reduction of contact angle to levels around 70° due to the air ionization. Over PDMS the contact angle remains low for long periods of time (~minutes) and it recovers slowly.*

Before discussing these observations, it is worth reporting on the XPS measurements made on PDMS before and after corona ionization. Those measurements have been carried out in order to verify the possible deterioration of the PDMS due to the corona ionization exposure.

It has been reported in the literature that the PDMS surface becomes hydrophilic when exposed to an electrical discharge[76]. It has been described that the main effects of corona discharge on PDMS are the formation of a glassy SiO_x surface layer, an increase in the oxygen content of the surface, and the degradation of the network structure.[77] However, PDMS shows the capacity to regain its hydrophobicity after some time. It has been shown that corona exposure with a voltage of 30kV at a distance of 5mm for 1 to 30 minutes creates damage that recovers on a timescale of 100 to 1000 min[76].

The possible surface damage of PDMS samples has been investigated by XPS measurements looking into the oxygen contents using a Kratos Ultra DLD system with a non-monochromatic source (Mg KR, 1253.6 *eV*). The measurements have been made at INA (Instituto Universitario de Nanociencia de Aragón, Zaragoza, Spain).

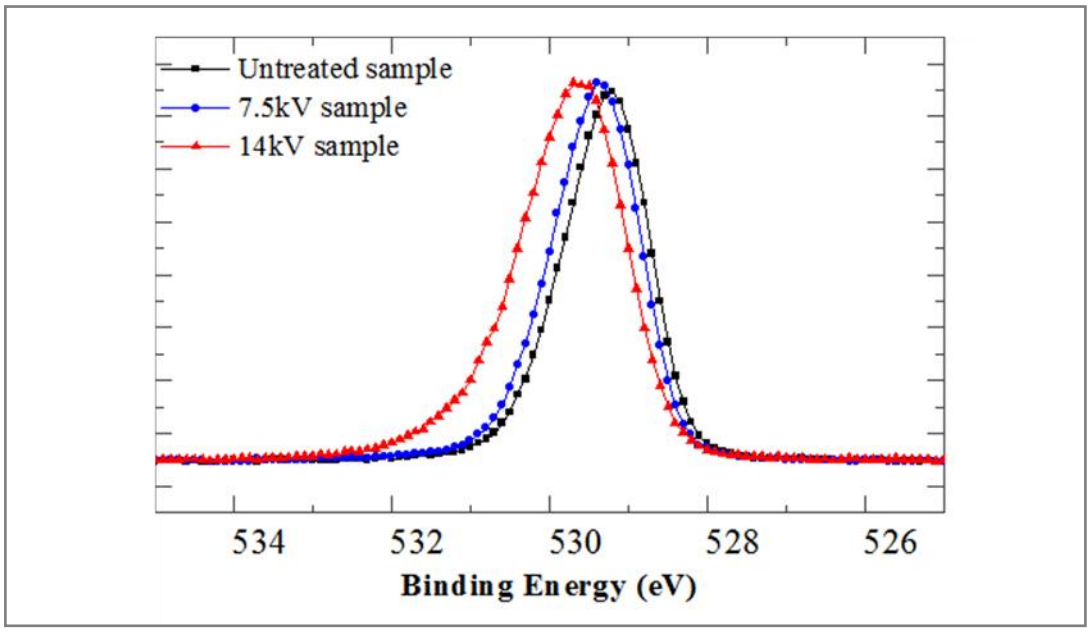

Figure 4-10: *O 1s peaks resolved for the PDMS untreated sample and for corona-treated samples at 7.5 and 14 kV. The untreated and 7.5-kVtreated samples show very similar and symmetric responses here as the sample treated at 14 kV shows a shift toward higher binding*

The pressure in the chamber was kept at around 10^{-7}Pa, the sample area is approximately 1cm^2, and the sampling depth is around 10nm. The value of the *C 1s* core of 284.5*eV* has been used for the calibration of the energy scale. Three PDMS samples have been cut from the same substrate. One of them was at 14kV and fitted with two peaks: the one at lower energy is centered at 529.5*eV* and corresponds to *O 1s* as in unoxidized PDMS, and the second at higher binding energy and centered in 530.2*eV* could be associated with the possible incorporation of silanol groups, *Si-OH*, on the surface. The conclusion is that the chemical environment changes when a PDMS sample is submitted to DC ionization on the order of 14kV whereas it does not if the DC ionization is some 7 to 8kV for a time of exposure of 180s.

Refs.[78, 76] report damages in PDMS surface created by a more aggressive electrical discharge than the one used in the experiments carried out in this research; the exposure producing damages on the PDMS structure lasted from 1 to 30 minutes, which is a much longer time than in contactless electrowetting case, which was a few seconds, and also the corona voltage was much higher (30kV compared to a maximum of 14kV).

Finally, in contactless electrowetting experiments the distance between the corona electrode and the drop was twice as long. The results shown in Figure 4-6, Figure 4-7 and Figure 4-8 for the wettability increase were for samples where the experimental conditions were such that XPS measurements did not find material deterioration.

The experiments enumerated in points (a) to (d) above are not compatible with PDMS damage recoverable on a timescale of 100 to 1000 minutes. They are, however, compatible with the effect of mobile charge. The explanation is that the charge created by the corona ionizer is stored in the capacitance created by the drop, PDMS layer, and substrate and, according to Young's law, reduces the solid-liquid surface tension and decreases the contact angle.

If the sample is kept electrically isolated, then the charge remains there for long time and the effect does not revert spontaneously. If some mean is provided for the charge to leave the sample, such as drawing away the drop using a micropipette or by just moderately heating the sample, then the contact angle recovers.

The effect of dielectric charging recovery by moderately heating the sample has been extensively used in studies of the dielectric charging of MEMS devices[50].

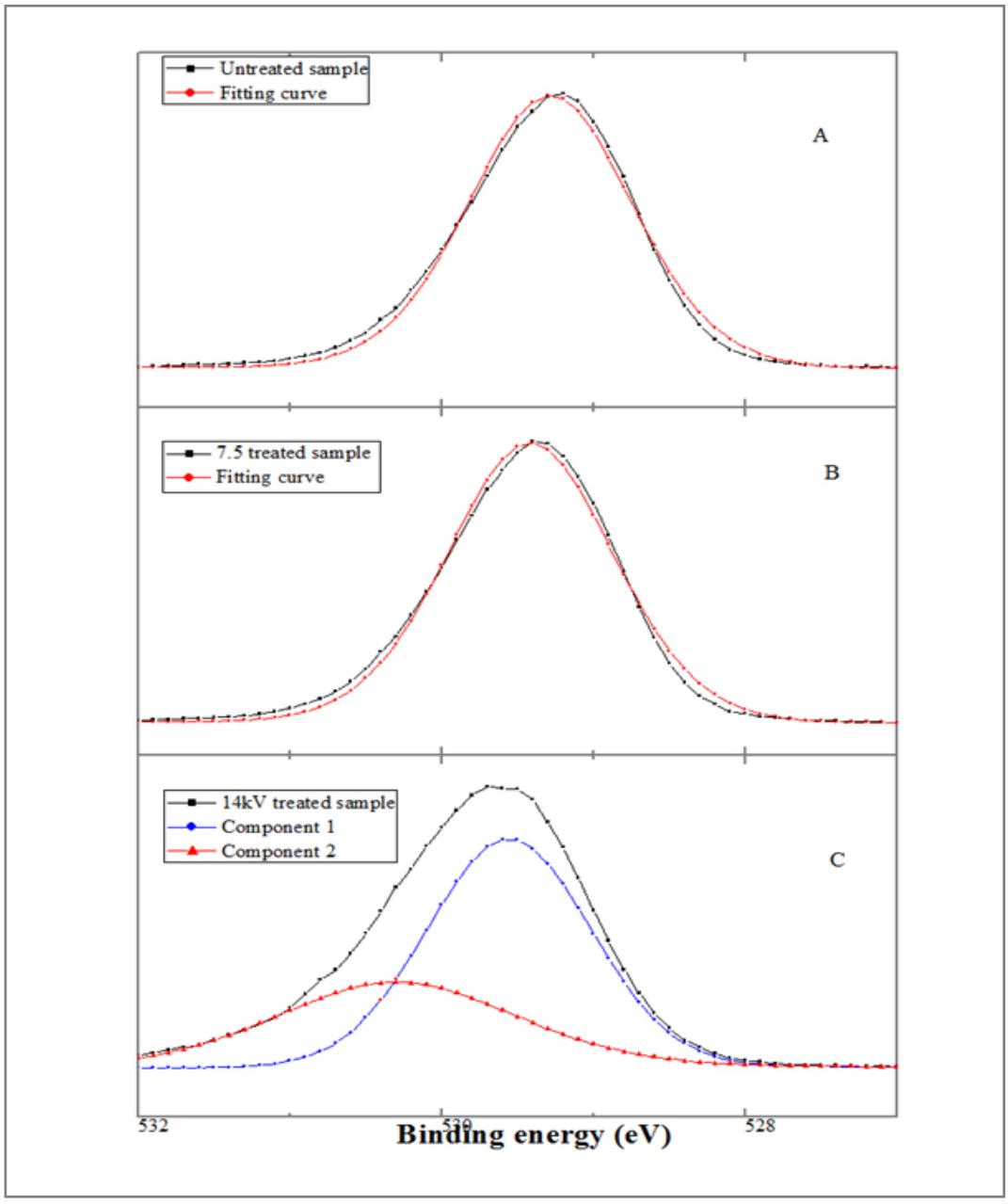

Figure 4-11: *O 1s peaks fitted for (a) the untreated sample and (b) the 7.5kV- and (c) 14-kV-treated samples. The untreated and 7.5-kVtreated samples show very similar and symmetric responses. They can both be fitted with just one peak, which surely corresponds to unoxidized PDMS. The 14 kV peak shows a small asymmetry that leads to a two component fitting: C1 at 529.5 eV and C2 at 530.2 eV. Two fitting components mean that oxygen on the surface can be found in two different compounds: unoxidized PDMS, expressed by the peak at lower energy, and partially oxidized PDMS, expressed by the higher-energy peak describing the incorporation of Si-OH groups.*

4.7 Conclusions

The effects of air ionization on the wettability of hydrophobic surfaces have been investigated by means of a corona ionization instrument and PDMS surfaces on top of a conductive substrate.

It has been shown that the wettability increases provided that the corona voltage is above a value that in our case was in the range of 4kV for our experimental setup.

Although in the vicinity of 4kV the contact angle transients were slower than at higher voltages, the asymptotic value of the contact angle was very similar in all experiments. Model fitting was used to calculate parameter values, and it was concluded that the charge supply to the triple line is the limiting effect for low-voltage values whereas at larger voltages the limiting parameter is the friction coefficient.

The conclusion is that, in all cases, the asymptotic value of the contact angle was in the saturation regime.

The effects of the humidity of the air on the value of the saturation contact angle were also investigated, and a significant increase was observed for increasing values of the relative humidity along with a slowing down of the transient. Air ionization and the humidity have important effects on the wettability of hydrophobic surfaces and also on the saturation contact angle.

Finally, evidences are provided that the effects observed are not related to the deterioration of the PDMS sample surface due to electrical discharge.

Chapter 5: Charge rate control of electrowetting dynamics

According to the results presented previously, charges seem to play a central role in contact angle variation. Controlling the charge injection rate it is possible to control electrowetting dynamics, therefore new applications can be enabled (i.e. linearization of electrowetting response) and energy consumption could be optimized.

5.1 Introduction

The analytic model presented by Castañer et al. in ref.[64] is applied to electrowetting setups as shown in Figure 5-1, where the droplet is biased by a voltage source and by "corona" ionization. The model describes well electrowetting dynamics in of those setups and two important operational parameters of the droplet movement are underlined:

- The power consumed by the source
- The time to respond of the droplet.

Among the numerous electrowetting applications, some of them as liquid lenses[22] and displays [2, 24, 79] already market products and more, as lab-on-a-chip devices [29, 46, 80, 31] are expected to reach maturity shortly.

Operational parameters such as settling time, power consumed and speed become more and more relevant.

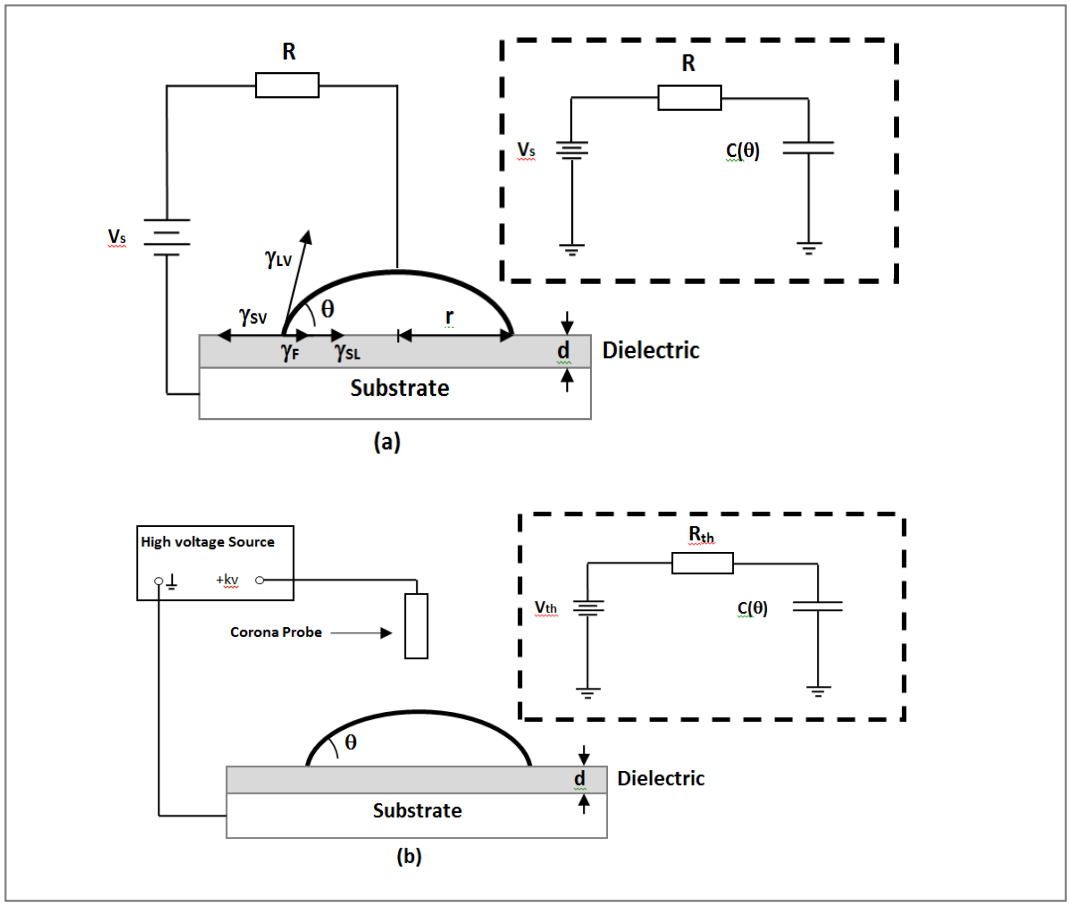

Figure 5-1: *Schematic view of the experimental settings used in ref. [64] for a)standard electrowetting on dielectric experiments and b)electrowetting on dielectric driven by corona charge.*

Hence experiments and models helping to better understand this parameter link to the dynamics, may lead to bridging the gap between numerical and circuitry modelling, such as Comsol.

In this Chapter will be discussed the "charge driving" electrowetting, that is basically electrowetting on dielectric effect by controlling the amount of charges supplied to the system instead of applying a voltage. The model proposed by Castañer et al. in ref.[64] is extended here to a situation where a parasitic resistance and capacitance are present and some preliminary simulated results are presented.

Following, multiphysic simulations are performed and compared with experimental results.

5.2 Charge driving electrowetting

Electrowetting devices are usually biased by a simple voltage source and the energy consumption evolves according to the voltage supply technical features.

Charge driving electrowetting, instead, involves a driving source that is capable (a) to deliver a controlled amount of electrical charge and (b) to set a specific charge delivery rate. Both features are relevant for the droplet dynamics control as the electrical charge delivered sets the steady state of the contact angle and the charge delivery rate sets the transient speed.

The Young-Lippmann equation eq.(1-4) can be written as follows:

$$\cos\vartheta_f = \cos\vartheta_0 + \frac{\varepsilon_0\varepsilon_r}{2t\gamma_{LV}}V_s^{\,2} = \cos\vartheta_0 + \frac{q_A^2}{2\gamma_{LV}C_A} \qquad (5\text{-}1)$$

where ϑ_f is the contact angle value at the end of the transient ($t\rightarrow\infty$), ϑ_0 is the initial value of the contact angle, ε_0 is the vacuum permittivity, ε_r and t are the relative permittivity and the thickness of the dielectric respectively and γ_{LV} is the liquid-vapor surface tension.

As exposed in eq.(5-2), the voltage dependent term can be written as a term dependent by the charge per unit area q_A stored in the droplet-dielectric-substrate capacitance, and C_A represents the capacitance per unit area.

Equation (5-3) steady state solution is reached at when ($t \rightarrow \infty$), thereby indicating that the amount of electrical charge transferred and stored per unit area in the liquid-dielectric-substrate system. Eq. 5-4 does not give any information about the speed of the transient but only that ϑ_f is achieved when a charge per unit area equal to $q_A = \sqrt{2C_A\gamma_{LV}(\cos\vartheta_f - \cos\vartheta_0)}$ is provided by the source to the electrowetting device.

The theoretical analytical model proposed in [64] reports about dynamics of the droplet movement under voltage and charge biasing, without taking into account also parasitic capacitances of wiring and measurement equipment; the transient, hence, depends on both the charge per unit area q_A and the charging rate, which in the end results to be the charging current.

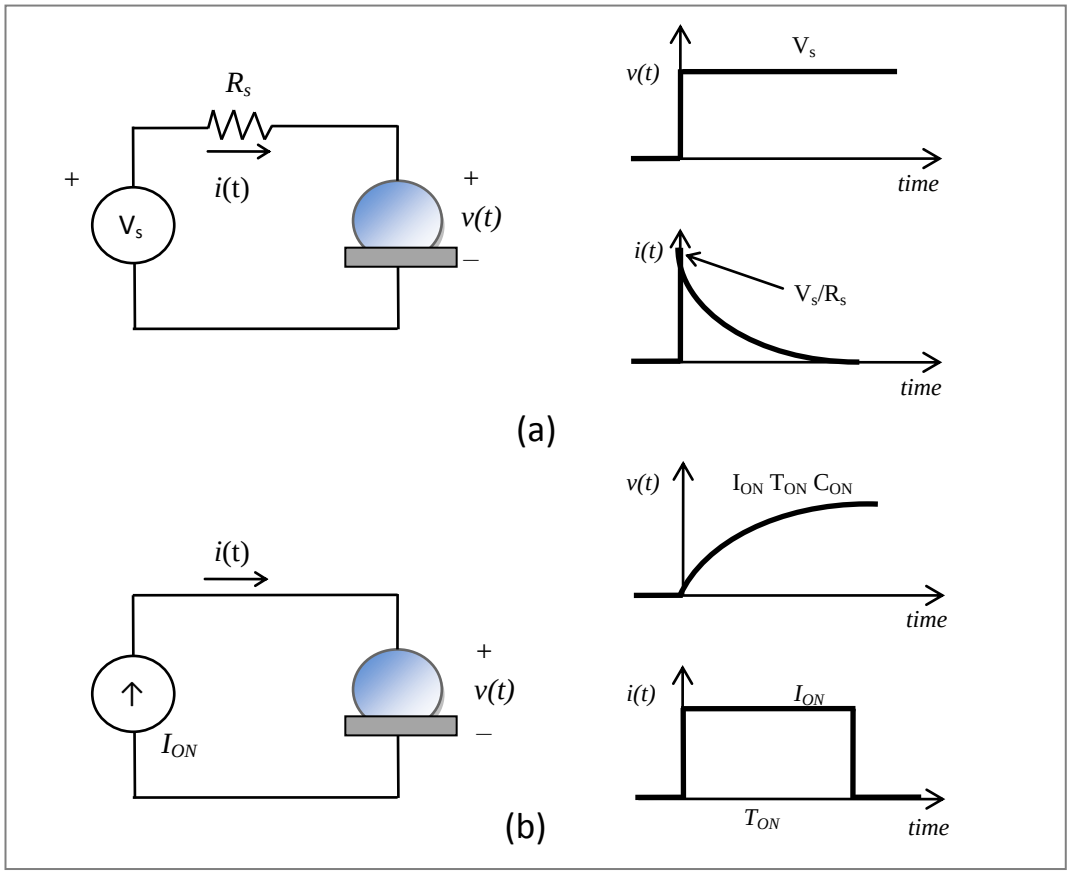

Figure 5-2: *Schematic of a) voltage driven electrowetting on dielectric and b) charge driven electrowetting on dielectric. A) When voltage is applied, charge are injected during the transient showing a high inception peak which value depends on the voltage supply resistance; voltage is constant during all the process. B) Driving electrowetting by injecting charges, voltage starts rising smoothly, while a controlled amount of charges are delivered to the device in a specific time span, depending on the droplet capacity. In this way, droplet dynamics are better managed and energy spent for the system can be easily controlled and optimized.*

In Figure 5-2 it is shown the comparison between the conventional voltage driving, Figure 5-2a, and the charge driving approach proposed here, Figure 5-2b.

The conventional electrowetting voltage driving, shown in Figure 5-2a, consists of a voltage source V_s connected in some way to the droplet. At time $t=0$ a given voltage is applied to the droplet. The internal power source resistance R_s is generally very low and acts as an inrush current limiter, which means that the current peak at the beginning of the transient is only limited by the voltage source compliance.

Figure 5-2*b* shows a practical implementation of the electrowetting charge driving. The circuit consists in a current source of value (I_{ON}) of a given duration (T_{ON}).

The total charge delivered by the source can be calculated as $I_{ON}\mathbf{x}T_{ON}$ and the charge rate (charge per unit time) is I_{ON}. The total amount of charges to be delivered to the device in order to get to the final contact angle ϑ_f is easily related to

$$q_A = \frac{(I_{ON}T_{ON})}{A_F} \qquad (5\text{-}2)$$

where A_F is the area of the drop when the contact angle value is ϑ_f.

As can be seen in the Figure 5-2b, the voltage transient evolves according to the main physical parameters involved in the electrowetting dynamics; the maximum value it can reach is $I_{ON}\mathbf{x}T_{ON}\mathbf{x}C_{ON}$ where C_{ON} is the droplet capacitance at the end of the transient.

In conclusion, the main difference between the two driving methods is that using charge driving method a constant value of the charge rate can be set; using voltage driving method, the charge rate cannot be controlled.

The lack of control of the charge rate of an electrowetting device when biased, due to the complexity of the fluid dynamics of the system, often involves vibration or oscillation modes, that are frequently witnessed during experiments[81], and they have been modeled theoretically[82]. These oscillation modes are excited by a step-voltage waveform, whereas the oscillation can be prevented using the charge driving mode described in this Chapter.

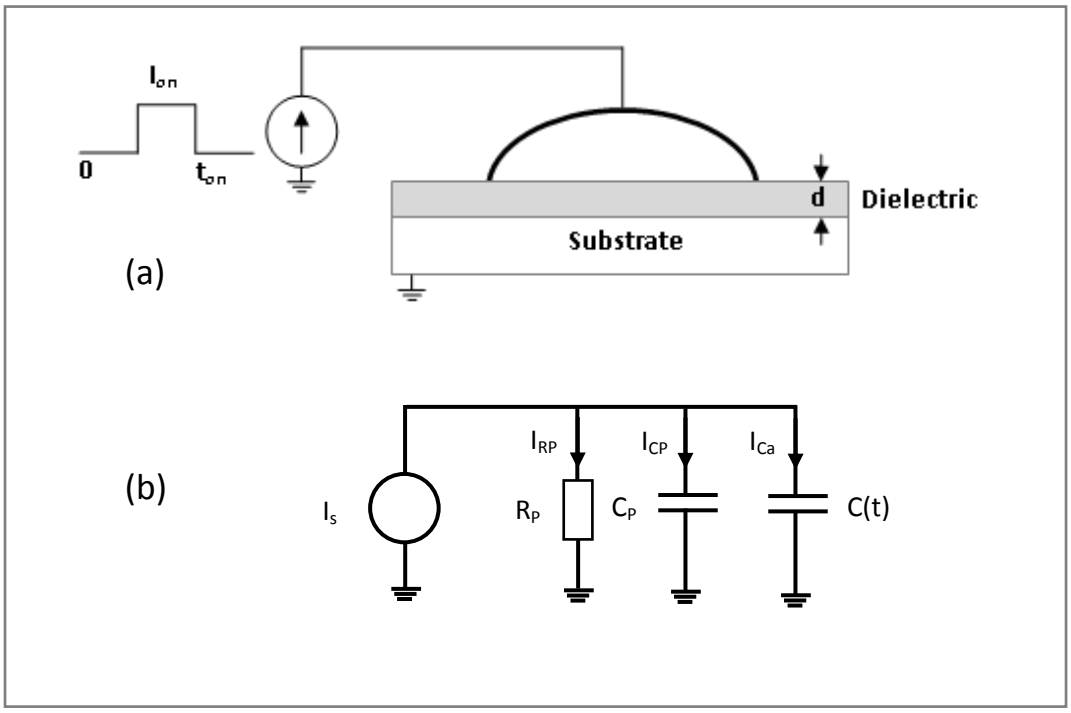

Figure 5-3: *Schematic of the a) charge drive experimental setup and b) equivalent electrical schematic of the system*

In [64] a transient model was reported and validated that couples contact angle variation and charges. In order to take into account also the parasitic behavior of the wiring (C_p and R_P) and the measurement equipment the model has been modified as follows:

$$I_S = C_p \frac{dV}{dt} + \frac{V}{R_P} + \frac{dq}{dt} \qquad (5\text{-}4)$$

Where

$$q = q_A A$$
$$V = \frac{q}{C} = \frac{q_A}{C_A} \qquad (5\text{-}5)$$

$$\frac{dq_A}{dt} = \frac{I_s}{\frac{C_p}{C_A} + A} - \frac{q_A}{\frac{C_p}{C_A} + A}\left(\frac{1}{C_A R_P} + \frac{dA}{dt}\right) \qquad (5\text{-}6)$$

$$\frac{d^2\vartheta}{dt^2} = \frac{1}{\Omega(\vartheta)}\frac{d\Omega(\vartheta)}{d\vartheta}\left(\frac{d\vartheta}{dt}\right)^2 - \frac{d\vartheta}{dt}\left(\frac{\gamma_{LV}\sin\vartheta}{\zeta\alpha\Omega} + \frac{2\pi r q_A^2}{\zeta(AC_A + C_p)}\right) - \frac{q_A I_s}{\zeta\alpha\Omega(AC_A + C_p)} + \frac{}{\zeta_0} \quad (5\text{-}7)$$

$$r = \alpha\frac{\sin\vartheta}{(2 - 3\cos\vartheta + \cos^3\vartheta)^{1/3}} \quad (5\text{-}8)$$

$$\alpha = \left(\frac{3vol}{\pi}\right)^{1/3} \quad (5\text{-}9)$$

$$\Omega(\vartheta) = \frac{(1-\cos\vartheta)^2}{(2 - 3\cos\vartheta + \cos^3\vartheta)^{4/3}} \quad (5\text{-}10)$$

where A is the area, r the radius of the spherical cap droplet base, ϑ is the contact angle, ζ is the friction coefficient, *vol* is the volume of the droplet, C_A and C_p are the capacitance per unit area and parasitic respectively, R_p is the parasitic resistance and finally, q_A is the charge per unit area.

The breakdown of energy coming from the source into components is:

$$E_S = \int I_S \frac{q}{C} dt = \int I_S \frac{q_A}{C_A} dt \quad (5\text{-}11)$$

$$E_C = \frac{q_A^2 A}{2C_A} \quad (5\text{-}12)$$

$$E_R = \frac{1}{R}\int\left(V_S - \frac{q_A}{C_A}\right)^2 dt \quad (5\text{-}13)$$

The conservative and dissipative forces are:

$$E_{cons} = \int_A (\gamma_{LV} \cos\vartheta + \gamma_{SL}(0) - \gamma_{SV})dA \qquad (5\text{-}14)$$

$$E_F = \int_A \gamma_F dA \qquad (5\text{-}15)$$

With this model, a typical example of a liquid droplet sit on a dielectric layer with the following properties is taken into account for an exploratory test: q_0=110°, 20 µl volume of the drop, ζ=4, γ_{LV}=72.86x10^{-3}, γ_{SV}=19.8x10^{-3}, γ_{SL}(0)=44.71x10^{-3}, d=30.28x10^{-6}, ε_r=2.63.

The timing chosen for the test is that in the system is injected positive charge for a T_{ON}, during time T_{OFF}=T_{ON} no charge is injected and then at T_{ON}+ T_{ONFF} is injected the same amount of negative charges, namely 2.642x10^{-8} C.

In Figure 5-4 the effects of selecting different values for t_{ON} are shown. Contact angle as a function of time for a commutation of the source (T_{off}=0.5s), (—)T_{on}=0.05s, (----)T_{on}=0.1s, (-·--·)T_{on}=0.2s. I_{on}xT_{on}=2.642x10^{-8}C.

The effect of the duration of T_{on} is very significant, and therefore it is plausible that the influence of the rate delivery of charges to liquid capacitance does matter on the transient dynamics of the droplet.

In following Sections will be described the experimental setup and the result discussion, where the theoretical model values will be compared with simulation and experimental results.

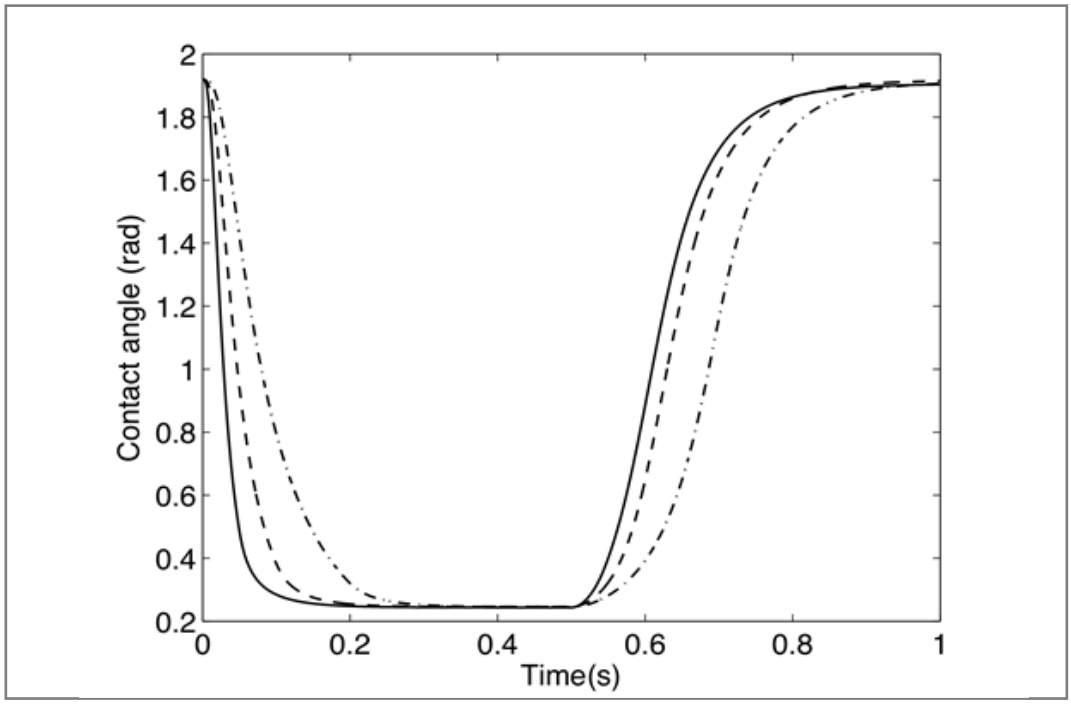

Figure 5-4: *Contact angle as a function of time for a commutation of the source (t_{OFF}=0.5s), (—)t_{ON}=0.05s, (----) t_{ON}=0.1s , (-·-·-) t_{ON} = 0.2 s. I_{ON}xt_{ON}=2.642x10^{-8}C*

5.2.1 Contact angle measurements and simulation: discussion of results and conclusions

Starting from the fabrication data described in the next Section where experimental results are reported and illustrated in Table 5-1, a complete simulation has been performed using Comsol multiphysic. The physics involved are: electrostatics (*ES module*), circuit model (*CIR module*) and two phase fluid flow moving mesh (*TPFMM module*), that is based on *Laminar Two-Phase flow* module, but with the possibility to track geometry movements.

The electrowetting CAD model has been designed taking advantage of the symmetry of the system. The CAD model is in fact, half a section of the drop-based setup. The whole 3D representation can be easily obtained by revolving the results around the symmetry axis.

The physical properties of the system are the same as shown in Table 5-1; the size proceeds from the optical measurements and experiment arrangement (i.e. needle width 0.7mm, drop height/ base diameter 1.09mm/2.16mm).

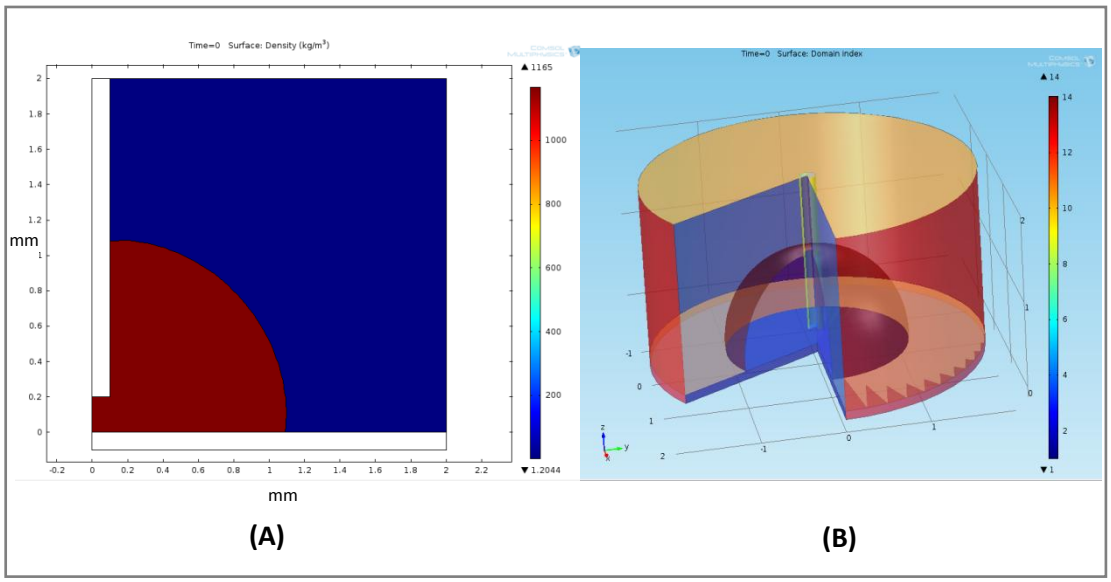

Figure 5-5: *A)The structure 2D axisymmetric designed in Comsol Cad n order to simulate the electrowetting device and B) the revolving of the 2D axisymmetric section that gives a 3D representation of simulation results.*

The current supply has been modeled using the CIR module. The schematic of the current supply is shown Figure 5-6 and the main components are:

- The ideal current generator, which value is I_g=5, 12.5, 20 or 25nA;

- The compliance resistance R_g, which value is 70[V]/I_g which value is between 2.8GΩ and 14GΩ.
- The voltage interface to the physical system designed in Comsol CAD *IvsU*

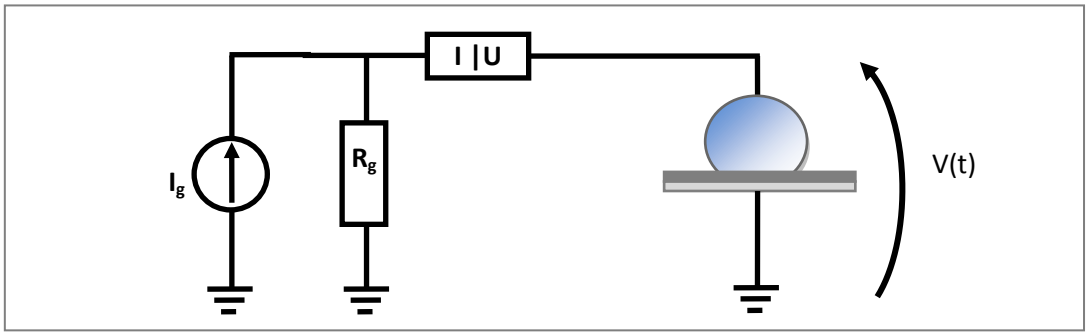

***Figure 5-6**: Voltage limited current supply schematic: an ideal current generator is connected in series with a resistor and an interface between the simulated circuitry and the system designed by mechanical CAD.*

The voltage drop across the external simulated device is then used for solving the Maxwell equations as input of the electrostatic (ES) module. The electrostatic module is interfaced with the circuit modules by setting as power supply a terminal; in the terminal options menu, the terminal type must be set on "Circuit".

The voltage across the *UvsI* device will be fed to the electrostatic module. In the electrostatic module section, is also set the ground (common with the circuit module) and the low permittivity gap boundary. For the low permittivity gap module are used parameters from materials (Teflon relative permittivity: ~1.92[83], SU8-2002 relative permittivity: ~2.8[84]) to calculate the stack dielectric permittivity, that finally results to be 2.6.

Electrostatic force, calculated by the integration of Maxwell stress tensor as mentioned in Chapter 2, is obtained starting from the results that this module outputs.

The model coupling is done by introducing the F_x and F_y electrostatic force as input of the *TPFMM* module, that solves the Navier-Stockes equations.

In *TPFMM* module section are defined mesh movement constraints, wall boundary conditions and, in particular, the initial contact angle is defined by specifying the surface tension values of the system in the subsection dedicated to the fluid-fluid and wall-fluid interface; the fluid surface tension was set to 0.05mN/m, Teflon surface free energy (SFE) is 0.02mN/m and being 100° the contact angle, applying Young equation, eq.(1-3), the liquid-Teflon surface tension results to be 0.043mN/m.

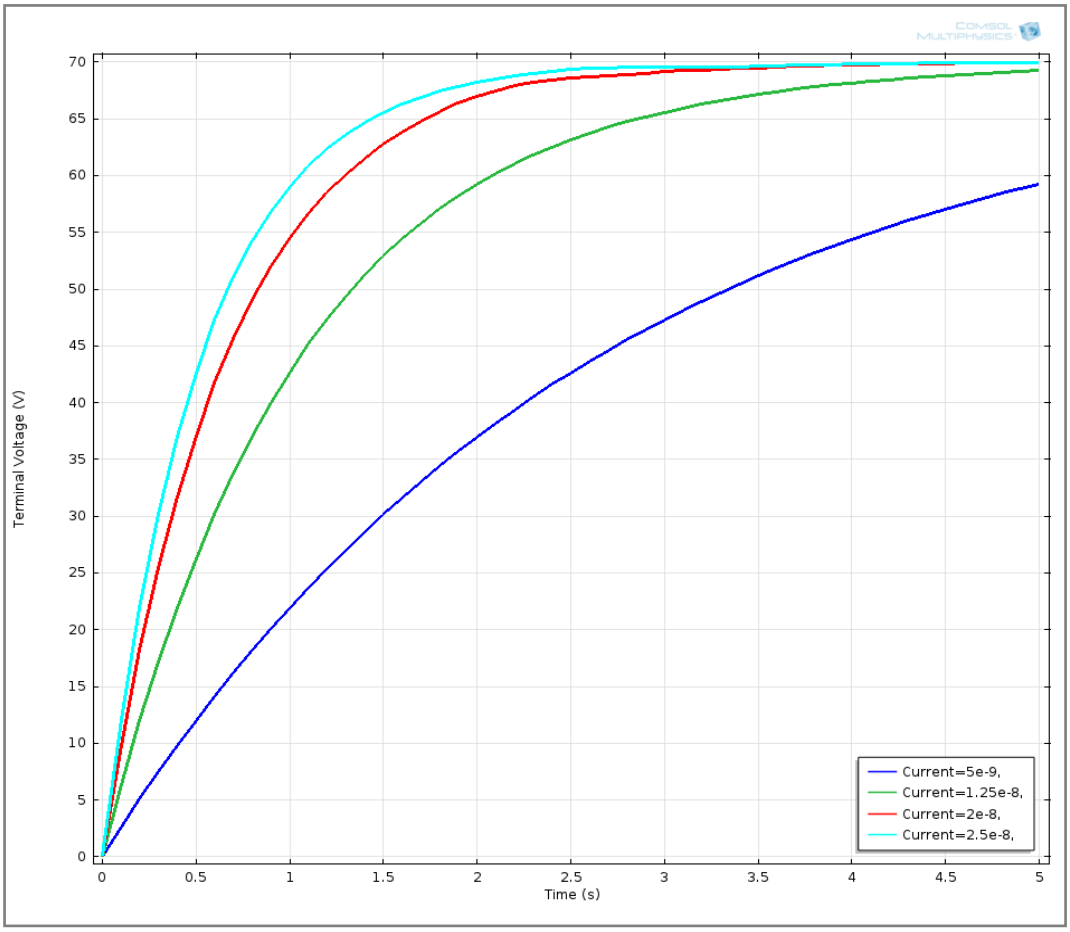

Figure 5-7: *Terminal voltage simulated by combining CIR and ES and then applyied to the geometry simulated. The voltage evolution is completely exponential and it is typical of a R-C network. The time constant depends on the resistance used for voltage limitation and the overall capacity (dielectric layer and liquid droplet)*

In Figure 5-7 are shown the plots of voltage across the device in function of the current. The final voltage tends asymptotically to 70V, although at low current values, already for 12.5nA injected, the saturation time is so high that exceeds a simulation time of 5s.

The voltage behavior is typical of an RC network with time constants compatible with a theoretically calculated capacity value of 1.34×10^{-10}F, assuming a droplet with radius 1mm and physical parameters listed in previous Section.

The time constants values are comprised in the range between 0.5s for 25nA current value and 2.5s for 5nA current value.

The contact angle variation resulted from is shown in Figure 5-8.

Applying the Lippmann-Young equation, eq.(1-4), the theoretical final contact angle is 0.754rad (43.5°).

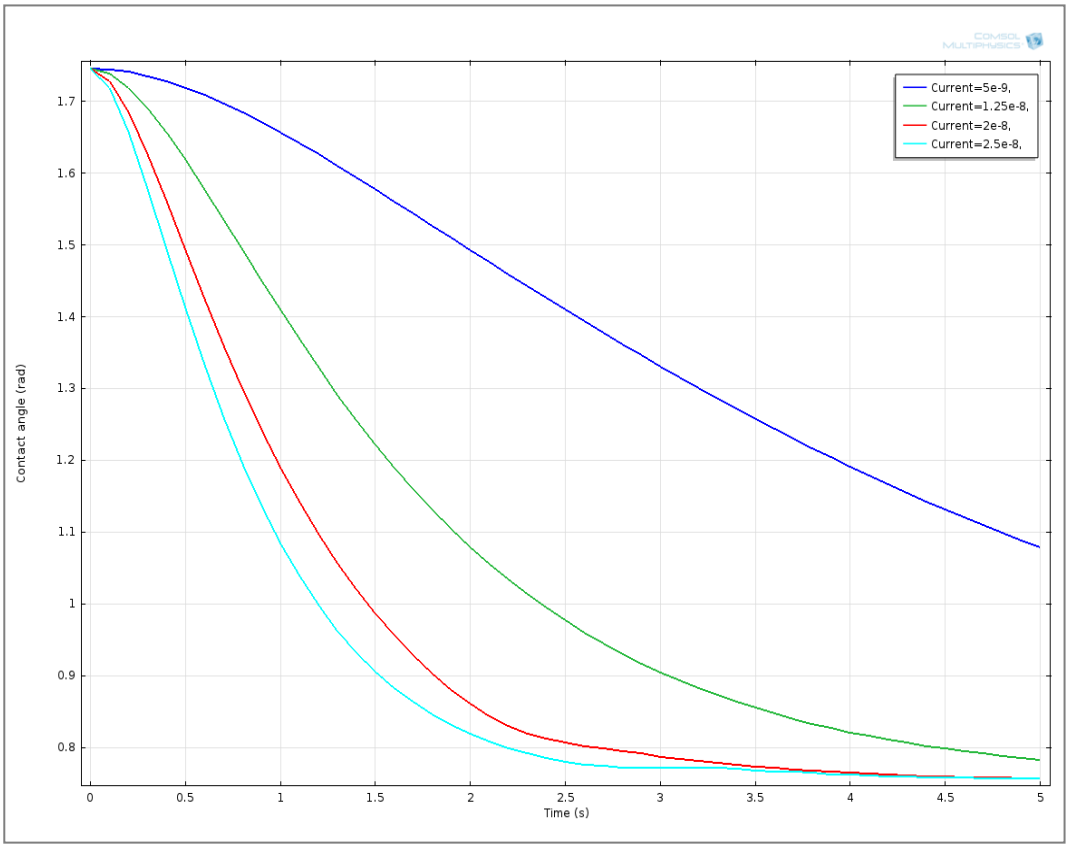

Figure 5-8: *Contact angle variation as a function of time for several current values. The geometry simulated is biased by applying a current ranging between 5nA and 25nA, with a voltage compliance of 70V. The initial contact angle was 1.74rad. Final minimum contact angle reached is 0.754rad, which is also the predicted contact angle by Lippmann-Young equation, eq. (1-4). Nevertheless only with high amount of current injected, in simulated system this value is reached in acceptable short time range.*

The theoretical lower contact angle value is only reached for the two highest current values, highlighting that applying 25nA current, the contact angle drops with oscillations, which are not present in the voltage curve, meaning that the effect is purely driven by the fluidic physics and not a reflex of voltage behavior, but due to the fact that the voltage drops so fast, not oscillating.

In Figure 5-10 it is shown a comparison between experimental measurements and theoretical results obtained using the model reported in[64].

The contact angle measurements reported have been obtained by applying the same current values across the electrowetting setup as per the Comsol simulation: 5nA, 12.5nA, 20nA and 25nA and also the voltage compliance was set at 70V.

The initial contact angle was measured to around 1.74 (99°); the final contact angle, instead, ranges between 1.29rad (73.93°) and 1.37rad (78.55°); compared with previous simulation results obtained with Comsol, there is a clear mismatch: the final contact angle is not aligned with experimental data and also the dynamics does not fit at all; in

particular at low currents, the time constant is extremely big compared with reality, while it is in the correct range for higher currents.

Figure 5-10 shows the theoretical model results fit very well with experimental data: the overall behavior is similar to measurements and the final saturation contact angle measured fits within a negligible deviation range. That corroborates the theoretical model described in [64] fits much better than multiphysic based simulations and also better than Lippmann-Young equation.

5.3 Charge-drive electrowetting experimental setup

The experimental setup designed in order to test the electrowetting devices driven by charge-pumping is based on a precision semiconductor analyzer Agilent 4156C and a contact angle goniometer KSV CAM200 provided with a Basler A601f camera; the synchronization of two instruments is done by using a LED light composed by 7 white light LEDs: the semiconductor analyzer acts as a voltage supply for the LED light and current to the electrowetting device through a probe; the same probe used for current injection is also used as voltage measurement.

The Basler camera equipping the KSV CAM200 can be triggered by measuring the light level of a pixel. The triggering level of the pixel can be “dark” of “white”. When no voltage is applied to the LED and no current is injected, the KSV CAM200 stays in standby; in the moment that the LED is switched ON, and current is injected into the electrowetting system, the pixel chosen as trigger becomes white and that triggers the contact angle goniometer that makes the acquisition of a number of frames.

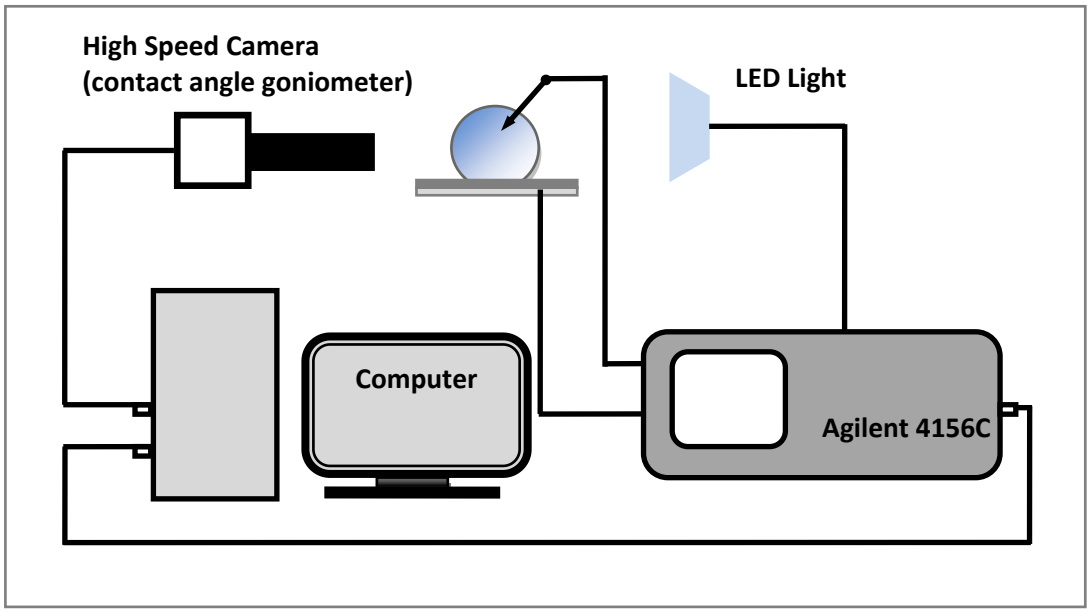

Figure 5-9: *Experimental setup used for the contact angle measurement together with the current injection/voltage measurement over the device under test.*

The first 2 seconds are sampled at 160FPS, after the speed decreases to 1FPS, this is because it is the camera’s frame grabber maximum sample time at full speed. At the same time, the semiconductor analyzer records current and voltage values across the electrowetting device with a sampling time of 560µs. Before measurements, adjustments are made in order to avoid any delay between current injection and LED light switching.

The minimum time is found by adjusting the current across the LED light in order to minimize the switching point. The rise time is measured using the semiconductor analyzer and it is adjusted to 0.3ms by modifying the current compliance. A 0.3ms delay in voltage and current measurement is also introduced in order to synchronize the graphs on the same time base. Of course, both instruments were controlled by a PC.

The experiments were made by placing a 5µl drop of conductive liquid on an electrowetting device. The liquid used was not pure water. In order to extend the lifespan of the electrowetting devices, electrolysis must be avoided. Due to the fact that the Teflon surface presents some imperfections due to the fabrication process and due to the extremely small size of water molecule, it is very likely that electrolysis occurs on the top of the Teflon layer, and therefore compromises the electrowetting device.

Instead of pure water, the use of mixture of ethylene glycol and water/NaCl was successfully tested in the past[82, 81]; adding glycerol[85], electrolysis becomes even less probable. In fact, as glycerol molecules are long and much bigger, therefore pores on Teflon layer are less accessible. Finally, the liquid used for the measurements was a mixture of ethylene glycol and glycerol; the electric conductivity was adjusted by adding NaCl. The physical properties of the liquid used are shown in Table 5-1.

Table 5-1: *Liquid physical properties.*

Density (kg/m^3)	1165
Viscosity (Pa/s)	0.5
Surface tension (N/m)	0.05
Electrical conductivity (µS/cm)	5.5e-6
Relative permittivity	42.5

The electrowetting devices used for the experiments were fabricated starting from a bare glass slide. On the glass slide was previously sputtered a thin layer of aluminum (700nm); afterwards, a barrier layer was spun over the aluminum. As a barrier layer has been used SU8 2000.5, spun at 2000rpm for 65 seconds and post-baked at 95°C during 1 minute.

The result was a 745nm SU8 layer. Upon the SU8 barrier layer has been spun Teflon AF 1600 1%wt, at 2000rpm during 65 seconds and it has been post-baked 30 minutes at 165°C. The resulting Teflon layer was 508 nm thick and the surface showed a hydrophobic behavior.

The droplet was contacted from the top using a gold needle probe, while the bottom electrode was grounded. The variables registered were the contact angle, the voltage across the terminals and the current delivered by the output of the 4156c Agilent Precision Semiconductor Analyzer.

From the raw measurements the total energy delivered by the source was calculated by time integration of the *Voltage x Current* product.

5.4 Measurements and simulation results

The measurements using the KSV goniometer and the Agilent semiconductor analyzer have been done on the same set of electrowetting devices, fabricated and characterized as reported in Section 5.3. The contact angle values have been recorded at full speed (160 FPS) during the first 2 seconds of the measurement, due to the cache memory limit of the camera, and then the speed has been decreased to 1 FPS. The electrical measurements have been done sampling the voltage across the electrowetting device at 560µs; the maximum value of the voltage was 70V, set as compliance of a current source. The current source, instead, has been set between 5nA and 25nA. The initial contact angle of the 5µl liquid drop deposited on the Teflon surface was typically 99° while the final contact angle was comprised in the range between 74° and 79°. The measurements conditions were kept constant: temperature at 23°C; humidity around 30%. The differences are attributed to the fact that although the measurements were made on the same substrate they were made sequentially and local changes on the dielectric thickness or surface state cannot be excluded from one measurement to the next.

The main measurements results are reported in Figure 5-8 and Figure 5-11.

In Figure 5-8 are shown the contact angle values recorded compared with the simulated results using the model proposed by Castañer and Di Virgilio [64], where in Figure 5-11 is shown the voltage evolution recordings across the electrowetting device in function of time for the different values of I_{ON} between 5nA and 25nA.

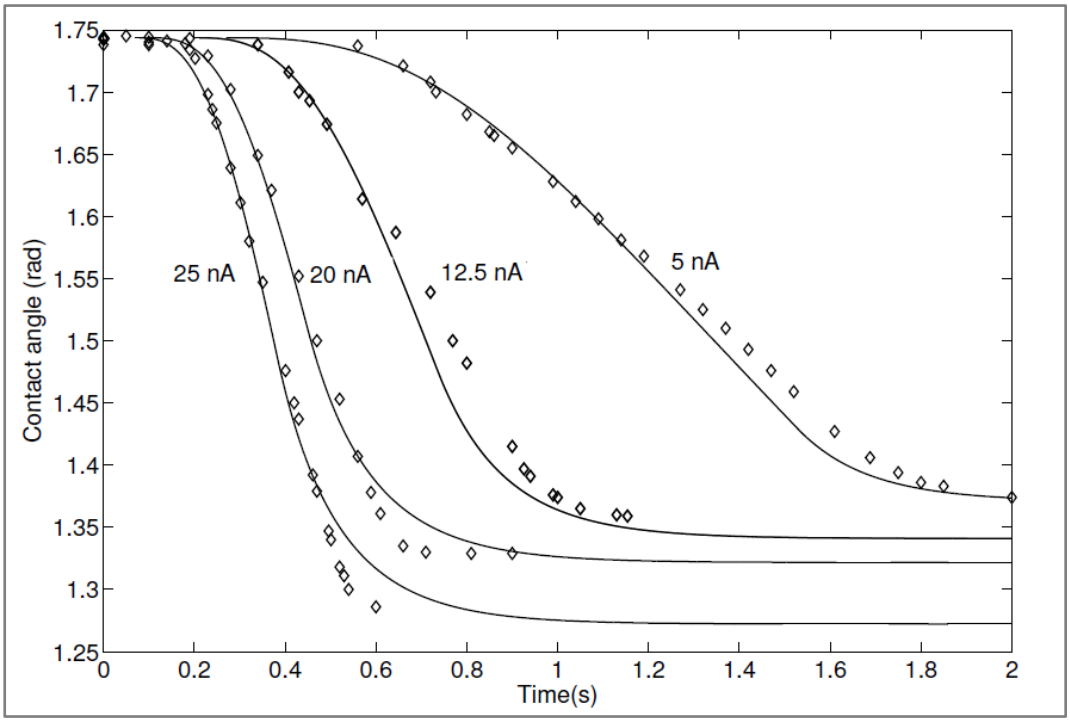

***Figure 5-10**: Experimental contact angle measurements for several values of current (▫) compared with model [64] prediction results (–) when parasitic capacitance C_p=0. The initial contact angles lay in the range between 99.65° and 100.5°, the final contact angles are comprised between 73.93° and 78.55°.*

5.4.1 Electrical measurements across the electrowetting device: discussion and conclusions

The electrowetting device has been submitted to extensive experimental sessions by controlled injection of current and measuring relevant parameters.

With current injection into the electrowetting device it is simultaneously recorded the evolution of the voltage across the device. This information is valuable at the moment of the estimation of the capacitive coupling of the liquid with the device.

The capacity value of the system is easily measured and the device can be fully understood if these data are cross-linked with contact angle variations.

In Figure 5-11 are reported several plots of the voltage evolution in function of time for several values of current.

At first, a superimposed ripple can be observed over the measurement and it is due to the 50Hz of the supply voltage network, therefore it can be neglected.

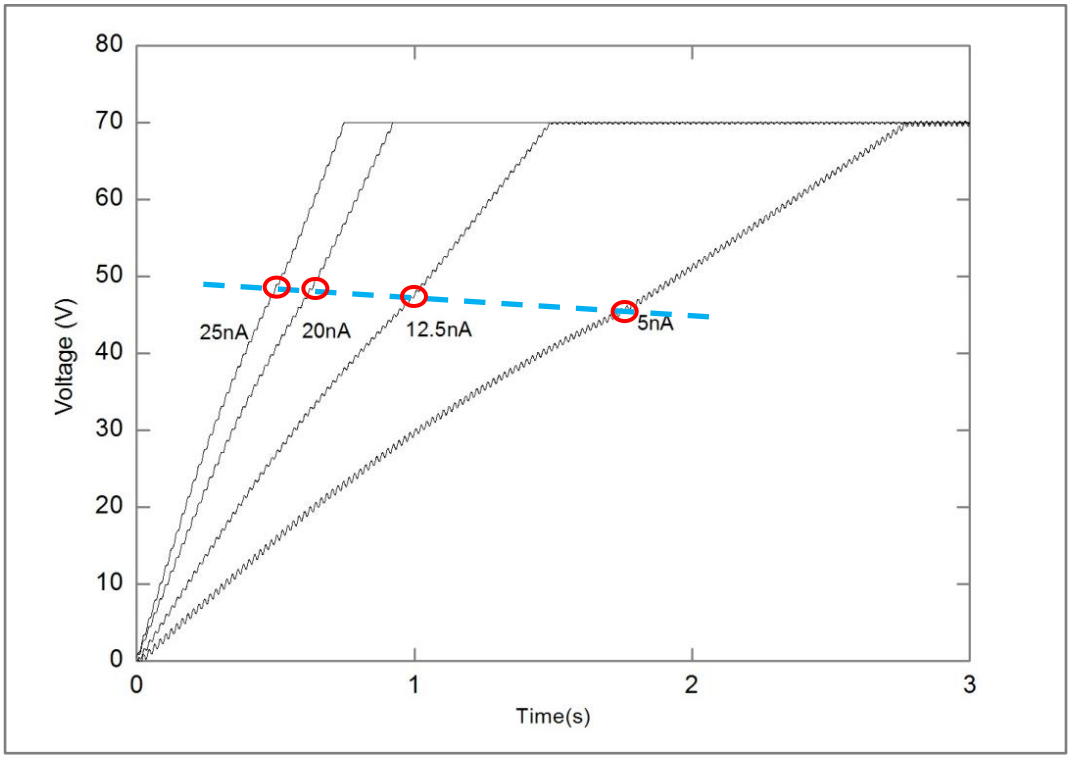

Figure 5-11: *Voltage measured across the electrowetting device under test while injecting current in the range between 5nA and 25nA. The voltage firstly evolves exponentially, where the time constant is driven by the resistance and capacity of the system. At a certain moment, it starts to evolve linearly; this happens when the contact angle saturates and the droplet is still. The voltage level at which this phenomenon happens, grows with current.*

Furthermore, the curve plot can be split into three zones: the first zone is characterized by the fact that the voltage evolves non-linearly; the second zone shows a linear growing of the voltage until the compliance value, the third zone shows the system is in steady state condition, where the voltage value is equal to the compliance of the current supply and no current is injected into the system.

Zone 1: at the beginning the device is not charged. When current is injected, the charges start accumulating on the surface of the droplet. The droplet modifies its boundaries as the TPL. Three main capacities can be identified in the typical electrowetting device: the substrate capacity, the dielectric layer capacity and the liquid droplet capacity; only the last one can modify its value due to the moving TPL.

At the beginning, the smaller and leading capacity is the one of the liquid drop, as the liquid is conductive but the charges across it are unbalanced and they stay unbalanced as long as the TPL moves. The movement of the contact line results into a larger capacity as the contact angle decreases and the drop height also decreases. Current is injected in this phase.

Zone 2: when the voltage stops evolving non-linearly and starts evolving linearly, could be named “switching point” and it is the moment when the TPL stops moving, the contact angle transient is over and the liquid interface stays still. The dominant capacity becomes the dielectric layer’s one, therefore the slope defines the capacity of this layer as it is assumed the liquid is conductive. In this phase, current value is still higher than 0 as charges are injected until the device capacity is charged fully.

In Figure 5-12 are shown two curves almost superimposed one to each other, one being the time at which contact angle saturation is reached and the other being the time at which the voltage stops evolving non-linearly (for several values of I_{ON}). Also, it is possible to conclude that at higher current values, the switching point is reached faster.

Zone 3: Once the compliance voltage is reached, the system enters in a steady state: the voltage reaches the compliance of the voltage supply and does not vary any more. On the other hand, the current injected is 0 as the capacitive coupling is reached.

At a glance, the plot of the contact angle saturation and the one of starting point of linear increase of the voltage across the device overlap on each other, Figure 5-12, and this corroborates that a moving droplet polarized with charge injection varies its capacitance while the contact line moves.

In Figure 5-13 it is compared the switching voltage value and the time when the switching voltage value is reached: when the charge injection rate is higher the switching voltage is reached in about 0.5s (25nA current value) while it takes more than 1.6s if for lowest rates (5nA current value). On the other hand, as it can be seen from the right axe, the voltage reached when switching point happens, also varies and the trend is the opposite: if high current is applied, and therefore injection rate is high, the voltage at which switching point happens is lower than if low current is applied. In particular, the switching point voltage ranges 43.2V and 47.3V, being the impact of the charge driving much smoother on the switching voltage than on the switching time.

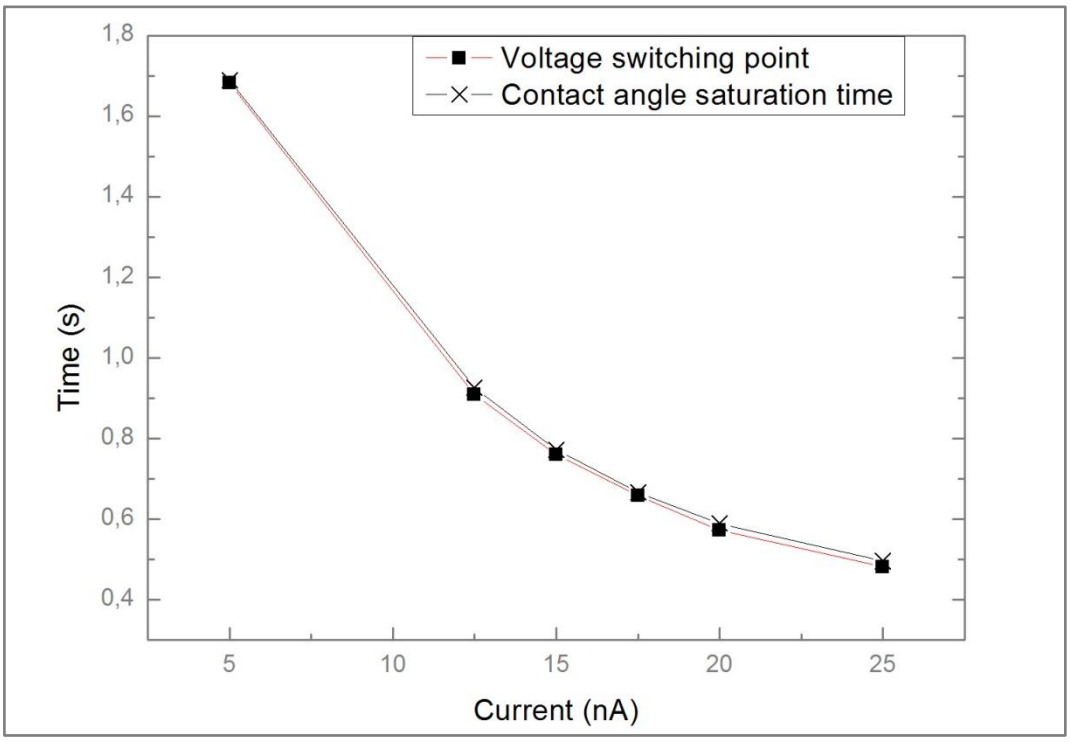

Figure 5-12: *Comparison between voltage switching point and contact angle saturation time. Both plots are shown on the same graph, being the x-coordinate, the current applied and the y coordinate the time. It is possible to conclude that the switching point happens when the contact angle saturates and the TPL does not move.*

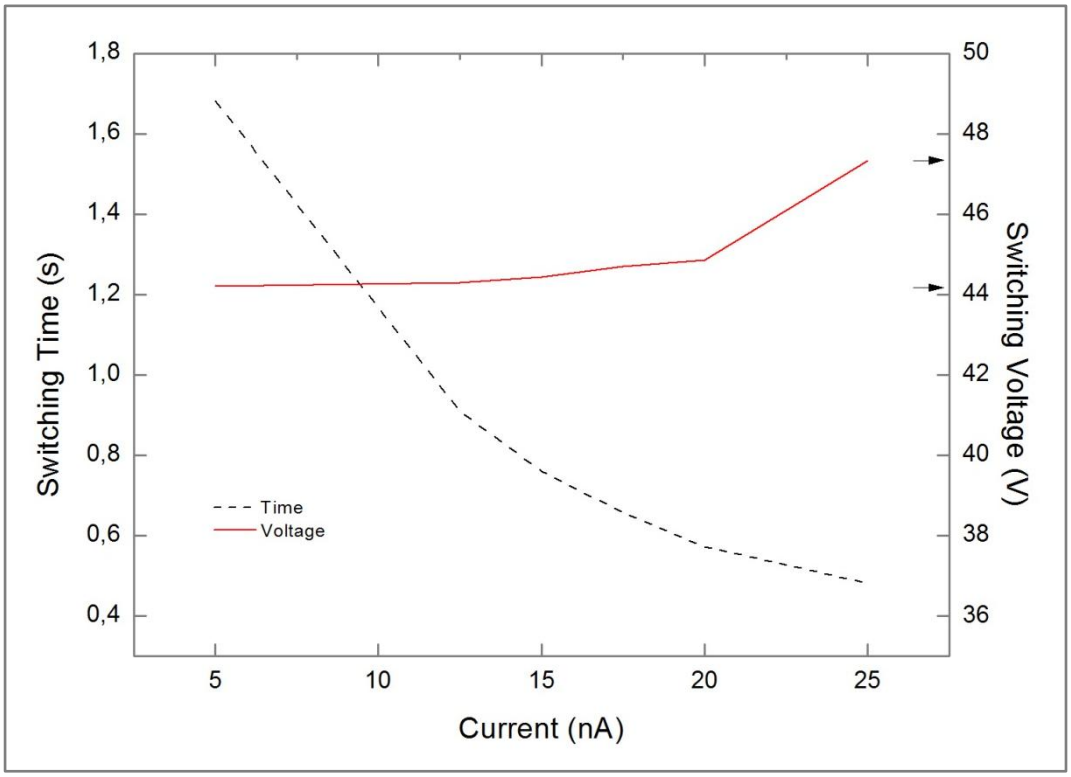

Figure 5-13: *Plot of the comparison between the trend of the time at which the voltage switches from exponential to linear evolution and the voltage at which the switching happens. It is shown that at higher current injected, the switching point is reached much faster, ranging from more than 1.6s for 5nA to 0.5sfor 25nA current. On the other hand, the voltage at which the switching happens is comprised between 44.4V and 47.3V.*

As a resume, the following statements can be written:

- The voltage increase across the droplet is non-linear when the TPL moves;
- The switching point happens when the contact angle saturation is reached;
- The non-linearity is due to the equivalent capacity of the liquid droplet;
- The switching point is reached faster with higher current values, as per the contact angle saturation.
- The switching point, for the devices under test, happens at a voltage comprised between 44.2V and 47.3V, and it is higher for higher current values. This is maybe a cause the contact angle saturates at lower values.

Plotting derivative with respect to the time of the voltage and multiplying it by the inverse of the current injected it is calculated of the capacity of the device: in Figure 5-14 are reported the values of the measured capacitance across the device for several current values taking into account the Zone 1 of the voltage measurement. The initial capacitance measured is in the range of 0.2nF. The final capacity value reached in this phase changes according to the current injection value and it is comprised between 0.3nF and 0.36nF. When the droplet is charged and the contact angle transient is finished; the leading capacity is the one of the substrate and it is smaller than the switching point value. From the linear zone in the voltage plot, Figure 5-11, it is possible to experimentally derive the value of the stack capacity that results to be $2.061\pm0.12\text{x}10^{-10}$F. This value is in line with calculated and simulated capacity values that are respectively $1.26\text{x}10^{-10}$F and $9.89871\text{x}10^{-10}$F. That means that the assumption of the use of a spherical cap to model the droplet shape made by Castañer and Di Virgilio in ref.[64] fits very well with experimental data and therefore it is a good approximation. The results are resumed in Table 5-2.

***Table 5-2**: Summary table of the electrowetting system capacitance, measured, calculated and simulated.*

Method	Value	Formula
Experimental measurement	$2.061\pm0.1\ 2\text{x}10^{-10}$F	$C = \frac{dV}{dt} * \frac{1}{I_g}$
Calculation by material properties	$1.26\text{x}10^{-10}$F	$C = \frac{\varepsilon_0 \varepsilon_r A}{d}$
Simulation (Comsol ES module)	$9.89871\text{x}10^{-10}$F	Maxwell eq. solving

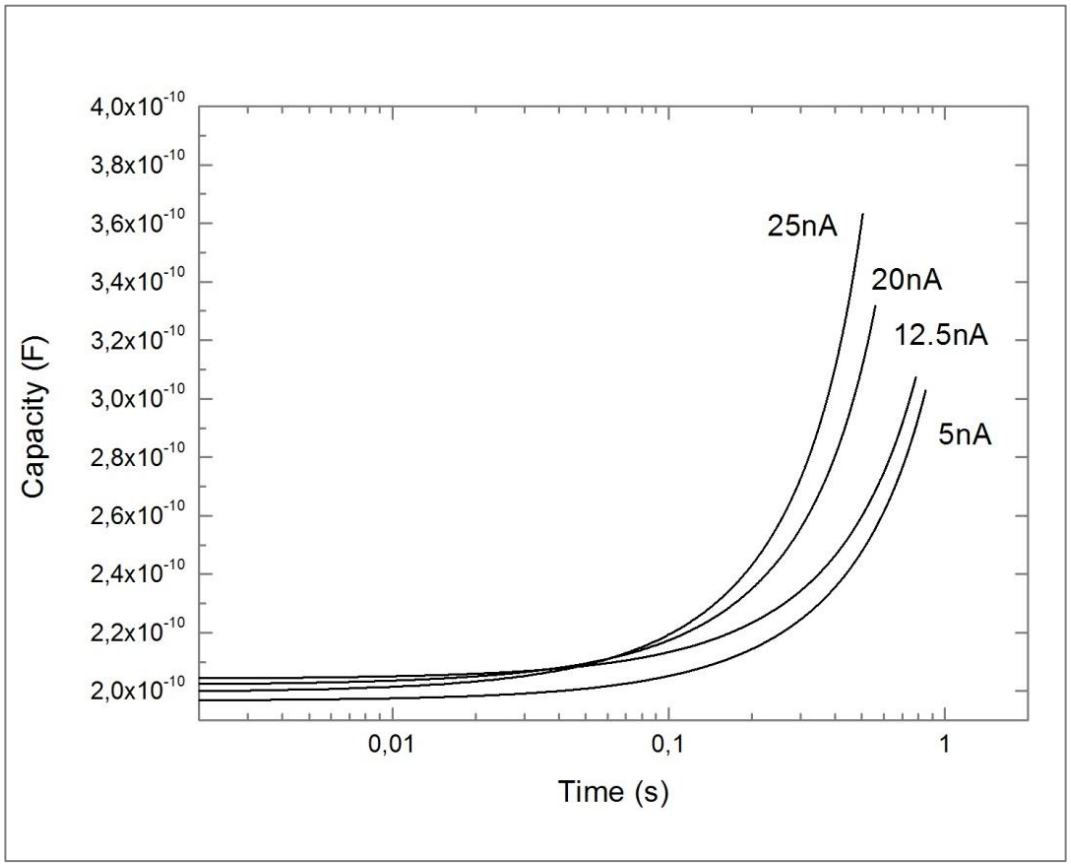

Figure 5-14: *Capacity measured across the electrowetting on dielectric device under test. The starting point is very similar for all the experiments run; on the other hand, the dynamics are different. The final capacity value reached is higher for higher driving currents, as well as the speed of increase.*

5.5 Speed control and energy reduction in electrowetting

The contact angle recorded during experimental session and depicted Figure 5-8 shows clearly a dependence of charge injection and speed. Analyzing the data obtained, for each value of current driving it can be computed the value of the fall time, defined as time difference between the 10% and 90% of contact angle variation, that means the point where the contact angle is $\vartheta_0 - 0.1*(\vartheta_f - \vartheta_0)$ and the point where the contact angle is $\vartheta_0 - 0.9*(\vartheta_f - \vartheta_0)$.

This calculation gives a unique measure of the transient speed. Moreover by time integration of the instantaneous values of the product $Current \times Voltage$, the amount of energy drawn from the source can be calculated.

The source energy is shown in Figure 5-15: both results as a function of the source current. As expected, the higher the current involved, the higher the energy drawn from the source. On the other hand, the fall time is steadily decreasing as the current of the source is increased. This indicates that the average speed of the transient increases as the charge rate increases. It can also be seen that the values of the energy drawn from the source range from $2x10^{-7}$J to $3x10^{-7}$J and increases as the current of the source increases.

In Figure 5-15 the calculated results from the theoretical model reported in [64] are also shown in solid lines. As can be seen the energy consumed from the source is underestimated by the model, mainly due to the simplifications done as it is only considers the friction losses.

Even if the approximation is good, it is clear from the experimental results that other losses have to be taken into account to better describe the phenomenon. These limitations are not seen on modeling of the speed of the transient, which is much better adjusted.

Furthermore, in Figure 5-16, it is shown the comparison between the energy drawn by charge drive, the predictions done applying the theoretical model and together with the conventional electrowetting voltage driving. It is very clear that conventional voltage driving of an electrowetting device is heavily inefficient.

In Figure 5-17, where the contact angle is plotted as a function of time, it can be seen the effect of the inefficient driving, not only energy wise.

In fact, oscillations are observed and much faster settling time than that registered in Figure 5-8. We have also computed the energy consumed from the source in this case and we have found a value of $5x10^{-6}$ J.

Oscillations in liquid droplets have been systematically observed and modeled [59]and nonlinear effects have also been observed when the amplitude of the oscillation is 10% larger than the radius of the drop [86]. In our measurements our interpretation is that the oscillations modes excited by the sharp voltage drive mode leads to larger viscous losses than in the charge drive mode which is smoother.

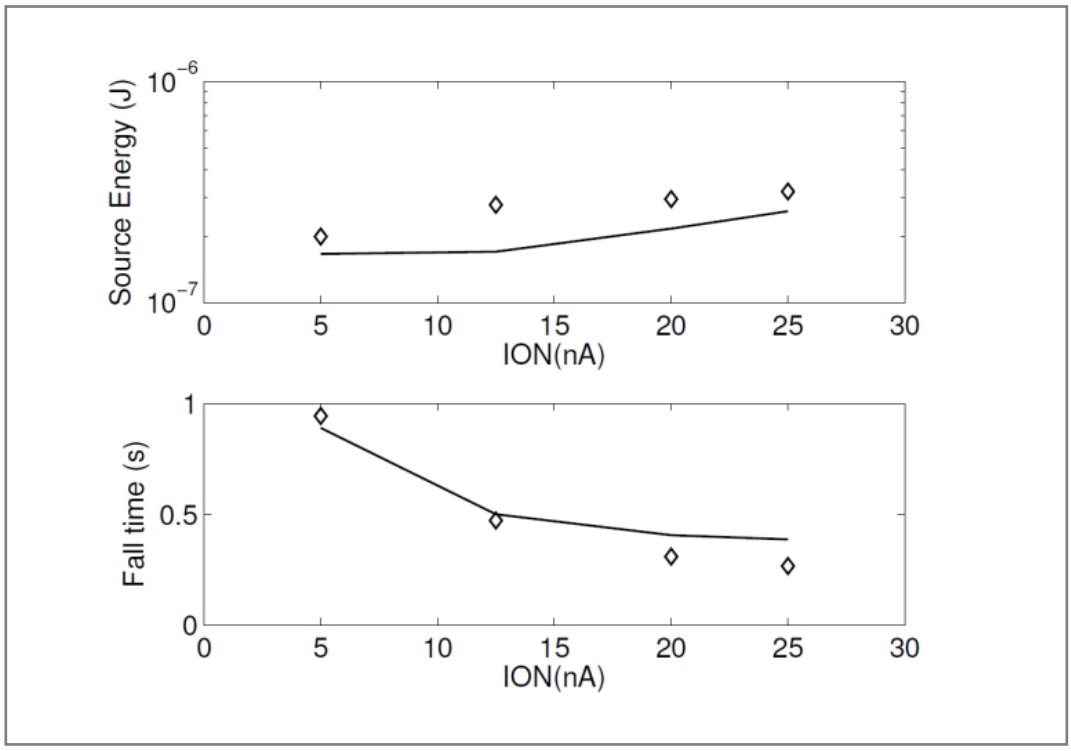

Figure 5-15: *(Top) Energy drawn from the source as a function of the driving current (bottom) Fall time as a function of the value of the driving current. Solid line represents the theoretical results obtained applying the model by Castañer and Di Virgilio [64]*

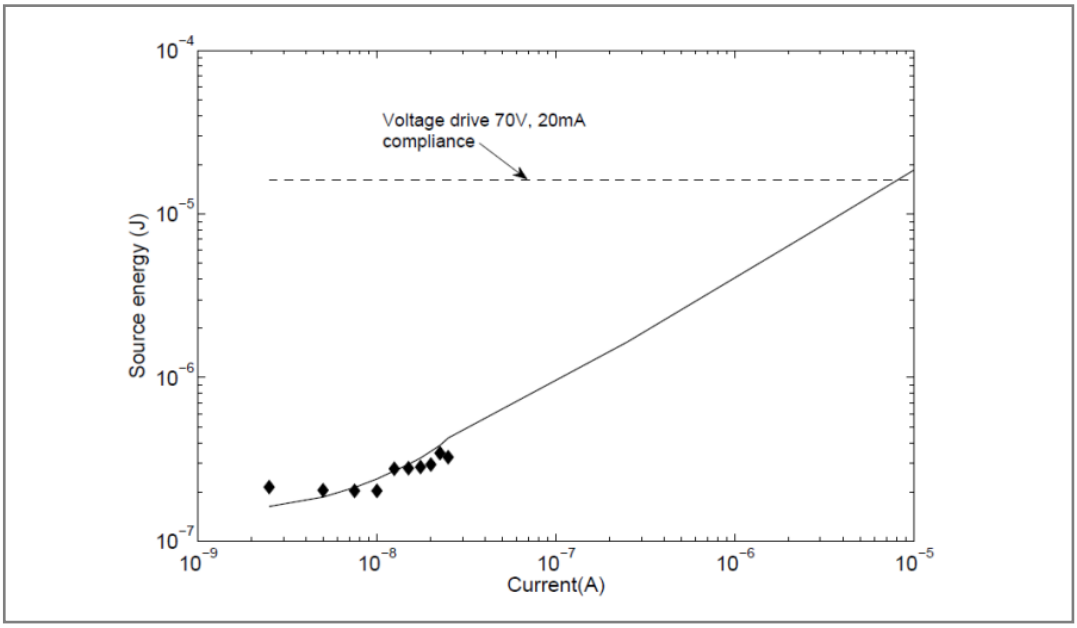

Figure 5-16 *Comparison between energy source drawn by charge driven electrowetting (◆),theoretical predictions done using the model by Castañer and Di Virgilio [64] and the energy drawn by conventional electrowetting voltage drive.*

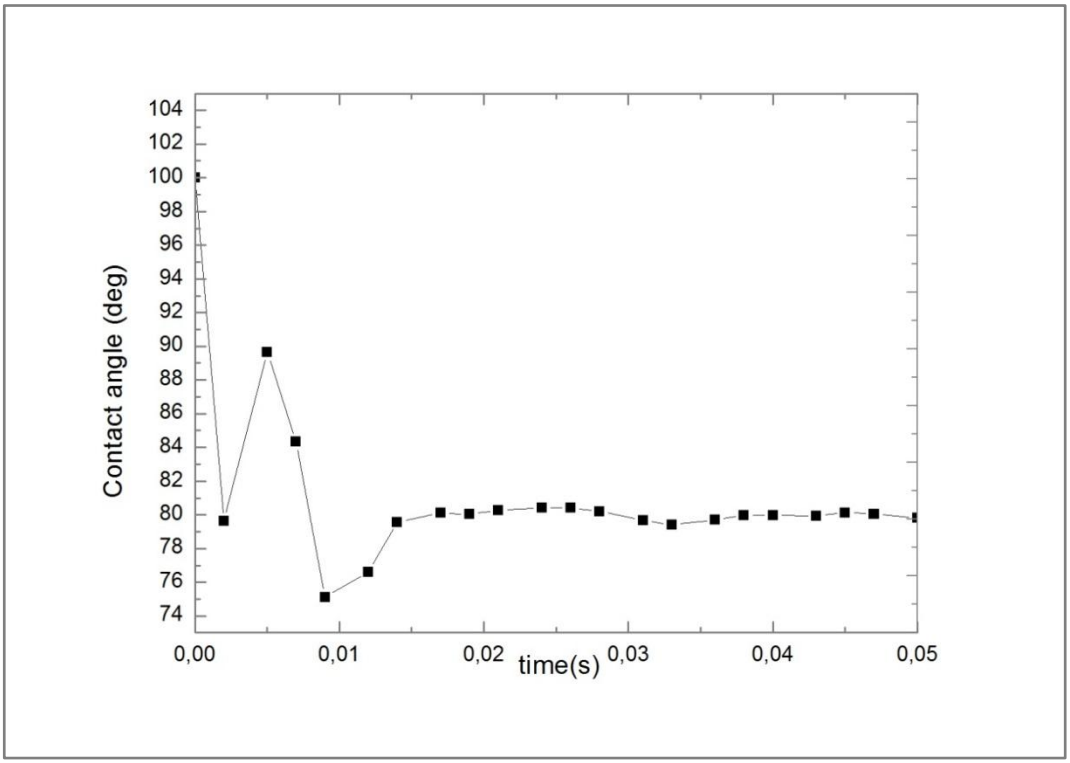

Figure 5-17: *Contact angle measurement driving the electrowetting device by a voltage source, 70V with 20mA current compliance. Oscillations are observed and large overshoot appears at the very beginning of contact angle variation.*

5.6 Conclusions

Taking as starting point the findings reported in Chapter 4 about the role of charges in contact angle variation and taking into account the work done by Castañer et al in [64], in this Chapter has been presented a novel method for the electrowetting device diving, that uses charge injection by a current supply instead of voltage, as commonly is done.

After having simulated the circuit and the geometry using a multiphysic simulator such Comsol, coupling, circuit simulation, electrostatics and fluid dynamics, several results have been obtained.

Those data have been compared with experimental results, during which, current, voltage and contact angle have been recorded.

The first interesting result is that the speed of contact angle varies according to the charges rate, the higher the charges are injected, the faster the contact angle drops. That shows a clear role on the charge dynamics over the TPL.

Nevertheless, voltage seems to not evolve exponentially, as it is proper of a capacity coupled device as an electrowetting device is. Instead the shape of the voltage changes with time. In particular, the evolution of the voltage is exponential as long as a contact angle variation happens. When the contact angle is still, in saturation region, the voltage evolves linearly.

A clear relationship of this phenomenon has been reported in Figure 5-12, where the saturation time and the switching point from exponential to linear are plotted in function of current value: the two curves almost overlap. Furthermore, it has been shown that the switching point is reached faster at higher current driving values, with very large differences between low and high current values; on the other hand, the saturation voltage also varies, being higher at higher at higher driving current values, nevertheless the impact is not so significant, as reported in Figure 5-13.

When system reaches the saturation, another interesting finding has been reported: the capacity, which is evolving differently if the contact angle is varying or not, shows a different increase rate, reported in Figure 5-14. In the same Figure, it is possible to see how at higher currents driving the device, the faster the capacity increases and the

highest is its final value. The capacity measured, is compared with the simulated by Comsol and calculated theoretically. This shows that the spherical cap approximation is not so distant from the reality, being an acceptable approximation, as all the values are in agreement being all close to each other.

The final part of the Chapter, relates about the energy consumption of the current driven system, as the charges are only injected in the very beginning. The comparison between the measured values and the theoretically calculated using the model by Castañer, shows that the model underestimate the energy consumption, probably due to the fact that some dissipative phenomena are neglected, while it fits very well the timing of contact angle variation.

Comparing the experimental results driving the electrowetting device by current and by voltage, and superimposing the theoretical model calculation of the energy consumption at the supply, it is clearly shown in Figure 5-16 that the current driving method not only unlocks the possibility to drive the device smoother, but also, efficiently, as the energy consumed is far less compared to the conventional voltage driving.

Chapter 6: Conclusions and future work

For more than 100 years, electrowetting has only been performed applying voltage, when the role of charges is fundamental. Ionizing charges can unlock a liquid handling technology performed without the interaction between liquid and upper electrode. Charges also are the key for a smoother and more efficient electrowetting driving; electrowetting pixels can be more easily drivable for gray-scale applications and liquid lenses can be more easily and precisely actuated. Being those last ones, technologies usually embedded on portable devices, energy efficiency will be extremely profitable.

6.1 Concluding remarks

This work relates about the phenomenon of the electrowetting on dielectric driven by charges instead of voltage.

In particular, in this work has been reported the fundamental role played by charges in contact angle variation, that before was never taken into account before.

In particular, two main findings have been reported:

1 The ionization of the surrounding of a droplet can induce a contact angle variation
2 The injection of charges at a controlled rate has strong impact over the dynamics of the contact angle and also on the energy consumption of the system.

Also, the contact angle saturation has been studied and some interesting effects of the charges have been reported. Unfortunately, this issue remains still open and unsolved even though some more information have been added.

In addition, a full multiphysic simulation of electrowetting has been performed, taking into account the power supply, the electrostatics and the fluid dynamics.

6.2 Contactless electrowetting

In this work the contactless electrowetting phenomenon has been presented. This phenomenon consists in varying the contact angle of a liquid drop sit over a hydrophobic surface by applying charges ionizing the surrounding of the drop.

The experiments have been performed using a single ionization source, before a ion gun and after a corona charge device; nevertheless liquid has been moved from its initial position due to the fact that contact angle does not change symmetrically over all the TPL.

If a matrix of ionizing needles can be fabricated, and each one of the needles addressed singularly as per creating a single charge source point, therefore the droplet can be easily moved along a path.

This technique could unlock a liquid handling over a surface, plane or not, without having to put in direct contact the liquid to a counter electrode. This feature avoids cross contaminations in case of different fluids, and this is extremely important in applications like genome sequencing or in µTAS. A simple schematic of a contactless electrowetting device is shown in Figure 6-1, where the major challenges are

- Voltage addressing to each needle, that is quite simple using a voltage control active matrix
- High quality hydrophobic coating using several high dielectric strength barrier layers in order to prevent sparks and dielectric damages.

On the other hand, there is no need to fabricate any special patterning of the bottom electrode, as it only serves to address the electric field.

Therefore the operations would be quite easily performed using a simple addressing logic. On the other hand, only liquid motion has been observed, while any study or investigation has been done in liquid manipulations basic functions, like splitting, merging, mixing and dispensing.

There is still a long path to walk towards a fully functional contactless electrowetting device.

As an addition to the fundamental study of electrowetting phenomenon, it has been reported the effects of humidity in contact angle saturation: in particular that as the humidity of surrounding air increases, also the contact angle at saturation increases, showing that the recombination rate at the TPL is also and strongly influenced by the surrounding environment.

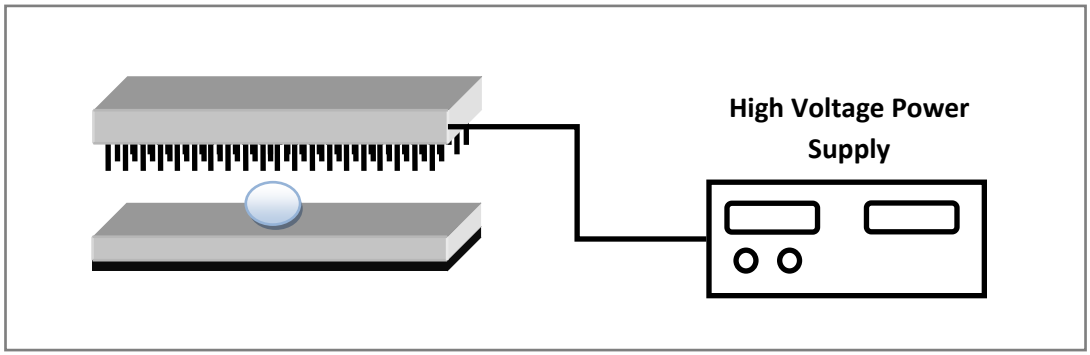

Figure 6-1: *General schematic of a contactless electrowetting device for liquid handling.*

6.3 Charge driving electrowetting devices: main advantages

The injection of charges at a controlled rate, into a standard electrowetting device, has been discussed deeply in Chapter 5.

First of all, the system has been simulated with the help of multiphysic simulations and applying the model introduced by Castañer [64], taking into account the parasitic effects of wiring on the full system.

After that, the system has been measured by injecting charges at several rates. Finally the results have been cross checked.

The simulations done applying the theoretical model by Castañer and the multiphysic simulations show the contact angle at different speeds, even though the theoretical model by Castañer is more accurate than the one developed in Comsol. The voltage calculated is exponential as the system is capacitive coupled.

In reality, the measurements show that the voltage is not completely exponential, as when the contact angle saturates, it increases linearly.

As expected, the speed of contact angle variation varies in function of the charge rate.

This is the main goal of the Chapter, as the control over the motion of the TPL is extremely beneficial for the two more mature electrowetting technologies: electrowetting pixels and electrowetting lenses.

One of the challenges of electrowetting displays is to show a good, and linear, response to the voltage applied in order to get a characterization of a gray scale excitation signal over at least 256 levels.

This is not possible, at the moment, as the electrowetting pixel suffers a high hysteresis and also the non-linearity experienced by applying a voltage step starting the pixel opening complicates the driving. If charge rate is controlled, the response can be quite easily characterized; pixels can open more smoothly, therefore a better linearization can be achieved.

In the same way, electrowetting lenses are nowadays affected by problems in controlling the focal dynamics. The dynamics of the internal interface between oil and conductive liquid is the key to achieve a fast focusing and precision in depth of field.

By well characterizing the TPL speed and dynamics, a fine position control in closed loop can be easily implemented.

The big importance, therefore, of the charge injection rate in an electrowetting device resides in the fact that the dynamics can be characterized for the design of a fine closed loop control.

Together with the easier controllability of droplet dynamics, injecting charges in a controlled way optimizes the power required for operations. The amount of energy required has been found to be from 10 to 100 times smaller, reported in Figure 5-17, than with conventional driving. As typically electrowetting displays and liquid lenses equip portable electronics such as smartphones or tablets, the energy consumption is a key point in making the technology attractive to the market.

As last remarks, it was also observed that the saturation angle has some relationship with charge injection rate: the decreasing at higher charge injection rates.

The fact that the contact angle saturates at lower values is seen to be due to the fact that the voltage “switching point” from exponential to linear increase happens later at higher charge rate, Figure 5-12.

Annex I

A. Schwarz-Christoffel transformation

Maxwell equation solving is not an easy task when the shape under analysis is far from being a pair of infinite parallel plates. Schwarz-Christoffel transformations help to transform complex shapes into easier ones, where Maxwell equations are solvable.

The water drop under depicted in Figure 3-9 can be sketched as the physical plane *Z=x,y* depicted in Figure A-1. In plane *Z* is considered a triangle with vertices A_1, A_2 and A_3, where A_3 is finite and A_1, A_2 are respectively $-\infty$ and $+\infty$.

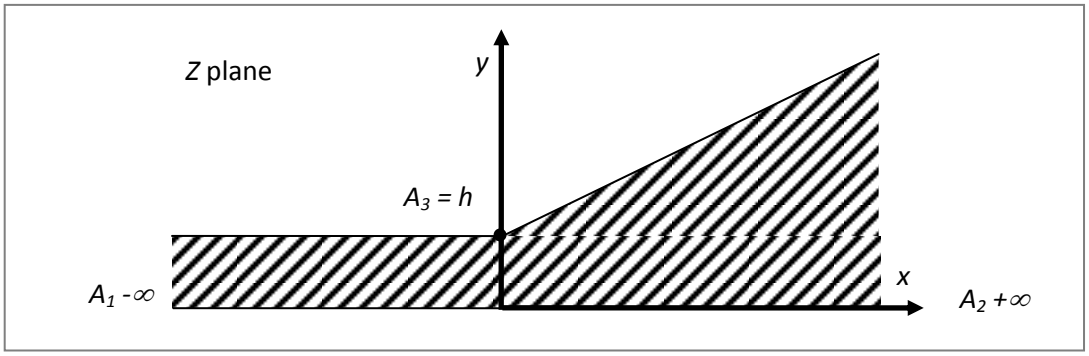

Figure A-1*: Shape in physical plane to be transformed by Schwarz-Christoffel transformation in a complex plane.*

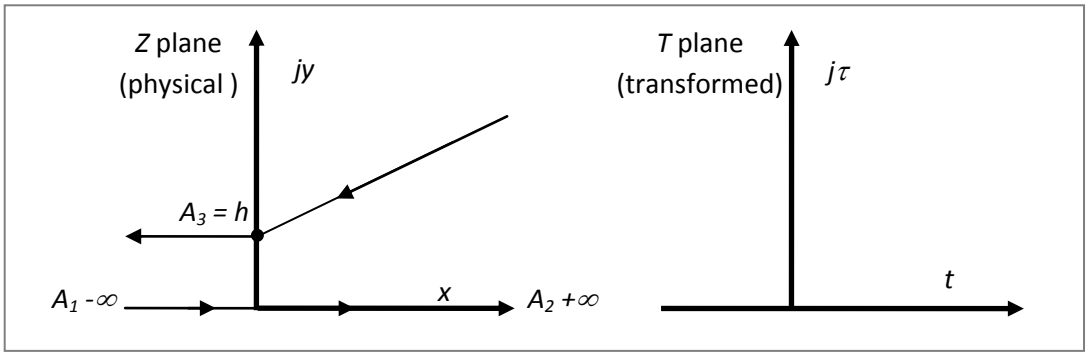

Figure A-2: *Representation of the physical plane* Z(x,jy) *and the transformed plane* T(t, jτ).

Applying the Schwarz-Christoffel transformation in equation (A-1) the physical plane *Z* is transformed in a complex plane *T(t,jτ)*:

$$Z(t) = C_1 \int_{t_0}^{t} (t-t_1)^{-\frac{\phi_1}{\pi}} (t-t_2)^{-\frac{\phi_2}{\pi}} \ldots dt + C_2 \qquad \text{(A-1)}$$

Where ϕ_i are the exterior angles defined rotating counter clockwise (CCW) along the polygon and the sum of which is equal to 2π. In this case the exterior angles of the three vertices of the triangle are defined as following:

- $A_1 = \pi$
- $A_3 = -\beta$ (it is negative because of the CCW constraint)
- $A_2 = 2\pi - (\pi - \beta) = \pi - \beta$ (because the sum of the three must be equal to 2π)

The destination of points A_1, A_2, and A_3 on the transformed plane *T* are t_1, t_2 and t_3 can be chosen arbitrarily, nevertheless choosing one of them at infinite, say $t_2=+\infty$, is a good choice as its effect will be absorbed in the constant C_1 of the transformation equation.

***Table A-1**: transformation correspondence between physical plane and transformed plane*

	Physical plane *Z*	Exterior angles	Transformed plane *T*
A_1	$-\infty$	π	$t_1 = 0$
A_2	jh	$\pi - \beta$	$t_2 = +\infty$
A_3	$+\infty$	$-\beta$	$t_1 = -1$

Introducing the data **Table** into Equation (A-1) therefore:

$$Z(t) = C_1 \int_{t_0}^{t} (t - t_1)^{\frac{\beta}{\pi}} t^{-1} dt + C_2 \qquad (A\text{-}2)$$

As can be defined $\beta = \alpha\pi$

$$Z(t) = C_1 \int_{t_0}^{t} (t - t_1)^{\alpha} t^{-1} dt + C_2 \qquad (A\text{-}3)$$

That is the transformation that brings the points on *Z* to a complex plane *T*.

In order to calculate the two constant C_2, eq. (A-3) is calculated in point A_3.

$$jh = C_1 \int_{t3}^{t3} (t - t_1)^{\alpha} t^{-1} dt + C_2 \qquad (A\text{-}4)$$

That results in:

$$C_2 = jh \qquad (A\text{-}5)$$

And therefore

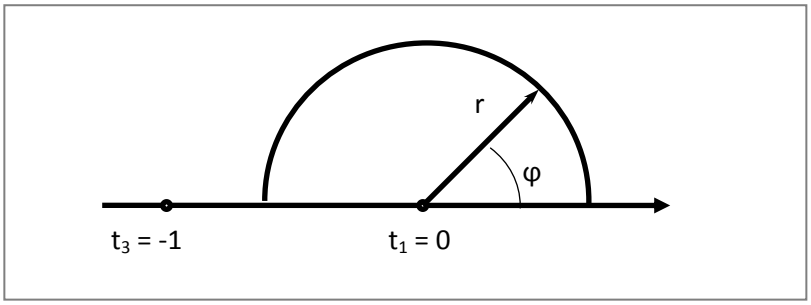

Figure A-3: *Graphic representation of the calculation of the constant C_1. When $r \to 0$ is when the point t_1 is reached.*

$$Z(t) = C_1 \int_{-1}^{t} (t - t_1)^{\alpha} t^{-1} dt + jh \qquad \textit{(A-6)}$$

The constant C1 can be calculated by pointing in t_1=0 and evaluating the increment of the integral of eq.(A-4) around that point infinitesimally.

When t = t_1-r the integral is:

$$Z(t_1 - r) = C_1 \int_{-1}^{t_1 - r} (t - t_1)^{\alpha} t^{-1} dt + jh \qquad \textit{(A-7)}$$

And when t = t_1+r the integral is:

$$Z(t_1 + r) = C_1 \int_{-1}^{t_1 + r} (t - t_1)^{\alpha} t^{-1} dt + jh \qquad \textit{(A-8)}$$

As *r* is infinitesimal, $(t+1)^{\alpha}$ has the same value in eq.(A-7) and in eq.(A-8) has the same value. It is possible, hence, to write:

$$Z(t_1 + r) - Z(t_1 - r) = C_1 \int_{-r}^{+r} (t - t_1)^{\alpha} t^{-1} dt + jh \qquad \textit{(A-9)}$$

As $(t+1)^{\alpha} \cong 1$ because $-r < t < +r$ is infinitesimal:

$$Z(t_1 + r) - Z(t_1 - r) = C_1 \int_{-r}^{+r} \frac{dt}{t} + jh \qquad \textit{(A-10)}$$

If $t = re^{j\varphi}$ and $dt = rje^{j\varphi} d\varphi$ then for $t = -r \;\; \varphi = \pi$ and for $t = +r \;\; \varphi = 0$. Therefore eq.(A-10) can be solved as:

$$\int_{-r}^{+r} \frac{dt}{t} = \int_{\pi}^{0} \frac{rje^{j\varphi}}{re^{j\varphi}} d\varphi = -j\pi \qquad \textit{(A-11)}$$

Hence:

$$Z(t_1 + r) - Z(t_1 - r) = -j\pi C_1 + jh \qquad \textit{(A-12)}$$

With $r \to 0$ C_1 results to be:

$$C_1 = \frac{h}{\pi} \qquad \textit{(A-13)}$$

Therefore eq.(A−3) can be written as:

$$Z(t) = \frac{h}{\pi}\int_{t_0}^{t}(t-t_1)^{\alpha}t^{-1}dt + jh \qquad \textit{(A-14)}$$

The transformation from $T \to W$ plane is $t = e^w$, $dt = e^w dw$ and transforms a positive semi-plane to a band between two infinite parallel lines, as showed in Figure A−4. When $t = -1$ results in $= j\pi$; $t = 0$ results in $w = -\infty$ and $t = +\infty$ results in $w = +\infty$.

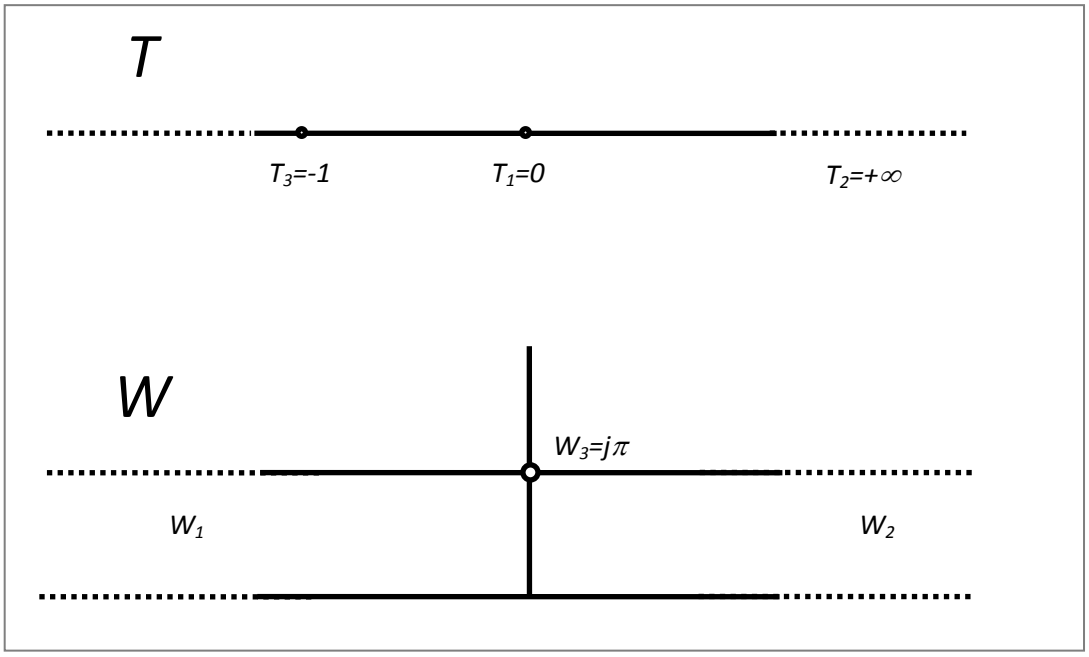

***Figure A-4**: Representation of the T plane transformed in the W plane.*

Eq.A−14 is hence written as:

$$Z(w) = \frac{h}{\pi}\int_{j\pi}^{w}(e^w+1)^{\alpha}e^{-w}e^w dw + jh \qquad \textit{(A-151)}$$

Therefore:

$$Z(w) = \frac{h}{\pi}\int_{j\pi}^{w}(e^w+1)^{\alpha}dw + jh \qquad \textit{(A-16)}$$

Eq.A−16 can be used to solve analytically electrowetting problem for the specific shape presented at the beginning.

Annex II

B1 Step-by-step modeling of electrowetting devices

B1.1 Initialization

In this Annex is described the step-by-step process for a complete multiphysic simulation setup, involving electronic circuits (CIR), electrostatics (ES) and computed fluid dynamics (CFD). When Comsol is started, the interactive wizard starts automatically. The navigation between screens is done by the right arrow, Figure B-1.

Firstly user selects the simulation type; as symmetries are used for geometry design, and simulation time optimization, 2D axisymmetric simulation has been chosen (Figure B-1a). Following, the physics selection window appears: multiple physics are chosen by multiple selections, Figure B-1b.

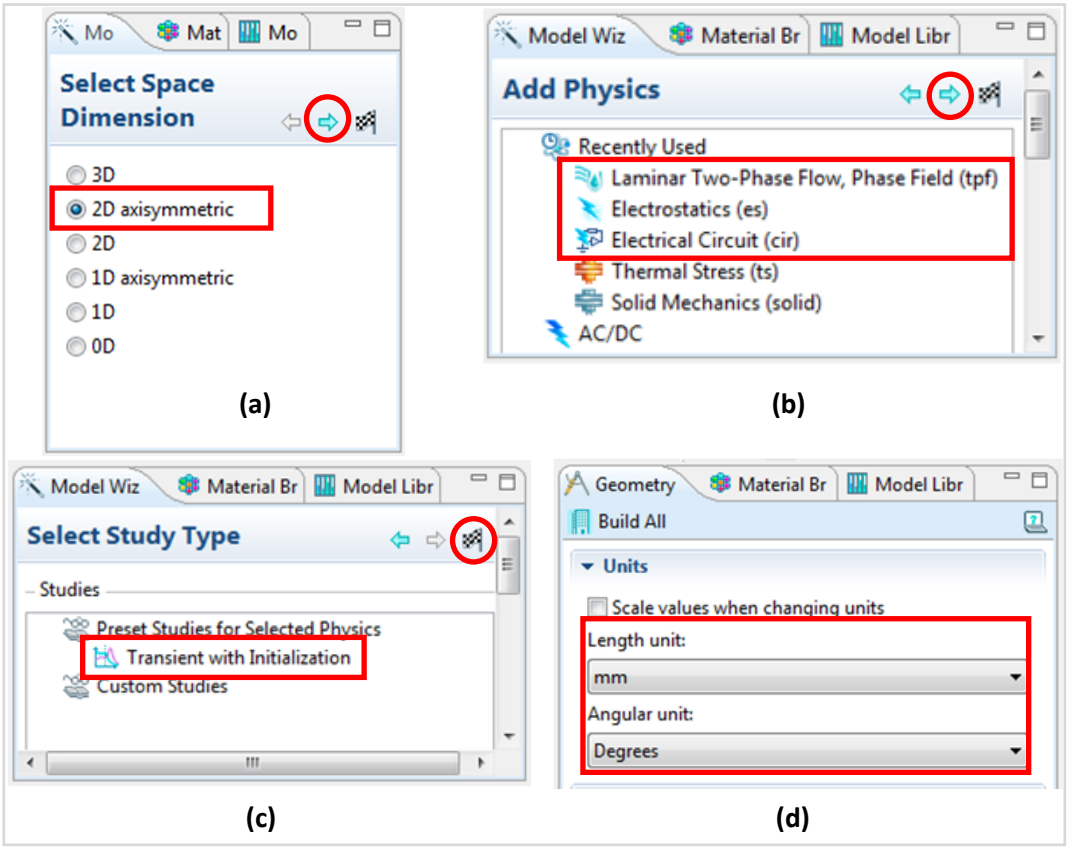

Figure B-1: *Step by step simulation model definition. A) Definition of the space in which simulation is run; b) selection of the physics involved in simulation; c) study selection of the simulation and finally d) definition of the units for the geometry design.*

For electrowetting, the physics involved are *"Laminar Two Phase Flow"* (TPF)*, "Electrical circuits"* (CIR) and "*Electrostatics"* (ES).

The simulation to be performed is a time-dependent simulation as the focus is the transient dynamics; therefore transient with phase initialization simulation type is chosen (Figure B-1c). The simulation start up finalizes when the chess flag is clicked. Prior the geometry and boundary conditions definition the length unit must be specified; mostly, electrowetting geometries are in the millimeters range, therefore the unit length is chosen accordingly.

Before designing the geometry, it is good practice to define, if needed, custom variables and functions. For electrowetting devices these variables and functions are mainly described in Table 2-1 and Table 2-2.

This procedure can be done by following the instructions below:

- In the ***Model Builder*** menu, right click on ***Global Definitions*** and select ***Parameters***; enter the following settings from Table 2-1.
- In the ***Model Builder*** menu, expand the ***Model 1*** menu and right click on ***Definitions***. Select ***Variables*** and enter the functions specified in Table 2-2.

Geometry definition

Model geometries can be designed using built-in Comsol CAD or they can be imported from external CAD program by clicking on "Geometry" in the simulation tree.

Once the geometry to be simulated is fully designed or imported, materials are assigned to the correspondent domain and boundary conditions are specified.

Figure B-2 shows the axisymmetric representation of a droplet of approximately 5μl (~1mm radius) sitting on a slightly hydrophobic surface and surrounded by air. The geometry is obtained by right clicking ***Geometry*** in the ***Model Builder*** and using the tools available for geometry design; in order to import an existing geometry ***Import*** from the drop down menu must be selected.

The dielectric layer is not designed as the mesh of the geometry would not converge due to the size of the layer (~1μm).

Instead, the thin dielectric layer is defined as a boundary condition in the ES module.

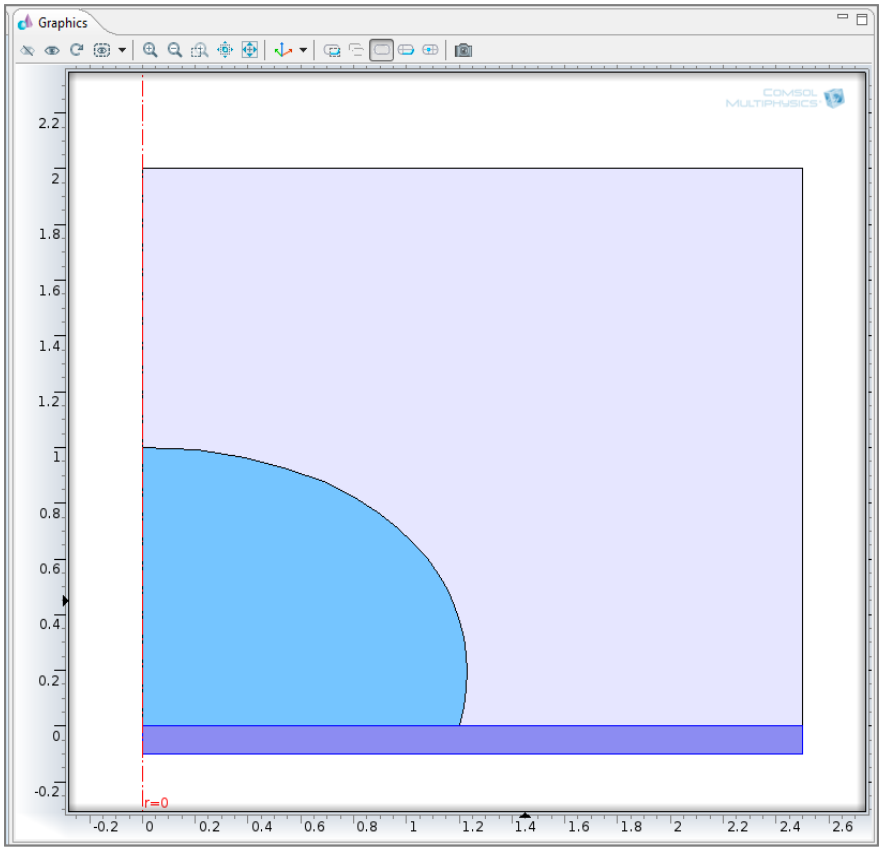

Figure B-2: *Electrowetting on dielectric droplet based simulation geometry.*

Table 2-2 shows the full implementation of the Maxwell Stress Tensor calculation. The coupling between ES and CFD is done by tracking the fluid-fluid interface and recalculating the relative permittivity according fluid movement.

This strategy implemented by taking advantage of the level set method magnitude *tpf.VfX*, which represents the volume of fluid fraction of the phase *X*. In this way the material physical properties related to a domain follow the movement of the fluid interface even though the geometry designed does not change move.

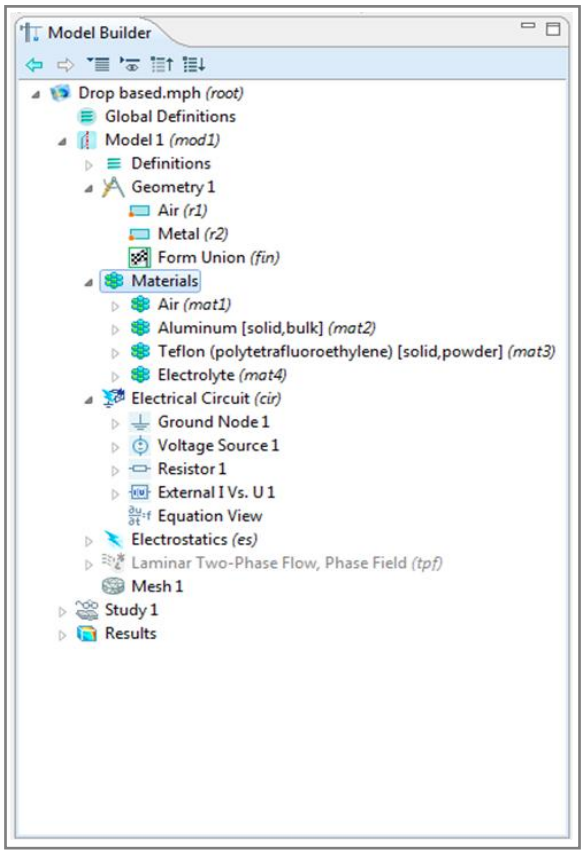

Figure B-3: *Material properties definition menu.*

Material properties are assigned by clicking on the ***Materials*** menu, Figure B-3, and adding a new material or picking one from the material library and then modifying physical parameters with the ones specified in ***Parameters*** definition. To each material, a domain must be associated. Boundary conditions are applied to each module separately.

B1.2. Boundary conditions setup for droplet-based electrowetting simulation

Boundary conditions for CIR module

CIR module defines the power supply circuit. In the most generic case, power supply provides voltage and there are no specific requirements. In the case taken into account, as example, the voltage supply has a current compliance of 20mA.

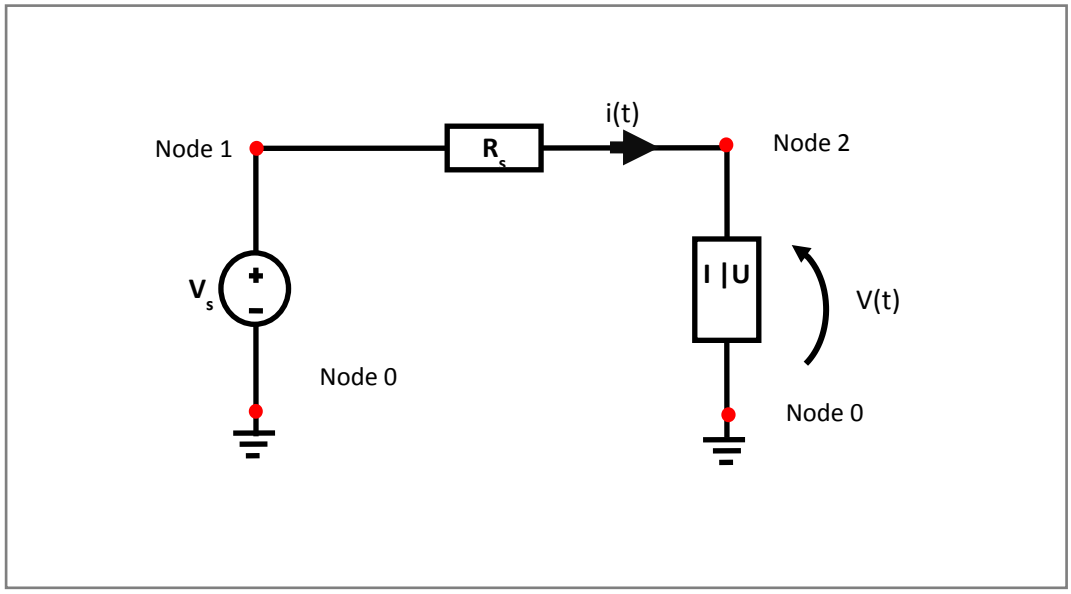

Figure B-4: *a) CIR module: a PSpice netlist can be directly imported, nevertheless a circuit definition can be done by using the components shown and interfacing them to ES module using External IvsU, UvsI and I-terminal. B) Schematic of the generator circuit interfaced to the electrowetting on dielectric device. The interface to the simulated geometry is done by a I|U component that applies to ES module terminal the voltage and current computed by the CIR module.*

Circuits defined as PSPICE net list can be easily imported by right-clicking on ***Electrical Circuit (CIR***), on the other hand, it is possible to define circuits from the same menu by adding components and specifying nodes and values.

The circuit to be described is shown in Figure B-4, where the voltage *V(t)* at terminals depends on the voltage generator with values comprised between 50V and 70V; the current *i(t)* is limited by the resistance of the generator R_g to a typical value 20 to 100mA.

The boundary conditions applied to voltage generator, resistor and external load (I|U) are shown in Figure B-5a, Figure B-5b and Figure B-5c respectively. The voltage generator boundary conditions are shown in Figure B-5a.

The device parameters are set to: DC voltage and 70V; the voltage generator is placed between nodes 1 and 0. Resistor boundary conditions are shown in Figure B-5b; the resistance value is set to 3.5kΩ, in order to limit current to 20mA; the resistor is placed between node 1 and 2.

Finally, Figure B-5c shows the boundary conditions for the external load (I|U). The component is placed between nodes 2 and 0; electric potential is set to "terminal voltage", nevertheless this option only appears after *Terminal* component is added in ES module.

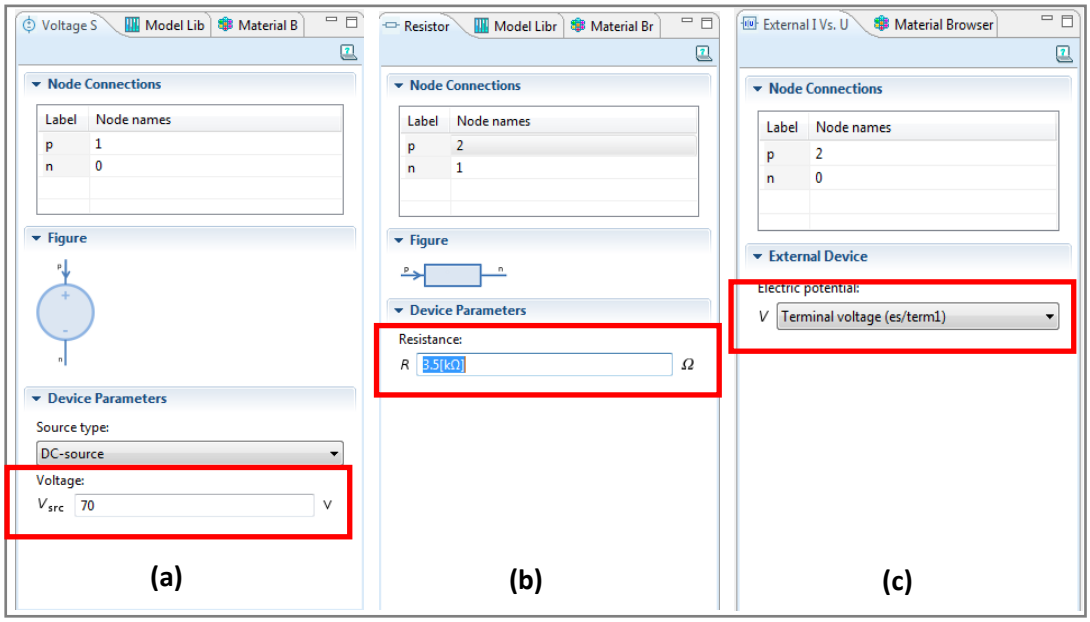

Figure B-5: *Boundary conditions for a) the voltage generator, b) the resistor and c) the external IvsU component. In particular external IvsU component feature "Terminal voltage" will appear when in ES module will be added the Terminal component.*

Boundary conditions for electrostatic (ES) module

ES boundary conditions are set by right-clicking on the ***Electrostatic (ES)*** menu in the model tree. In this menu, domain and line boundary conditions can be specified, as shown in Figure B-6.

The electrostatic boundary conditions specified are set over lines. Ground, terminal and low permittivity gap conditions are applied to the model geometry as shown in Figure B-7, Figure B-8 and Figure B-9.

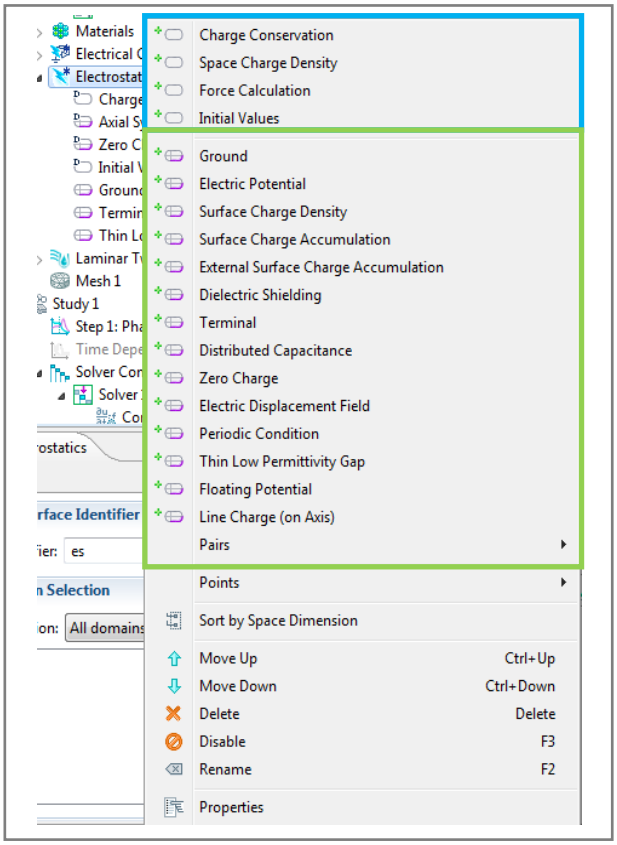

Figure B-6: *Electrostatic boundary conditions. The features highlighted in blue apply boundary conditions to domains while the features highlighted in green apply boundary conditions to lines and contours.*

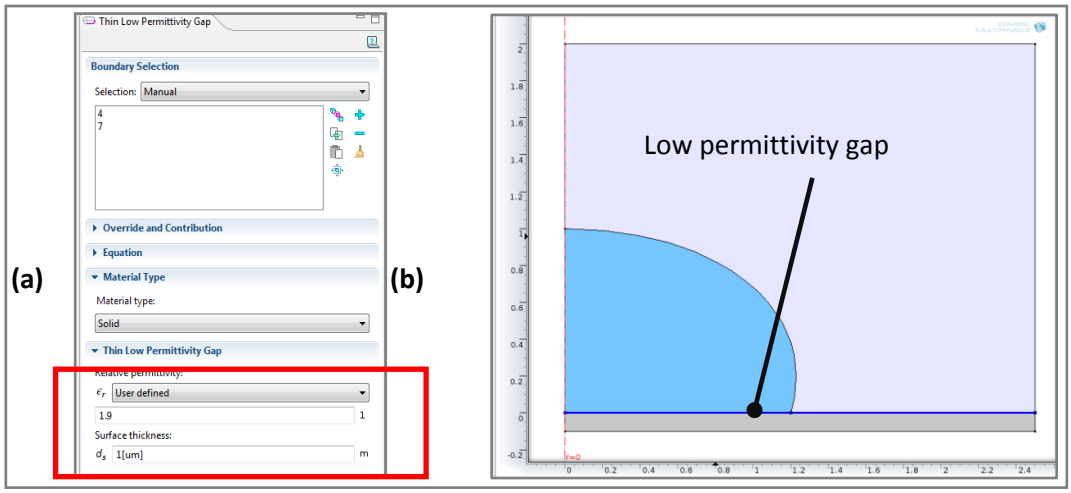

Figure B-7: *Low permittivity gap boundary condition defined on the surface of the hydrophobic layer. The hydrophobic layer has been defined as 1µm thick and showing a relative permittivity constant of 1.9 (Teflon).*

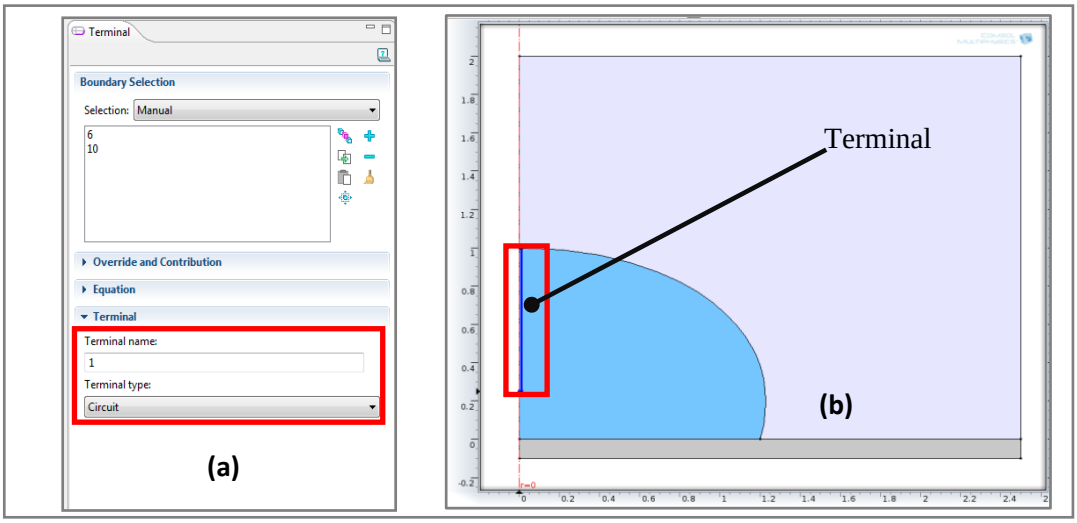

Figure B-8: *ES electrostatic module boundary conditions definition: a) thin low permittivity gap (dielectric layer) definition; b) Terminal definition on node 1 and c) ground definition.*

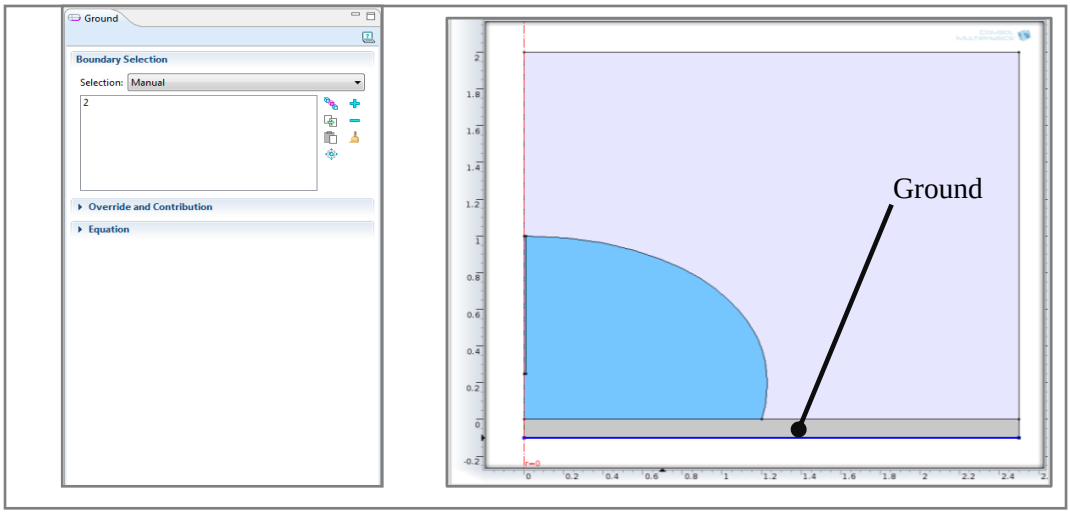

Figure B-9: *Ground is designed to be the bottom of the electrode. A)By default, it is node 0. b) shows the boundary line chosen as Ground*

The low permittivity gap is specified by manually entering thickness and relative permittivity of the Teflon layer. The boundary is chosen as the line between the bottom electrode and the electrolyte/air.

The terminal is linked to the electrical circuit by specifying the terminal type (circuit) and selecting the lines that form the needle contour. In the same way it is chosen the ground, the area beneath the electrolyte and the air, as shown in Figure B-9.

Boundary conditions for the laminar two-phase flow (TPF) module

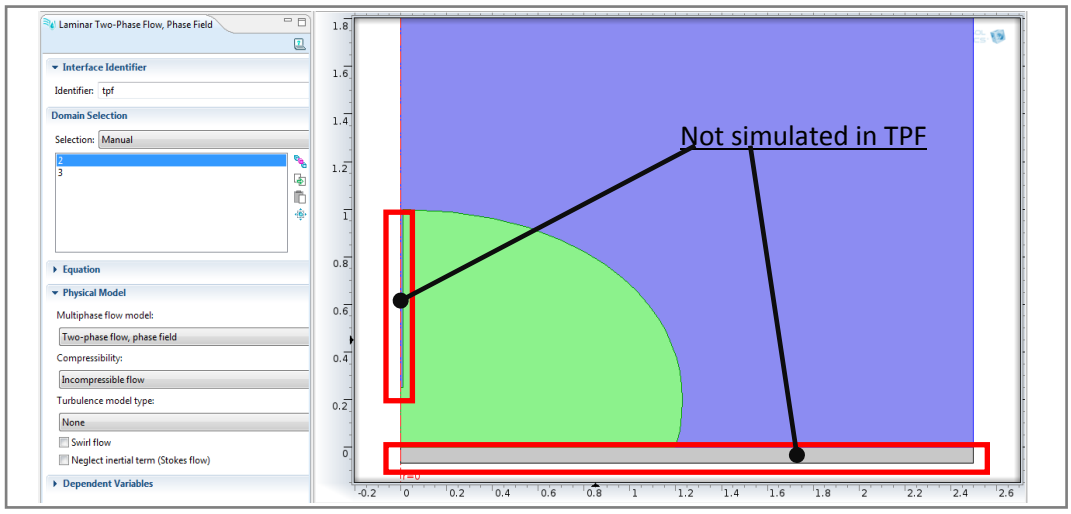

Figure B-10 *Settings of the Laminar Two-Phase Flow: metal domains are excluded from the simulation.*

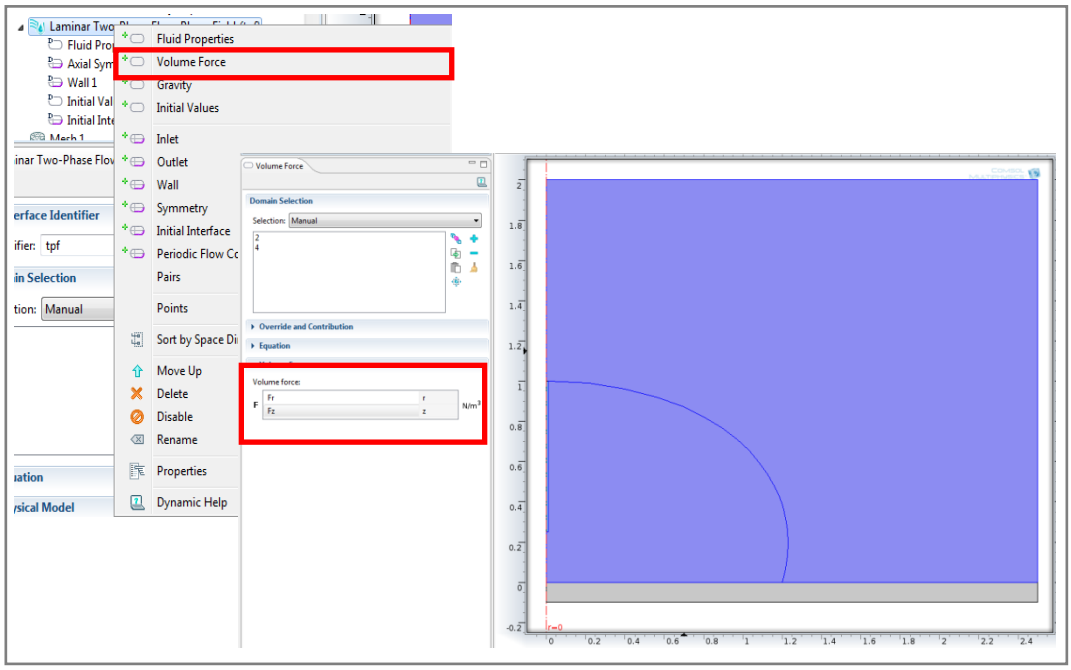

Figure B-11: *Volume Force boundary condition definition by applying Maxwell stress tensor calculated by ES module to the Laminar Two -Phase flow*

The laminar two-phase flow module only takes into account liquid domains, which means that the geometry areas occupied by metal have to be unselected from TPF simulation. This operation is done by clicking on ***Laminar Two-Phase Flow (tpf)*** menu and unselecting the needle and bottom electrode domains as shown in Figure B-10

By right clicking on the ***Laminar Two-Phase Flow (tpf)*** menu, volume force boundary condition can be set over the liquid and air domains, by entering *Fr* and *Fz* values in *Volume force* menu shown in Figure B-11. In order to allow the system to converge, it is mandatory to define a Zero Pressure Point. This operation is shown in Figure B-12 and usually it is chosen a corner that can never be reached by the liquid movement.

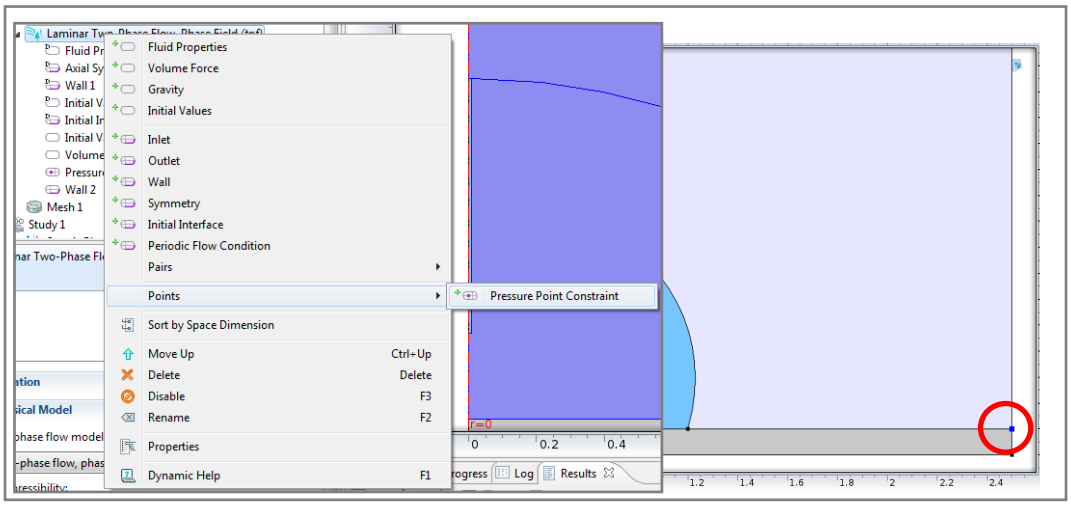

Figure B-12: *Zero pressure point boundary condition. In detail is shown the point, far from the drop domain, where pressure is set to "0".*

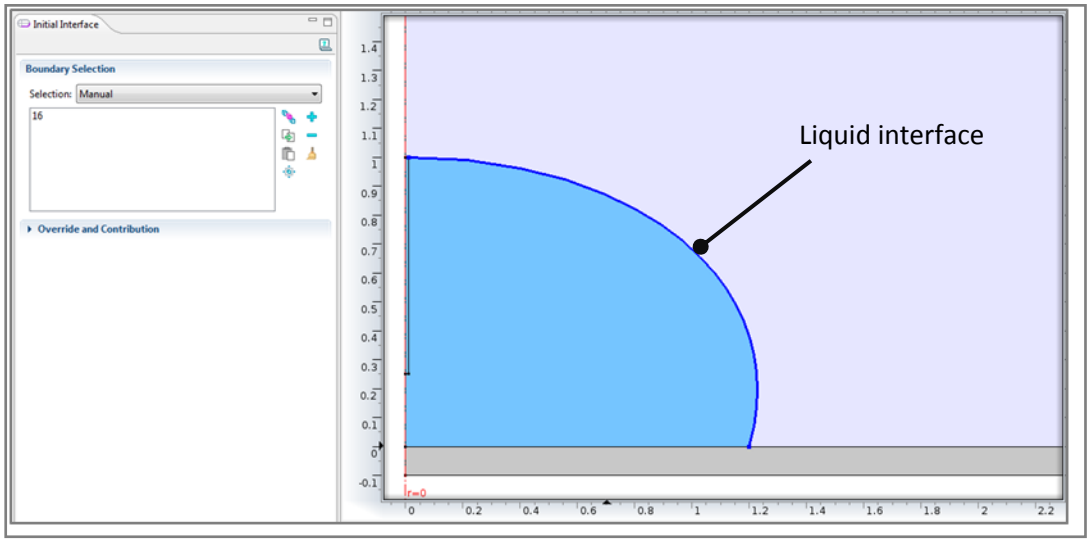

Figure B-13: *Initial fluid interface boundary selection. The interface between the liquid drop and the surrounding air must be selected.*

Following, *phase 1* and *phase 2* must be identified. This operation is done by selecting *Initial values* in the domain properties definition. Figure B-15 shows the full work flow: first enter as fluid 1 the droplet domain, Figure B-15a; add another "*Initial values*" at the

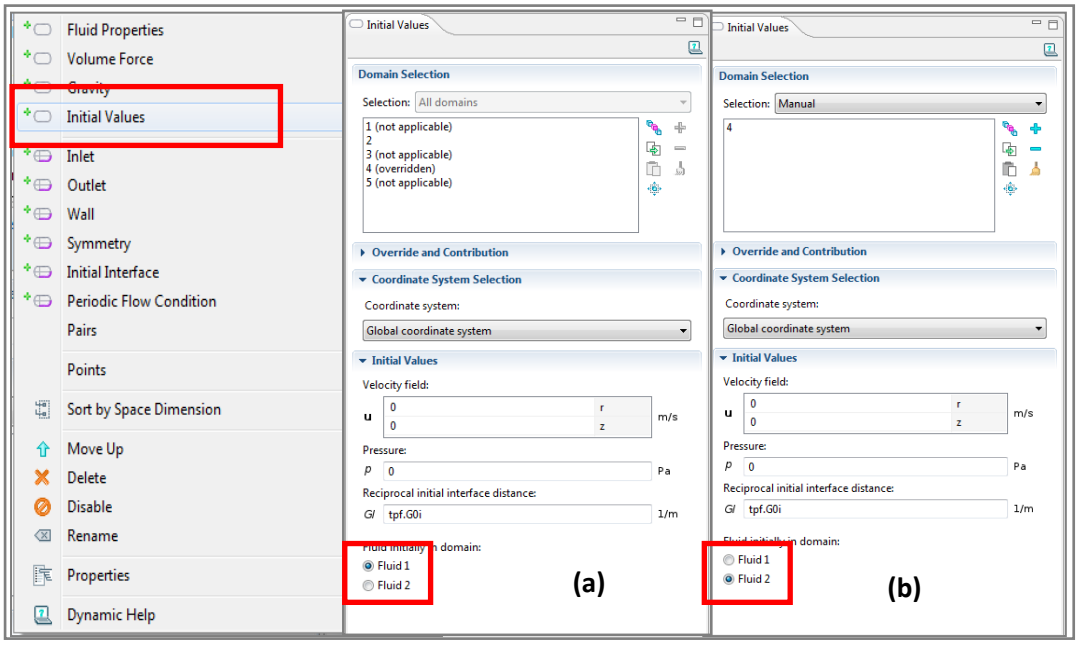

Figure B-15: *Fluid initial conditions a) drop domain set as "fluid 1" and b) air domain is set to "fluid 2".*

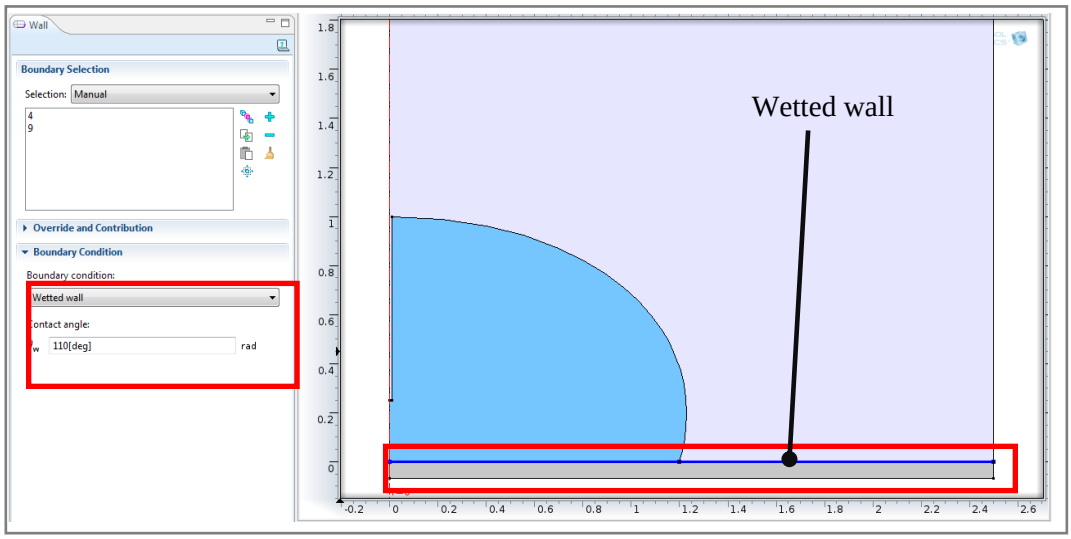

FigureB-14: *Wetted wall boundary definition. The surface where the droplet sits shows an initial contact angle of 110°. The boundary condition is defined by entering the contact angle value in radians or specifying the dimension is degrees.*

model tree and select air as fluid 2, Figure B-15b. Following, the interface between liquid droplet and air must be defined. Figure B-13 shows how to apply this boundary condition to the model geometry.

Finally, the wall constraint is defined by clicking on "*Wall";* if "Wetted wall" boundary condition is selected, then a specific contact angle (or a function of it) can be specified. In this case, the angle specified is 110° as reported in FigureB-14.

B1.3 Study definition

In order to perform correctly a multiphysic simulation, a study must be prepared. The study to perform a correct *CIR-ES-TPF* simulation must have at least 2 steps: *Phase initialization* and *time dependent* step.

In ***Phase Initialization*** step is needed to set the initial conditions for the TPF module. In Figure B-16a it is shown how to set the ***Phase initialization*** step: *CIR* and *ES* physics must be not selected while in ***Dependent values*** menu *Initial expression* and ***Zero solution*** must be selected. The ***Time dependent*** step, just below, must be set as in Figure B-16b: all physics are selected; the ***Dependent values*** are set to ***Study1***, ***Phase initialization*** and ***Automatic***. The time range specified in this case is 1ms with 1000 steps.

In order to start the simulation, ***Study1*** *must be selected, therefore in the upper menu will appear the symbol* ***"="*** *as shown in* Figure B-17.

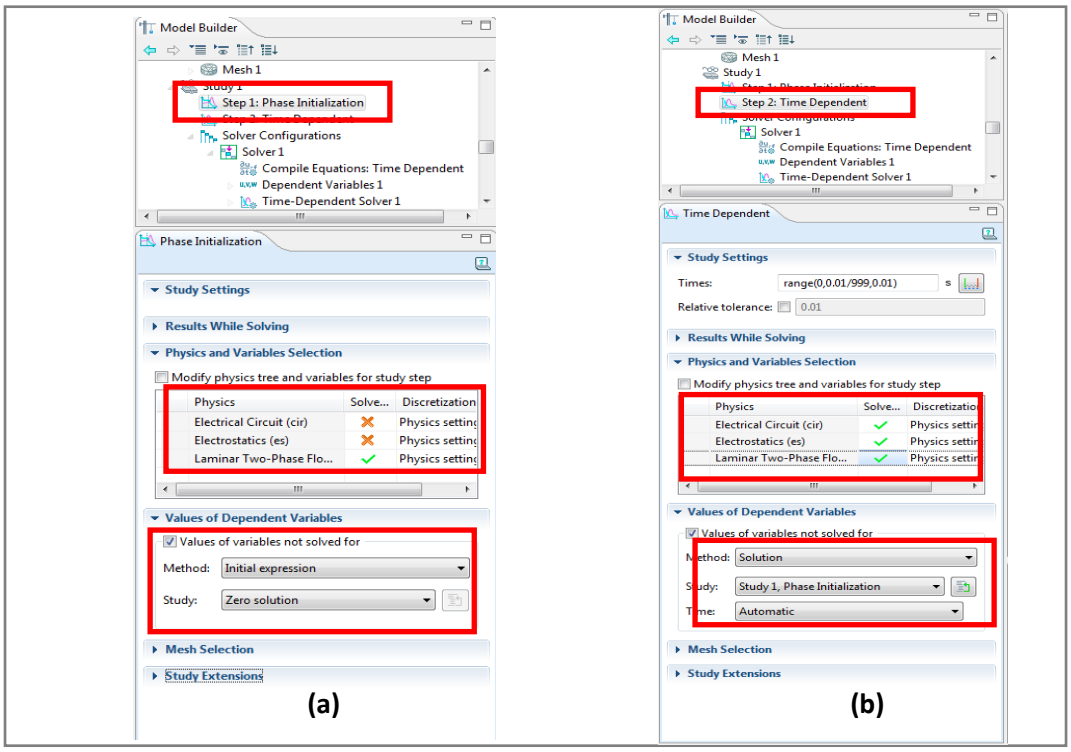

Figure B-16: *Study definition. A) Step 1: phase initialization only takes into account the laminar two-phase flow module. The dependent variables must be set to "initial expression" and "zero solution". B) In Step 2, a full CIR-ES-TPF simulation is performed, starting from the solution of study 1 and over a time range comprised between 0 and 0.001s with 1000time steps.*

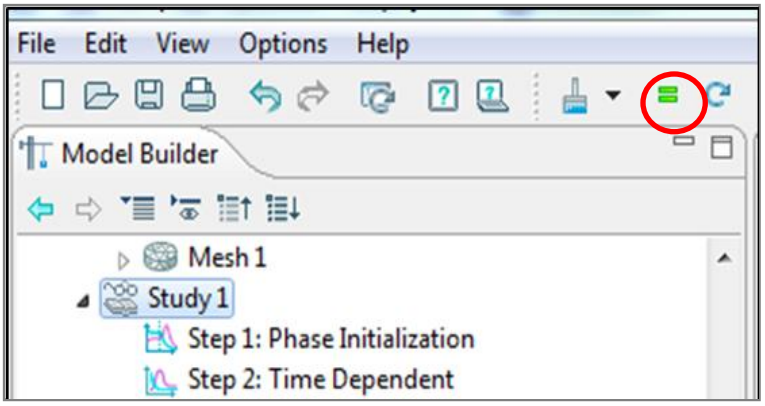

Figure B-17: *In order to start the simulation, Study1 must be selected and "=" must be clicked.*

List of publications

[1] V., Di Virgilio; L., Castañer, “Comparison of static contact angle change and relaxation in EWOD devices”, *Spanish Conference on Electron Devices*, 2009.

[2] V., Mokkapati; V., Di Virgilio; C., Shen; J., Mollinger; J., Bastemeijer; A., Bossche, “Nanochannels fabrication, filling and DNA manipulation”, *ASME First Global Congress on Nano Engineering for Medicine and Biology,* p.135-138, 2010.

[3] V., Di Virgilio; A., Coll; S., Bermejo; L., Castañer, “Dynamic simulation of particle self-assembly applied to microarray technology”, *Comsol Conference*, Paris 2010.

[4] A., Coll; V., Di Virgilio; S., Bermejo; L., Castañer, “Simulation of photonic crystals particle filling by electrospray ”, *Comsol Conference*, Paris 2010.

[5] L., Castañer; V., Di Virgilio; S., Bermejo; "Charge-coupled transient model for electrowetting”, *Langmuir,* 26(20), p.16178-85, Oct 19 2010.

[6] V., Di Virgilio; S., Bermejo; L., Castañer, "wettability increase by "corona" ionization”, *Langmuir*, 27(15), p.9614-2, Aug 2 2011.

[7] V., Di Virgilio; A., Coll; S., Bermejo; L., Castañer, “Modeling and simulation of a cost-effective microfluidic circuit for particles’ manipulation”, *Spanish Conference on Electron Devices*, 2011.

[8] V., Mokkapati; V., Di Virgilio; C., Shen; J., Mollinger; J., Bastemeijer; A., Bossche, “DNA tracking within a nanochannel: device fabrication and experiments”, *Lab on a Chip,* 11 (16), 2711-2719, 2011.

Bibliography

[1] G. Lippmann, "Relations entre les phénomènes électriques et capillaires," *Annales de Chimie et de Physique,* 1875.

[2] G. Beni and S. Hackwood, "Electrowetting displays," *Bulletin of the American Physical Society Vol.26, N.3,* pp. 445 -446, 1981.

[3] B. Berge, "Electrocapillarité et mouillage de films isolants par l'eauI," *Comptes Rendues de l'Academie des Sciences Paris, t. 317, Série II,* p. 157, 1993.

[4] F. a. B. J.-C. Mugele, "Electrowetting: from basics to applications," *J. Phis. Condens. Matter 17, 705 ,* 2005.

[5] P. G. deGennes, "Wetting: statics and dynamics," *Rev. Mod. Phys. 57 ,* p. 827, 1985.

[6] H. a. P. M. Verheijen, " Reversible electrowetting and trapping of charge: model and experiments," *Langmuir, 15,* p. 6616, 1999.

[7] B. Janocha, H. Bauser, C. Oehr and H. a. G. W. Brunner, "Competitive Electrowetting of Polymer Surfaces by Water and Decane," *Langmuir,* vol. 16, no. 7, p. 3349–3354, 2000.

[8] M. Vallet and M. a. B. B. Vallade, "Limiting phenomena for the spreading of water on polymer," *The European Physical Journal B,* vol. 11, pp. 583-591, 1999.

[9] V. Di Virgilio and S. C. L. Bermejo, "Wettability increase by "Corona" ionization," *Langmuir,* vol. 27, pp. 9614-9620, 2011.

[10] S. R. a. R. J. Quinn A, "Contact angle saturation in electrowetting," *J.Phys Chem. B,* vol. 109, pp. 6268-6275, 2005.

[11] A. Quinn, R. Sedev and J. Ralston, "Influence of the electrical double layer in electrowetting," *J. Phys. Chem. B,* vol. 107, pp. 1163-1169, 2003.

[12] A. a. B. A. G. Papathanasiou, "Manifestation of the connection between dielectric breakdown strength and contact angle saturation in electrowetting," *Applied Physics Letters,* vol. 86, p. 164012, 2005.

[13] A. G. Papathanasiou and A. G. Papaioannou A. T. and Boudouvis, "Illuminating the connection between contact angle saturation and dielectric breakdown in electrowetting through leakage current measurements," *Journal of Applied Physics,* vol. 103, p. 034901, 2008.

[14] A. Drygiannakis and A. G. a. B. A. G. Papathanasiou, "On the connection between dielectric breakdown strength, trapping of charge and contact angle saturation in electrowetting," *Langmuir,* vol. 25, no. 1, 2009.

[15] T. B. Jones, "On the relationship of dielectrophoresis and electrowetting," *Langmuir ,* vol. 18, p. 4437, 2002.

[16] T. B. Jones, J. D. Fowler and Y. S. a. K. C. Chang, "Frequency-based relationship of electrowetting and dielectrophoretic liquid microactuation," *Langmuir ,* vol. 19, p. 7646, 2003.

[17] T. Jones and K. a. Y. D. Wang, " Frequency-dependent electromechanics of aqueous liquids: Electrowetting and dielectrophoresis.," *Langmuir ,* vol. 20 , p. 2813, 2004.

[18] H. H. Woodson and J. R. Melcher, Electromechanical dynamics, part I: Discrete systems., New York: Wiley, 1968.

[19] C. E. Rosenkilde, "A dielectric fluid drop in an electric field," *Proc.Royal Soc. (London),* vol. A312, pp. 473-494, 1969.

[20] R. Digilov, "Charge-induced modification of contact angle: the secondary electrocapillary effect.," *Langmuir,* vol. 16, pp. 6719-6723, 2000.

[21] K. Kang, "How electrostatic fields change contact angle in electrowetting," *Langmuir,* vol. 18, p. 10318, 2002 .

[22] B. a. P. J. Berge, "Variable focal lens controlled by an external voltage: an application of electrowetting," *Eur.Phys.J.,* vol. E3, no. 159, 2000.

[23] "www.varioptic.com," [Online].

[24] R. A. Hayes and B. J. Feenstra, "Video-speed electronic paper based on electrowetting," *Nature,* vol. 383, p. 425, 2003.

[25] "www.liquavista.com," [Online].

[26] J. Heikenfeld, K. Zhou, E. Kreit, B. Raj, S. Yang, B. Sun, A. Milarcik and L. a. S. R. Clapp, "Electrofluidic displays using Young-Laplace transposition if brilliant pigment," *Nature Photonics,* vol. 3, p. 292, 2009.

[27] "www.gammadynamics.net," [Online].

[28] "www.adt-gmbh.de," [Online].

[29] S. K. Cho and J. H. a. K. Moon, "Creating, transporting, cutting, and merging liquid droplets by electrowetting-based actuation for digital microfluidic circuits," *J. Microelectromech. Syst.,* vol. 12, no. 70, 2003.

[30] V. Srinivasan and V. K. a. F. R. B. Pamula, "An integrated digital microfluidic lab-on-a-chip," *Lab Chip,* vol. 4, no. 310, 2004.

[31] R. B. Fair, "Digital microfluidics: is a true lab-on-a-chip possible?," *Microfluid Nanofluid.,* vol. 3, no. 245, 2007.

[32] "http://www.liquid-logic.com/," [Online].

[33] "www.illumina.com," [Online].

[34] "http://www.mphasetech.com/," [Online].

[35] T. K. a. J. A. Taylor, "Reverse electrowetting as a new approach to high-power energy harvesting," *Nat Commun,* vol. 2, no. 448, 2011.

[36] N. S. a. P. J. Shenck, "Energy scavenging with shoe-mounted piezoelectrics," *IEEE Micro,* vol. 21 , pp. 30-42, 2001.

[37] "http://www.pavegen.com/," [Online].

[38] R. O'Donnell, " Energy harvesting from human and machine motion for wireless electronic devices.," *Proc. Ieee,* vol. 96, p. 1455–1456, 2008.

[39] A. Z. P. &. Z. C. Khaligh, "Kinetic energy harvesting using piezoelectric and electromagnetic technologies-state of the art," *Ieee Trans. Ind. Electron,* vol. 57, pp. 850-860, 2010.

[40] S. K. C. R. L. G. a. C.-J. “. K. Hyejin Moon, "Low voltage electrowetting-on-dielectric," *J. Appl. Phys.,* vol. 92, p. 4080, 2002.

[41] S. K. J. H. Manjeet Dhindsa, "Reliable and low-voltage electrowetting on thin parylene," *Thin solid films,* vol. 519, pp. 3346-3351, 2011.

[42] B. Cahill, A. Giannitsis, G. Gastrock and M. a. B. D. Min, "A Dynamic Electrowetting Simulation using the Level-Set Method," *Comsol Confenerces,* 2008.

[43] J. Dannenberg and J. a. L. E. Brinkert, "On The Modelling of Electrowetting in COMSOL MultiPhysics," *Comsol Conferences,* 2010.

[44] C. L. Yaws, Chemical Properties Handbook, New York: McGraw-Hill, 1999, pp. 897-

903.

[45] D. Fluoroproducts, Teflon properties handbook, Wilminghton: DuPont, 2010.

[46] W. Satoh and W. a. S. H. Loughran, "Microfluidic transport based on direct electrowetting," *J. Appl. Phys.,* vol. 96, pp. 835-841, 2004.

[47] F. Saeki, J. Baum, H. Moon, J.-Y. Yoon, C.-J. Kim and R. L. Garrell, "Electrowetting on Dielectrics (EWOD): Reducing Voltage Requirements for Microfluidics," *Polym. Mater. Sci. Eng.,* vol. 85, pp. 12-13, 2001.

[48] D. Arifin and L. a. F. J. Yeo, "Microfluidic Blood Plasma Separation Via Bulk Electrohydrodynamic Flows," *Biomicrofluidics,* vol. 1, p. 014103, 2007.

[49] V. Di Virgilio and L. Castañer, "Comparison of static contact angle change and relaxation in EWOD devices," *Proc. of 2009 Spanish Conference on electron devices,* pp. 46-49, 2009.

[50] D. M. R. L.Castañer, "Dielectric charge measurement in capacitive microelectromechanical systems," *Applied Physics Letters,* vol. 89, p. 103506, 2006.

[51] S. a. C. L. Senturia, "Speed-energy optimization of electrostatic actuators based on pull-in," *IEEE Jour. of Microelectromechanical systems (JMEMS),* vol. 8, no. 3, pp. 290-298, 1999.

[52] R. S. a. P. Laura, Conformal Mapping: methods and applications, Amsterdam: Elsevier, 1991.

[53] B. Chua, A. Wexler, N. Tien, D. Niemeier and B. Holmén, "Design, fabrication and testing of microfabricated corona ionize," *Journal of Microelectromechanical Systems,* vol. 17, pp. 115-123, 2008.

[54] J. Lowke, "Theory of electrical breakdown in air-the role of metastable oxygen molecules," *J.Phys. D. Journal of Applied Physics,* vol. 25, pp. 202-210, 1992.

[55] K. Feser and R. Hugues, "Measurement of Direct Voltage by Rod-Rod Gaps," *Electra,* vol. 117, pp. 23-24, 1988.

[56] F. Peek, Dielectric Phenomena in High Voltage Engineering, New York: McGraw-Hill, 1929.

[57] J. Oh and D. a. M. F. Legendre, "Shaken not stirred —On internal flow patterns in oscillating sessile drops," *EPL,* vol. 98, p. 34003., 2012.

[58] J. Oh and S. a. K. K. Ko, "Varifocal liquid lens based on microelectrofluidic technology," *Phys. Fluids,* vol. 22, p. 032002, 2010.

[59] K. S. a. K. K. Oh J.M., "Shape Oscillation of a drop in ac electrowetting," *Langmuir,* vol. 24, no. 15, pp. 8379-86, 2008.

[60] C. Eck, M. Fontelos, G. Grün and F. a. V. O. Klingbeil, "On a phase-field model for electrowetting," *Interfaces and free boundaries,* vol. 11, pp. 259-190, 2009.

[61] S. Walker and B. a. N. R. Shapiro, "Electrowetting with Contact Line Pinning: Computational Modeling and Comparisons with Experiments," *Physics of Fluids,* vol. 21, no. 10, pp. 102-103, 2009.

[62] S. Walker and A. a. N. R. Bonito, "Mixed Finite Element Method for Electrowetting On Dielectric (EWOD) with Contact Line Pinning," *Interfaces and Free Boundaries,* vol. 12, no. 1, pp. 85-109, 2010.

[63] P. W. P. C.-W.-B. C. S. Monnier, " Numerical modelling of electrowetting by a shape inverse approach," *SIAM J. Appl. Math. ,* vol. 69, no. 5, pp. 1477-1500, 2009.

[64] L. Castañer, V. Di Virgilio and S. Bermejo, "Charge-coupled transient model applied to electrowetting," *Langmuir,* vol. 26, pp. 16178-16185, 2010.

[65] T. D. Blake, A. Clarke and E. H. and Stattersfield, "An Investigation of Electrostatic Assist in Dynamic Wetting," *Langmuir,* vol. 16, no. 6, p. 2924–2927, 2000.

[66] M. Vallet and B. a. V. L. Berge, "Electrowetting of Water and Aqueous Solutions on Poly-ethylene-terephthalate Insulating Films," *Polymer,* vol. 37, no. 12, p. 2465–2470, 1996.

[67] T. D. a. H. J. M. Blake, " Kinetics of liquid/liquid displacement.," *Journal of Colloid Interface Science,* vol. 30, pp. 421-423, 1969.

[68] O. Voinov, "Hydrodynamics of wetting," *Fluid dynamics,* vol. 11, no. 5, pp. 714-721, 1976.

[69] M. Paneru, C. Priest and R. a. R. J. Sedev, "Static and Dynamic Electrowetting of an Ionic Liquid in a Solid/Liquid/Liquid System," *The Journal of the American Chemical Society,* vol. 132, p. 8301, 2010.

[70] P. Intra and N. Tippayawong, "Measurements of ion current from a corona-needle charger using a Faraday cup electrometer," *chiang Mai Journal of Science,* vol. 36, pp. 110-119, 2009.

[71] W. a. F. L. Welters, "Fast electrically switchable capillary effects," *Langmuir,* vol. 14, no. 7, pp. 1535-1538, 1998.

[72] S. Millefiorini, A. Tkaczyk, R. Sedev and J. a. R. J. Efthimiadis, "Electrowetting of ionic liquids," *J Am Chem Soc.,* vol. 128, no. 9, pp. 3098-101., 2006.

[73] M. Paneru, C. Priest and R. a. R. J. Sedev, "Electrowetting of Aqueous Solutions of Ionic Liquid in Solid-Liquid-Liquid Systems," *J. Phys. Chem. C,* vol. 114, p. 8383, 2012.

[74] J. Restolho and J. L. a. S. B. J. Mata, "Electrowetting of ionic liquids: contact angle saturation and irreversibility," *Phys. Chem. C ,* vol. 114, p. 9321, 2009.

[75] W. Wang, C. Li, B. Luo, X. Li, Y. Jiang, B. An and Y. Wang, "The effect of temperature and humidity on corona inception voltage gradient of UHV DC transmission line," in *International Conference on Condition Monitoring and Diagnosis*, Beijing, 2008.

[76] M. Meincken and T. A. a. M. P. E. Berhane, "Tracking the hydrophobicity recovery of PDMS compounds using the adhesive force by AFM force distance measurements.," *Polymer ,* vol. 46, pp. 203-208, 2005.

[77] V. M. Moreno, R. S. Gorur and Kroese, *A. IEEE Trans. Dielect.Elect. Insul.,* vol. 10, p. 80–95, 2003.

[78] V. Moreno and R. a. K. A. Gorur, "Impact of Corona on the long-term performances of non-ceramic insulators," *IEEE Transactions on Dielectrics and Electrical Insulation,* vol. 10, no. 1, pp. 80-95, 2003.

[79] G. Beni and M. Tenan, "Dynamics of electrowetting displays," *Journal of Applied Physics,* vol. 52, pp. 6011-6015, 1981.

[80] M. Pollack and A. a. F. R. Shenderov, " Electrowetting-based actuation of droplets for integrated microfluidics," *Lab on a Chip,* vol. 2, no. 96, 2002.

[81] F. Mugele and J. a. S. D. Baret, "Microfluidic mixing through electrowetting-induced droplet oscillations," *Appl. Phys. Lett ,* no. 88, p. 204106, 2006.

[82] C. Decamps and J. De Coninck, "Dynamics of Spontaneous Spreading under Electrowetting Conditions," *Langmuir,* vol. 16, no. 26, pp. 10150-10153, 2000.

[83] Dupont, "http://www2.dupont.com/Teflon_Industrial/en_US/assets/downloads/h44587.pdf," [Online].

[84] Microchem, "http://www.microchem.com/pdf/SU-

82000DataSheet2000_5thru2015Ver4.pdf," [Online].

[85] S. Chevaliot, J. Heikenfeld, L. Clapp and A. a. V. S. Milarcik, "Analysis of Nonaqueous Electrowetting Fluids for Displays," *IEEE Journal of Display Technolog,* vol. 7, no. 12, p. 649, 2011.

[86] E. Becker and W. a. K. T. Hiller, "Experimental and theoretical investigation of large droplets oscillations of liquid droplets," *Journal f Fluid Mechanics,* vol. 231, pp. 189-210, 1991.

[87] S. D. Pawar, P. Murugavel and D. M. Lal, "Effect of relative humidity and sea level pressure on electrical conductivity of air over Indian Ocean," *Journal of Geophysical Research,* vol. 114, 2009.

[88] H. Ren, R. Fair and M. a. S. E. Pollack, "Dynamics of electro-wetting droplet transport," *Sensors and actuators B: chemical,* vol. 87, no. 1, pp. 201-206, 2002.

[89] Y. B. S. K. Z. a. J. H. Lao, "Ultra-high transmission electrowetting displays enabled by integrated reflectors," *Journal of Display Technology,* vol. 4, pp. 120-122, 2008.

[90] R. F. Probstein, Physicochemical Hydrodynamics, 2nd ed., Hoboken, New Jersey: Wiley, 2003.

[91] K. Kang and I. a. L. C. Kang, "Electrostatic contribution to line tension in a wedge-shaped contact region," *Langmuir,* vol. 19, no. 22, pp. 9334-9342, 2003.

[92] J. M. Oh, S. H. Ko and K. H. Kang, "Analysis of electrowetting-driven spreading of a drop in air," *Phys. Fluids,* vol. 22, p. 032002, 2010.

[93] D. Aronov and M. a. R. G. Molotskii, "Charge-Induced Wettability Modification," *Appl. Phys. Letts,* vol. 90, p. 104104, 2007.

[94] "www.keithley.com/products/DCAC/currentsource," Keithley. [Online].

[95] M. Ghovanloo and K. Najafi, "A compact large voltage compliancehigh output impedance programmable current source for biomedical implantable microstimulators," *IEEE Trans. on Biomed. Eng,* vol. 52, pp. 97-105, 2005.

[96] R. Nadal-Guardia, A. Dehé, R. Aigner and L. Castaner, "Current drive methods to extend the range of travel of electrostatic microactuators beyond the voltage pull-in point," *Microelectromechanical Systems, Journal,* vol. 11, no. 3, pp. 255-263, 2002.

[97] L. Castañer and S. Senturia, "Speed-energy optimization of electrostatic actuators based on pull-in," *Microelectromechanical Systems,* vol. 8, no. 3, pp. 290-298, 1999.